ABSTRACT

HAN, KOOHEE. Field-Driven Reconfigurable Assemblies and Self-Propelling Microbots Engineered from Anisotropic Particles (Under the direction of Dr. Orlin D. Velev).

Colloidal systems of anisotropic particles in external fields represent a rapidly emerging area in soft matter, evoking intense interest due to their unusual interactions, dynamics, and structure formation abilities. From an engineering perspective, a variety of field-driven dynamic responses can be encoded in the design of anisotropic particles, thereby forming the basis of developing structures with on-demand functionality. Early examples of such structures have shown promise for making of materials with simple responses, such as one-dimensional contraction and translational motion in a single direction. However, encoding more sophisticated functionalities into colloidal structures has been challenging.

This dissertation presents engineering strategies to formulate a new class of dynamic structures capable of precise microscale operations. Our approaches are based on using anisotropic colloidal particles with tailored form factors and surface polarizabilities. To gain fundamental insights into their complex field-driven dynamic behaviors, we focus on particle-particle and particle-medium interactions at the microscale level. Building upon the identified fundamental breakthroughs, we develop concepts for miniaturized machines that could potentially address critical challenges in science and medicine.

First, we introduce self-reconfiguring microbots made by magnetic assembly and actuation of one-side cobalt coated patchy microcubes. Assemblies of the patchy microcubes can store energy through magnetic polarization of the cobalt patches and release it by microscale reconfiguration. These reconfiguration patterns are determined by the sequence of the cube orientations within the assemblies. We demonstrate microbot prototypes that can be used to capture and transport a target yeast cell by combining a uniform magnetic field for controlled

folding actuation with a gradient field for spatial maneuvering.

We extend the use of the sequence-encoded reconfiguration function of the multi-cube assemblies to make self-propelling microswimmers. Single-hinged “microscallop” assemblies can be directionally motile when suspended in non-Newtonian fluids and actuated by cyclic time-asymmetric magnetic fields. The field-controlled time-asymmetric flapping strokes of the microscallops create a local viscosity gradient and generate propulsive thrust. We demonstrate that the viscophoretic swimming motility of microscallop assemblies depends not only on the type of time-asymmetric flapping strokes, but also on their geometric length and sequence.

Lastly, we present another class of motile externally powered microdevices that controllably spin about their central axis in AC electric fields. The rational design of these “microspinners” enables the conversion of electrical energy into active rotation. Multiple electrokinetic mechanisms operating at different frequency ranges can be programmed via the anisotropy of the particle shape and polarizabilities. We demonstrate that the microspinners can switch their direction of rotation on-demand by changing the frequency of the electric fields.

The principles and engineering strategies identified in this dissertation could be extended to design dynamic structures with more elaborate functions and higher degree of controllability by using more complex particle shapes, compositions, and field parameters. We believe the scientific principles for making such advanced dynamic structures could be used to address a broad range of applications, from microbotics and micromanipulation, to smart functional materials.

Field-Driven Reconfigurable Assemblies and Self-Propelling Microbots Engineered from Anisotropic Particles

by
Koohee Han

A dissertation submitted to the Graduate Faculty of
North Carolina State University
in partial fulfillment of the
requirements for the degree of
Doctor of Philosophy

Chemical Engineering

Raleigh, North Carolina

2018

APPROVED BY:

_____	_____
Dr. Orlin D. Velev Committee Chair	Dr. Carol K. Hall
_____	_____
Dr. Jan Genzer	Dr. Michael D. Dickey

DEDICATION

This dissertation is dedicated to my family for all their support and love.

BIOGRAPHY

Koohee Han was born in Seoul, South Korea to Sang Hyuk Han and Eunhee Lim. He grew up with his older brother Kwanhee Han in Janghowon, a small town in Icheon-si, Kyunggi-do, South Korea, while attending Janghowon Elementary, Middle, and High School. After obtaining his B.S. in 2011 and M.S. in 2013 in Chemical Engineering from the University of Seoul, Seoul, South Korea, he joined the Department of Chemical and Biomolecular Engineering at North Carolina State University, Raleigh, NC in Fall 2013. Since joining the group of Prof. Orlin D. Velev in Dec. 2013, his PhD research has focused on understanding the fundamentals behind the dynamic behaviors of anisotropic colloidal particles in external fields under the guidance of Prof. Velev. During his graduate pursuit, he had an internship in Panel Process and Optics Engineering team of Apple Inc, Cupertino, CA in Summer 2016. After completion of his PhD studies in June 2018, Koohee will join the group of Dr. Alexey Snezhko at Argonne National Laboratory, Chicago, IL, where he will pursue post-doctoral research in the field of active matter.

ACKNOWLEDGMENTS

This work would not have been possible without the help and support of many people. First and foremost, I would like to thank Prof. Orlin D. Velev, who has been an exceptional advisor and a wonderful role model. He has guided me in the right direction with his enthusiasm, insight, and positive attitude while helping me to seek intellectual curiosity and creativity by providing a lot of interesting research opportunities.

I respectfully thank Prof. Carol K. Hall, Prof. Jan Genzer, and Prof. Michael D. Dickey, for serving as my committee members and for providing helpful advice throughout my PhD studies. I am very honored to have such a committee composed of very accomplished scientists who are also very kind and friendly people.

I am grateful to past and present members of the Velev research group. I appreciate Prof. Bhuvnesh Bharti who shared his knowledge and research experience with me when I first joined the group. I thank Dr. C. Wyatt Shields IV and Dr. Ugonna Ohiri who have been an excellent colleague and collaborator to work with. I thank Dr. Fuduo Ma who taught me his expertise in AC electrokinetics.

I would like to thank the Research Triangle MRSEC for the financial support and for the education and outreach opportunities throughout my PhD studies. I sincerely appreciate Mrs. Amy Alexander for her kind help with taking care of all administrative services of MRSEC. I would also like to thank the staff members, Mrs. Sandra Bailey, Mrs. Angela Efimenko, Mrs. Joan O'Sullivan and Mr. Mike Mantini, from our department for their kind help and support.

Last, but most importantly, I would like to express my deepest thanks to my family. Their unconditional love, sacrifice, and support have enabled me in all my accomplishments.

TABLE OF CONTENTS

LIST OF TABLES

LIST OF FIGURES

double layer for one half cycle of an AC electric field. Under a horizontal AC electric field with a low frequency (e.g., 0.1–10 kHz), a stronger slip from ICEO around the Au side drives the JP to propel in the direction of the polystyrene (PS) side. Adapted with permission.[158] Copyright 2008 American Physical Society. (**b**) Self-dielectrophoresis of a JP. Under a vertical electric field at a high frequency (i.e., > 100 kHz), the JP travels with its Au side facing forward due to strong induced field gradients between the Au hemisphere and the conducting substrate (bottom, right inset). Adapted with permission.[188] Copyright 2016 American Chemical Society. (**c**-**d**) Asymmetric surface electrohydrodynamic (EHD) flows for particle self-propulsion. (**c**) An asymmetric PS dimer self-propels by asymmetric EHD flows in a vertical electric field, in this case, at frequencies between 1.4 and 6.0 kHz. The top schematic illustrates a dumbbell model where two spheres, A and B, are connected by an imaginary rod. The dimer moves toward the B end since the B particle generates stronger attractive EHD flows. Adapted with permission.[161] Copyright 2015 American Physical Society. (**d**) Circular motion of a L-shaped particle overlaid with its trajectory (left). A schematic of the template used to assemble the L-shaped particle (right). Adapted with permission.[192] Copyright 2017 Royal Society of Chemistry. (**e**-**f**) Self-rectified electrophoretic motion. (**e**) A millimeter-sized diode self-propels on a liquid-air interface due to an applied AC electric field. The rectified DC electric field between the electrodes of the diode leads to electroosmotic flows, propelling the diode in the direction of its anode. Adapted with permission.[163] Copyright 2007 Nature Publishing

Both the (**ii**) 10-cube and (**iii**) 4-cube clusters reveal no net displacement after 10 cycles of the time-symmetric stroke. (**b-c**) Net displacement of the 10-cube and 4-cube clusters under time-asymmetric reciprocal actuations: (**bi**) rapid opening & slow opening strokes; (**ci**) slow opening & rapid opening strokes. A snapshot of the 10-cube cluster overlaid with 5 frames at an interval of 1 sec. reveals the net (**bii**) upward and (**cii**) downward displacement under the applied magnetic field in (**bi**) and (**ci**), respectively. A snapshot of the 4-cube cluster overlaid with 5 frames at an interval of 4 sec. reveals the net (**biii**) downward and (**ciii**) upward displacement under the applied magnetic field in (**bi**) and (**ci**), respectively. Duty cycle of the signal in (**ai**), (**bi**), and (**ci**): 1 sec. Scale bar: 10 μm. 81

Figure 3.6: The effect of time-asymmetric strokes on the net displacement of a long cluster. (**a**) No net displacement of a cluster with long flapping arms because of lack of local viscosity gradient. The diagram in (**i**) depicts the change in the strength of a magnetic field for time-symmetric actuation. Schematic illustrations of the long cluster with a local viscosity distribution during the (**ii**) opening and (**iii**) closing stroke under the applied magnetic field in (**i**). (**b-c**) Net displacement of the cluster because of a local viscosity gradient induced by a rapid stroke. A diagram depicting the change in the strength of a magnetic field for time-asymmetric actuation: (**bi**) rapid opening & slow closing strokes; (**ci**) slow opening & rapid closing strokes. Schematic illustrations of the cluster with a local viscosity distribution: during the (**bii**) slow closing and (**biii**) rapid

Chapter 1

Introduction: Field-Directed Manipulation and Control of Colloidal Systems*

* Partially based on Han, Shields IV, and Velev, *Adv. Funct. Mater*. **2018**, in press.

1.1 Introduction: from Static to Dynamic Colloidal Systems

Colloidal systems, by definition, represent a multiphase mixture within which the dispersed phase is distributed in the continuous phase (e.g., solid particles in a liquid medium).[1] The classifications of colloidal systems are summarized in **Table 1.1**. depending on types of dispersed and continuous phases.[2] As colloidal systems are highly relevant to our everyday lives (**Table 1.1**), many different aspects of the field of colloid science have been explored. The interactions between the components of a dispersed phase as well as between the dispersed and the continuous phase play a particularly important role in determining the function of a colloidal system.[3–9] For example, when particles in solution are subjected to a net attractive force (e.g., attractive capillary forces during the evaporation of the solvent), they self-assemble into a crystalline structure,[10–12] termed a colloidal crystal.[13–16] Such colloidal assembly techniques have been widely used to generate hierarchically ordered structures from a variety of building blocks ranging in size from molecular to macroscopic.[17–22] While these self-assembled structures have shown promise for a wide range of potential applications such as optics (e.g., photonic crystals) and electronics (e.g., electrodes),[23–30] their practical use has been limited mainly because of their "static" structure.

Table 1.1: Classifications of colloidal systems in everyday use depending on the nature of the dispersed and continuous phases.[2]

Colloidal systems		Dispersed phase		
		Gas	Liquid	Solid
Continuous phase (medium)	Gas	n/a	Liquid aerosol (ex: hairspray)	Solid aerosol (ex: smoke)
	Liquid	Foam (ex: whipped cream)	Emulsion (ex: milk)	Sol (ex: paint)
	Solid	Solid foam (ex: Styrofoam)	Gel (ex: jelly)	Solid sol (ex: ruby glass)

The assembly of "dynamic" colloidal systems for the fabrication of structures with complex on-demand functionality is an emerging topic of intense science interest. In contrast to static colloidal systems stabilized in a global equilibrium state, dynamic colloidal systems involve the transition between local equilibrium states or remain out-of-equilibrium. The former and latter describe reconfigurable structures and active (or self-propelling) structures, respectively. The focus of this dissertation is to investigate the dynamic behaviors of anisotropic colloidal particles powered by external fields and stimuli. An experimental system was designed based on the following parameters: 1) Phases—solid particles dispersed in a liquid medium were considered as a model system. Solid particles can move though the liquid medium in a reasonable time scale (i.e., too slow in a solid medium; too fast in a gas medium), and do not significantly change their size and shape while interacting with each other; 2) Size—approximately 10 μm particles were used to minimize the undesired effect of thermal Brownian motion and facilitate observing their dynamic behaviors in real time using an optical microscope; 3) External stimuli—external magnetic and electric fields were used as a means to power and control colloidal particles. Dynamic responses of the particles were remotely and precisely tuned using parameters such as field direction, frequency, and strength.

1.2 Anisotropic Particles for Colloidal Systems

The advances in micro- and nanofabrication have made the creation of particles with extraordinary complexity a reality. The conceptual framework of anisotropic particles presented by Glotzer and Solomon (**Figure 1.1**)[31] has helped many researchers to develop new, sophisticated methods to create anisotropic particles (i.e., with surface or shape anisotropy) with complex properties. From an engineering perspective, such anisotropic particles can exhibit encoded responses to external

stimuli depending on their design elements such as shape, polarizability and surface functionality. These elements may allow the particles to function as complex structures such as microbots, microswimmers, and microdevices.

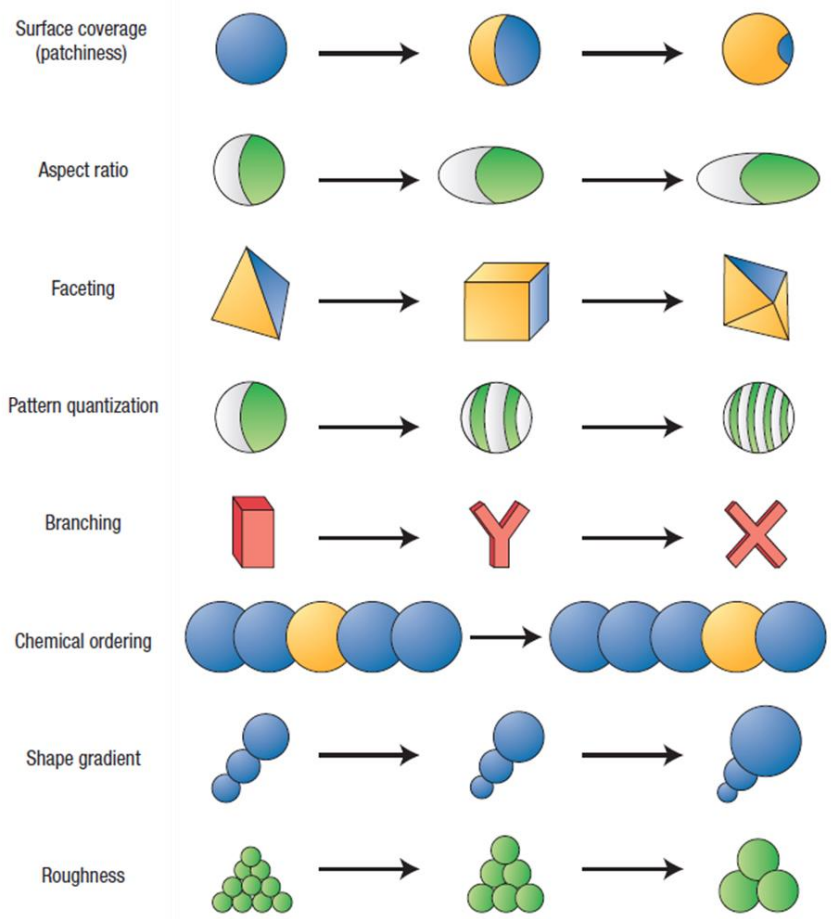

Figure 1.1: Conceptual framework of representative types of anisotropic particles. Key anisotropy attributes of particles are vertically presented where each row shows homologous series of anisotropic particles. Reproduced with permission.[31] Copyright 2007, Nature Publishing Group.

The simplest type of an anisotropic particle is the Janus particle, where one half is physically and/or chemically disparate from the other.[32,33] Metallo-dielectric Janus spheres can be conveniently fabricated by metal evaporation techniques. This method involves forming a monolayer of spheres (e.g., polystyrene) on a solid substrate (e.g., via convective assembly)[34] and then depositing a thin layer of metal (e.g., iron or gold) on top in a direction perpendicular to the

plane.[35] Pawar and Kretzschmar modified this technique by positioning the monolayer of particles at an angle from the metal source (non-perpendicular) to produce patchy particles[36] in a method commonly referred to as glancing angle deposition (GLAD).[37] By this technique, the patch geometry is determined by the angle of vapor incidence and the shadow effects by neighboring particles. Once made, selective chemical modifications can be applied to the metallic side or the non-metallic side to render the particles, for example, biofunctional.[38,39]

Inspired by the design of the helical flagella of some types of bacteria (e.g., *E. coli*), several methods have been developed to fabricate particles with helical structures, including GLAD, self-scrolling of thin films and direct laser writing (DLW).[40] GLAD has been shown to produce large numbers of helical structures with high uniformity.[37,41] A monolayer of silica spheres supported on a solid substrate acts as a seed layer, where the surface of each sphere serves as a nucleation site. After mounting the seed layer at a sharp, glancing angle from the vapor source (e.g., $\alpha \approx 85°$), the substrate continuously rotates with respect to the incoming vapor flux of a magnetic material to allow for the growth of a magnetic helical pillar off of each particle (**Figure 1.2a**).[42] The chirality and pitch of the helical structures are adjustable by changing the direction and speed of rotation. Self-scrolling method[43] has also been used to produce helical shaped structures, whereby conventional thin-film deposition was used to make the base material and a magnetic head was attached to one end using e-beam lithography.[44] Here, a 2D multilayer of monocrystalline thin films was rolled along their crystalline direction into a 3D helical tail. DLW[45] is another method used to fabricate helical structures. This method is based on 3D laser lithography and allows for the fabrication of arbitrary 3D shapes.[46]

The rational design and use of templates has enabled the fabrication of many types of anisotropic particles, as exemplified by anodic aluminum oxide (AAO) template-assisted

electrodeposition (TAE)[47,48] and by soft lithography.[49] AAO TAE has been used to fabricate multi-block rods, the most popular of which is the Au/Pt catalytic nanomotor, which propels by decomposition of hydrogen peroxide.[50] A typical AAO template consists of a nanoporous honeycomb-like structure with pore sizes ranging from 5 to 500 nm in diameter, where the pore diameter determines the rod diameter.[51] As shown in **Figure 1.2b**, the Au/Pt bimetallic rods are obtained after the sequential electrodeposition of Au and Pt into the pores, followed by dissolution of the AAO template (usually with a basic solution). A sacrificial layer (e.g., Ag) is usually first deposited onto the working electrode to allow for facile release and collection of the rods (not shown in **Figure 1.2b**). Other materials (e.g., metals and polymers) can be used for electrodeposition. Also, structures with a larger number of blocks (e.g., tri-blocks, tetra-blocks) can be achieved by additional steps of electrodeposition. Another type of multiblock structure can be obtained by sequential UV polymerization of different compounds on a micromold with pre-designed cylindrical wells.[52] Particle replication in non-wetting templates (PRINT), developed by DeSimone and coworkers, has shown large promise for the generation of anisotropic particles with precise control over their size, shape, composition and surface functionality.[53]

Our group has shown that photolithography in combination with metal evaporation can be used to fabricate a wide range of anisotropically shaped particles with metallic patches.[54] We have recently demonstrated that non-spherical particles with small patches covering small, well-defined regions along the surfaces of the particles can be made using alignment lithography, metal deposition and solvent decoupling, as shown in **Figure 1.2c**. Briefly, we spin-coat photoresist on silicon wafers and transfer a pattern from a photomask to the photoresist to form the body of the particles. Next, we spin-coat a second layer of a different type of photoresist on top. Performing photolithography again with a second photomask containing a set of alignment markers, we can

form defined voids in the second photoresist to create exposed regions on the tops of the particles underneath. The exposed regions of the particles are then coated by metal evaporation. Finally, we separate the first and second layers of photoresist using a mixture of solvents. Conventional photography can be combined with other techniques to produce other types of anisotropic particles. For instance, a photolithography-based microfluidic technique has been used to synthesize polymeric particles with complex shapes and chemistries.[55,56] Shim *et al*. have recently demonstrated that engineering chemical gradients (e.g., of oxygen) during photolithography can provide a means to spatially control the polymerization rate through growth-guiding patterns, allowing for the creation of 3D polymeric particles with precisely determined shapes and compositions.[57]

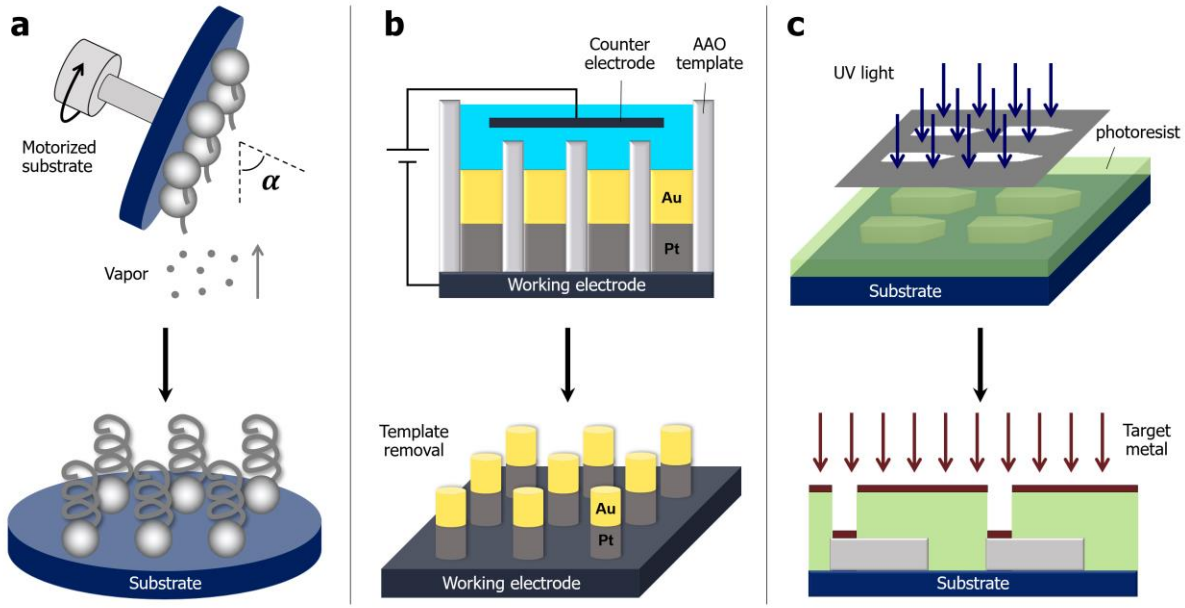

Figure 1.2: Representative methods for the fabrication of engineered anisotropic particles. (**a**) Fabrication of asymmetric helical structures by glancing angle deposition (GLAD) and substrate rotation. Metal vapor is deposited onto a monolayer of spherical particles on a motorized substrate at an angle, α. (**b**) Fabrication of bimetallic rods using anodic aluminum oxide (AAO) template-assisted electrodeposition. After electrodeposition, the AAO template is removed to obtain, in this case, Au/Pt bimetallic rods. (**c**) Fabrication of anisotropic patchy particles using alignment photolithography and metal deposition.

Additionally, simple anisotropic particles can be made from the assembly of isotropic spheres. Velegol and coworkers developed a so-called “salting out-quenching-fusing” technique to generate homodoublets and heterodoublets from particles of the same or of different size.[58] They sequentially aggregated particles into doublets at high ionic strengths, quenched the reaction by diluting the ionic strength and fused the assembled doublets by heating them above their glass transition temperature. Wolf, Isa and coworkers demonstrated sequential capillarity-assisted particle assembly (sCAPA) over topographical templates to assemble isotropic particles into various patterns.[59] Their technique utilizes sequential filling of pre-designed templates with particles of different composition. Other bulk synthetic methods have been used to fabricate anisotropic particles. For example, isotropic polystyrene spheres can be controllably deformed by casting the particles into a stretchable film (e.g., polyvinyl alcohol), melting their cores and stretching the film in one or two dimensions (e.g., one dimensional stretching of the film produces ellipsoids).[60] Swelling of cross-linked polymer spheres by the addition of a polymerizable monomer solution can lead to the controlled deformation of the particles by phase separation and thus the generation of an additional protruding section by further polymerization.[61] If oil is used to swell polymer spheres, the newly formed protrusions can be removed upon evaporation of the oil phase such that particles with dimples can be formed.[62] Oil can also directly nucleate on the particles and deform them when they are melted due to surface tension forces. The use of a polymerizable oil allows for the creation of biphasic particles, where each polymer component can be selectively polymerized and dissolved.[63] Seeded growth and polymerization have been widely used to form core-shell structures, where a core particle can be either concentrically or eccentrically positioned in a polymer shell, depending on the interfacial tension between the core

and shell materials.[82] An eccentric core-shell structure with a magnetic core is often adopted to generate anisotropic magnetic particles.[64,65]

1.3 Field-Directed Assembly of Colloidal Systems

Colloidal assembly has been widely used to generate highly ordered suprastructures from a variety of building blocks through a bottom-up approach.[66–68] One of the most common colloidal assembly techniques is self-assembly, in which disordered components ranging from molecular to macroscopic size form uniformly ordered structures through spatially isotropic interparticle attractions.[69–72] While colloidal self-assembly has produced a range of well-ordered structures such as molecular crystals[73,74] and nanomaterials,[75,76] the lack of the directionality in particle-particle interactions may hinder the fabrication of structures with sophisticated functionality. To further extend the role of self-assembly, it is therefore required to utilize a means for introducing directional particle-particle interactions.[77–80] External magnetic and electric fields can be used to directionally control the assembly of colloidal particles as the field-induced polarization of particles leads to anisotropic interactions between them.[81–86]

When colloidal particles are subjected to external magnetic and electric fields, they polarize and attain a dipole in the direction of the fields.[87] Under both magnetic and electric fields, a significant discrepancy in polarizability between the dispersed (e.g., solid particles) and continuous (e.g., liquid medium) phase is necessary to drive a strong enough attractive interaction potential between the particles leading to their assembly. In the case of magnetic field-driven assembly, a material with high magnetic polarizability should be contained in either a dispersed (e.g., magnetic particles in water) or continuous (e.g., dielectric particles in a ferrofluid) phase. Conversely, in the case of electric field-driven assembly, much less restriction on the selection of

materials exists because the electric polarizability (or permittivity) of most particulate materials is usually different from that of an aqueous medium (e.g., dielectric or conductive particles in water).

Although the physical origin of electric and magnetic dipoles is quite different, once polarized, particles with either an electric or a magnetic dipole similarly interact with each other by dipole-dipole or dipolar interactions. When particles are uniformly polarized (e.g., when they are isotropic), their polarization can be approximated as a point dipole. A simplified equation for calculating point dipole-dipole interaction energy is **Equation 1.1**:[87]

$$E_{\text{int}} = \frac{\mu_0}{4\pi}\frac{1}{{r_{12}}^3}\left[\vec{\mu}_1 \cdot \vec{\mu}_2 - 3\frac{(\vec{\mu}_1 \cdot \vec{r}_{12})(\vec{\mu}_2 \cdot \vec{r}_{12})}{{r_{12}}^2}\right] \qquad (\textbf{Equation 1.1})$$

where μ_0 is the permeability of free space ($4\pi \times 10^{-7}$ m kg s^{-2} A^{-2}), $\vec{\mu}_1$ and $\vec{\mu}_2$ are the dipole moment vector of particles 1 and 2, and $\vec{r}_{12}$ is the position vector between the centers of the particles 1 and 2. As the application of an external field induces the same magnitude and the same direction of a dipole on the particles, Equation (1) can be further simplified as (**Equation 1.2**):

$$E_{\text{int}} = \frac{\mu_0}{4\pi}\frac{\mu^2}{{r_{12}}^3}[1 - 3\cos^2\theta] \qquad (\textbf{Equation 1.2})$$

where μ is the magnitude of the dipole moment for the particles, θ is the angle between a dipole and the line connecting two dipoles, and r_{12} is the center-to-center distance between the two dipoles. Such external field-induced dipolar interactions commonly result in the assembly of long linear chains, which agrees well with **Equation 1.2**; the energy, E_{int}, is at a minimum when θ approaches 0° (**Figure 1.3a**). The simplest example is the formation of "pearl chains" from spherical particles (**Figure 1.3b**).[88] If the concentration of the particles is high enough, the initially formed chains are close enough to attract each other and therefore can further assemble

into close-packed crystalline structures under the continued application of the external field (**Figure 1.3c**).[88]

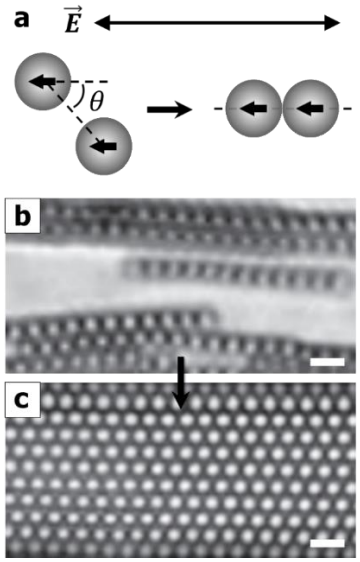

Figure 1.3: External field-driven assembly of isotropic particles. (**a**) Electric dipole polarization of micron-size spherical particles by application of an external alternating current (AC) electric field. Once polarized, two particles self-assemble into a linear chain (i.e., $\theta \rightarrow 0$) to minimize their dipolar interaction potential. (**b**) Assembly of linear chains of particles by application of a horizontal AC electric field. (**c**) Formation of a 2D colloidal crystal from multiple chains by continuous application of the external field. Scale bar: 3 μm. Reproduced with permission.[88] Copyright 2006, Royal Society of Chemistry.

Beyond the simple isotropic particles, the principle of field-induced dipolar interactions can be extended to many other types of dispersions to create advanced functional materials. For example, the structural diversity of an assembled structure can be enhanced using building blocks with shape and/or surface anisotropy.[89–93] Particles with anisotropic shape have formed unusual crystal structures with tunable packing density as exemplified in **Figure 1.4a**.[94] Particles with an anisotropic surface such as Janus particles were used for the assembly of structures with unusual but tailored symmetry resulting from the directional interactions between similar hemispheres (e.g., patch-to-patch attraction; **Figure 1.4b**).[95] The assemblies of anisotropic particles in combination with external fields can form the basis of functional structures as the anisotropic

polarization patterns of the particles can be easily and readily modulated by field parameters including field frequency, strength, and direction.

A characteristic function of the assemblies is structural change, which is attributed to modulating the interaction potential between the constituent particles by adjusting the field parameters.[96] If assembled structures have two (or more) equilibrium states and the potential energy barrier between the equilibrium states is relatively low—for a transition from one to another or a reversible transition between the states—they are considered to be reconfigurable assemblies.[97] In the following sections, representative examples of reconfigurable assemblies generated by external magnetic and electric fields are presented.

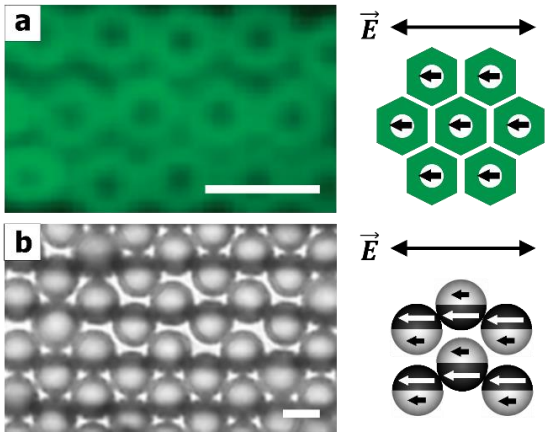

Figure 1.4: External field-driven assembly of anisotropic particles. (**a**) A snapshot (left) and a schematic illustration (right) of a crystal structure assembled from hexnuts in a horizontal AC electric field. Scale bar: 5 μm. Reproduced with permission.[94] Copyright 2008, American Chemical Society. (**b**) A snapshot (left) and a schematic illustration (right) of staggered chains assembled from metallo-dielectric Janus particles in a horizontal AC electric field. Strong electric polarization (white arrow) of the metallic patches (black hemisphere) leads to the formation of staggered chains where the metallic patches are connected in series along the center of the chains. These staggered chains can be further assembled into a crystal structure resulting from the interactions between polarized dielectric bodies (grey hemisphere; black arrow indicates weak electric polarization). Scale bar: 5 μm. Reproduced with permission.[95] Copyright 2008, American Chemical Society.

1.3.1 Magnetic Field-Driven Reconfigurable Assemblies

Janus particles, in which one hemisphere is coated with a material different from that of the core (e.g., a half-metallic patch on a dielectric particle), have functioned as useful building blocks to create hierarchically ordered structures.[98–101] When a magnetic material is used as the coating material, the application of an external magnetic field selectively polarizes the magnetic patch and imparts directional interactions between the magnetic patches. As a result, as shown by Smoukov et al., magnetic Janus particles self-assemble in pre-programmed patterns such as staggered chains, which would be inconceivable for traditional spherical particles (**Figure 1.5**).[102] As long as the field is applied, the assembled structures hold their extended configuration (**Figure 1.5a**) due to the interaction between the external field and the polarized patches. Even after the field is removed, the magnetic patches retain residual magnetization, such that the extended structures do not disassemble but relax and self-reconfigure into a new equilibrium state (**Figure 1.5b**). These permanent structures can be disassembled on demand by demagnetizing the magnetic patches (the inset of **Figure 1.5b**) and reassembled by the reintroduction of a magnetic field.

The assembly and reconfiguration of magnetic Janus particles have also been investigated for the case of application of a rotating magnetic field. As demonstrated in earlier research on the rotating field-driven assembly of isotropic paramagnetic particles,[103,104] magnetic Janus particles can be assembled into a monolayer of hexagonally ordered crystalline structures as shown in **Figure 1.5c**. This phenomenon is due to the well-balanced attractive dipolar interactions between the particles upon the application of a rotating magnetic field with a frequency of 10 Hz and moderate strength (20–50 Gauss).[105] The Janus particles appear opaque in the assembled crystalline structure because the long axis of their magnetic patches align in the direction of the magnetic field at a moment (i.e., facing toward the focal plane). Once assembled, the particles

synchronously rotate with the external rotating field while retaining their hexagonal ordering unless the field strength changes. Upon increasing the field strength (≈ 300 Gauss), the hexagonally packed structure of single particles reconfigures into multiple doublet-clusters as attractive dipolar interactions between the magnetic patches become strong enough to form dumbbell-like doublets between two neighboring particles (**Figure 1.5d**). The formed doublets continue synchronously rotating around their center of mass with the external rotating field of the same strength (**Figure 1.5d**), which is similar to the case of moderate field strength (**Figure 1.5c**).

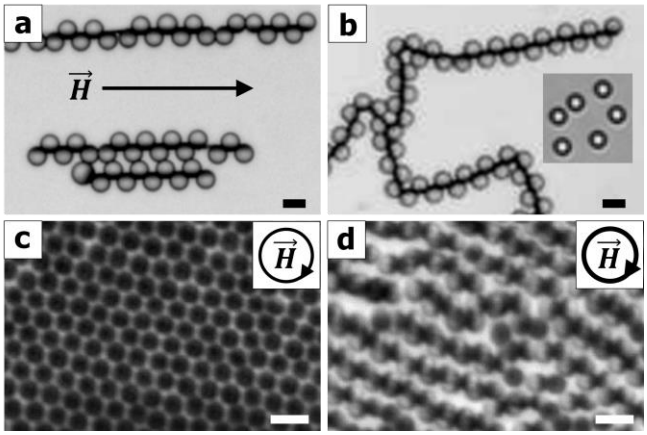

Figure 1.5: Magnetic field-driven reconfiguration of assemblies of Janus particles. (**a–b**) Assembly of Janus particles in a horizontal magnetic field: (**a**) the formation of linear chains of Janus particles by application of the magnetic field and (**b**) reconfiguration of the chains by removal of the field. The inset in (**b**) displays the disassembled Janus particles after demagnetization. Reproduced with permission.[102] Copyright 2009, Royal Society of Chemistry. (**c–d**) Assembly of Janus particles in a rotating magnetic field: (**c**) the formation of a monolayer of hexagonally packed Janus particles in a rotating magnetic field of 20–50 Gauss and (**d**) reconfiguration of the hexagonal structure into multiple-doublet clusters by increasing the strength of the rotating field to 300 Gauss. Scale bar: 5 μm. Reproduced with permission.[105] Copyright 2015, Wiley.

Linker-mediated assembly of isotropic magnetic particles has shown promise for the generation of reconfigurable structures with larger flexibility than the assemblies of Janus particles. For example, Biswal and co-workers demonstrated the assembly of flexible chains of micron-size magnetic particles connected by DNA linkers.[106] Once assembled by a horizontally

uniform magnetic field, the flexibility of assembled chains of particles was determined by the interparticle distance, which is directed by the length of DNA linkers between the particles and the strength of the external magnetic field. While particles connected by short linkers (564 base pairs (bp)) formed rigid chains (**Figure 1.6a**), particles connected by intermediate linkers (2000 bp) formed semi-flexible chains in a field strength of 140 Gauss (**Figure 1.6b**). The assembled chains increased in flexibility as the linker length (4000 bp) increased, and the field strength (19 Gauss) decreased as shown in **Figure 1.6c**. The chains with long linkers (8000 bp) were flexible in a weak field (19 Gauss) and stiffened (e.g., semi-flexible) in a stronger field (140 Gauss) because of stronger particle-particle attractive interactions leading to the entropic exclusion of the linkers between the particles (**Figure 1.6d**). The Biswal group recently demonstrated that such DNA-linked chains (2000 bp) could exhibit a rich variety of dynamic behaviors in a rotating magnetic field where the field frequency determines the dynamics of their rigid rotation, wagging, coiling, and folding.[107]

Velev and co-workers reported that lipid induced-capillary bridging was used as a linker in forming reconfigurable filaments from magnetic nanoparticles.[108] Once magnetic nanoparticles wetted with liquid lipids were assembled into microfilaments by application of an external magnetic field, the filaments remained connected via interparticle capillary bridge formation (**Figure 1.6e**). The liquid nature of capillary bridging between the particles rendered the assembled filaments ultra-flexible. The highly flexible filaments reassembled into bundled filaments as well as unusual structures like ring, infinity, square, and heart shapes in a rotating magnetic field.[109] A critical feature of these filaments is their self-healing capability. Because the nanoparticles within the assembled filaments are linked to each other by capillary bridging, local mechanical damage by a sharp stylus (**Figure 1.6e→f**) can be readily repaired by reforming the capillary

bridges between the disconnected ends during the application of a magnetic field (**Figure 1.6f→g**). Also, the temperature-driven fluid-to-gel and gel-to-fluid phase transition of the lipids within the bridge acted as a thermal switch for the assembly and disassembly of the filaments.

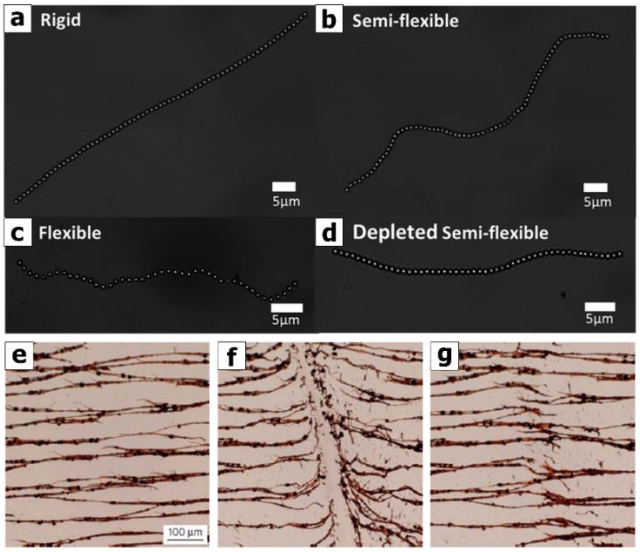

Figure 1.6: Linker-mediated assembly of magnetic particles into flexible filaments. (**a–d**) Assembly of linear chains from micron-size magnetic particles connected by DNA linkers. Depending on the length of the DNA linkers and the field strength, the assembled chains were: (**a**) rigid (564 bp, 140 Gauss), (**b**) semi-flexible (2000 bp, 140 Gauss), (**c**) flexible (4000 bp, 19 Gauss), and (**d**) depleted semi-flexible; the depletion of long flexible linkers (8000 bp) by a strong magnetic field (140 Gauss) resulted in a semi-flexible chain. Reproduced with permission.[106] Copyright 2014, American Chemical Society. (**e–f**) Assembly of ultra-flexible filaments from magnetic nanoparticles connected by capillary bridging: (**e**) formation of flexible linear filaments of magnetic nanoparticles by application of a horizontal magnetic field, (**f**) assembled filaments were fractured locally with a sharp stylus, and (**g**) self-repaired by the reintroduction of the magnetic field. Reproduced with permission.[108] Copyright 2015, Nature Publishing Group.

1.3.2 Electric Field-Driven Reconfigurable Assemblies

The application of external electric fields to particles with anisotropic features (e.g., shape and/or surface anisotropy) provides a way to program multiple modes of assembly patterns. In a pioneering example of this approach, Velev and co-workers reported directed assembly of metallo-dielectric Janus particles in an AC electric field.[95] As shown in **Figure 1.7**, they investigated the

phase transitions between various assembled structures as a function of field strength and frequency, which revealed the critical influence of the field parameters on the patterns of particle assemblies.

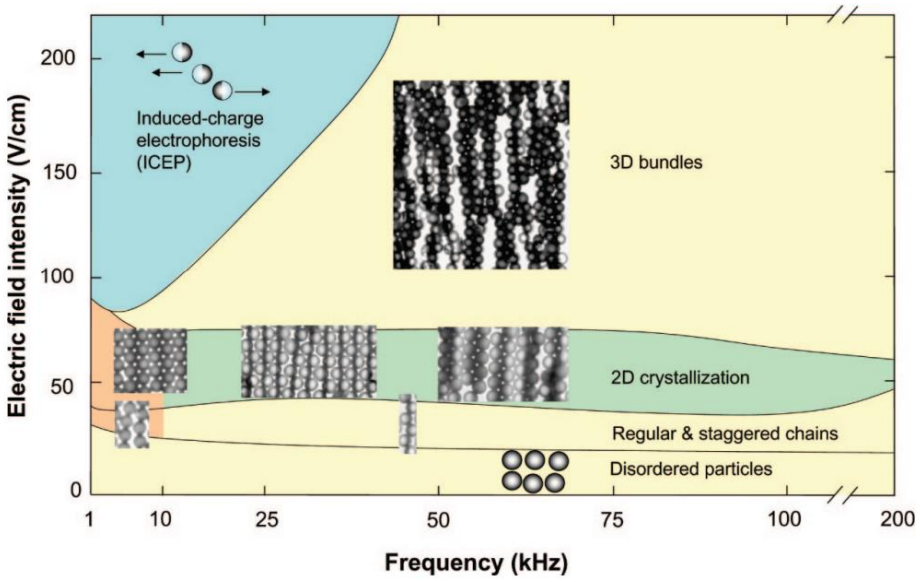

Figure 1.7: A variety of assembly patterns formed from metallo-dielectric Janus particles in an AC electric field depending on the field strength and frequency. Reproduced with permission.[95] Copyright 2008, American Chemical Society.

Following this work, Lewis and co-workers demonstrated how to tune assembly patterns using gold-coated Janus silica rods in a transverse AC electric field.[110] Because an external electric field polarizes both dielectric (e.g., silica) and metallic (e.g., gold) compound, both materials play an essential role in determining the assembly patterns of silica rods. Non-coated silica rods formed linear chains in the direction of the field regardless of the field frequency as their long axis aligned parallel to the field direction. In contrast, tip-coated Janus rods, which the authors referred to as Janus "matchsticks," exhibited field frequency-dependent assembly behaviors. At a field frequency of 100 kHz, the long axis of the Janus matchsticks aligned in the field direction just like the non-coated silica rods. While increasing the field frequency, the Janus matchsticks reoriented at 2 MHz (**Figure 1.8a**) and assembled into staggered bilayers at 3.5 MHz

(**Figure 1.8b**) where the long axis of individual Janus matchsticks aligned perpendicularly to the field direction. As the field frequency increased, the gold patch of the Janus matchsticks played an increasingly dominant role over their silica body in determining their assembled structure, such that the gold patches formed a linear conductive pathway along the center of the bilayers. The authors demonstrated that the assembled bilayers were reconfigurable based on their ability to disassemble and reassemble on-demand. After the field was removed, the bilayers quickly disassembled due to the thermal Brownian motion of each particle. Dispersed Janus matchsticks readily reassembled into a staggered bilayer when the field was reintroduced.

Ma et al. demonstrated the assembly and reconfiguration of symmetric colloidal dimers (i.e., two lobes of the same size) on a conducting substrate in a vertical AC electric field.[111] In a vertical electric field, spherical colloidal particles can be assembled into close-packed crystalline structures due to the electrohydrodynamic (EHD) attraction between the particles.[112,113] The interaction between a polarized particle and the free ions from an adjacent conducting substrate generates attracting EHD flows (i.e., induced-charge electroosmotic (ICEO) flows).[114,115] The authors utilized the EHD flows to assemble colloidal dimers and modulated the competition between the electric and hydrodynamic torques to control assembly patterns by tuning the field frequency. At high field frequencies (~ 6 kHz), they observed close-packed crystals of "standing" dimers (**Figure 1.8c**) where the electric torque between the substrates was strong enough to align each dimer in the field direction. As the frequency decreased, the hydrodynamic torque induced by the ICEO flow increased and became strong enough to dominate over the electric torque such that the standing dimers started lying down and formed crystals of "lying" dimers (**Figure 1.8d**). The authors demonstrated that the assemblies of dimers were reconfigurable based on the orientation change of individual dimers within the assemblies depending on the field frequency.

Also, the on-demand assembly and disassembly of the dimers were exhibited by simply turning the field on and off. The authors also demonstrated that a greater variety of assembly patterns could be produced using asymmetric colloidal dimers (i.e., two lobes having different sizes) as building blocks.[116,117]

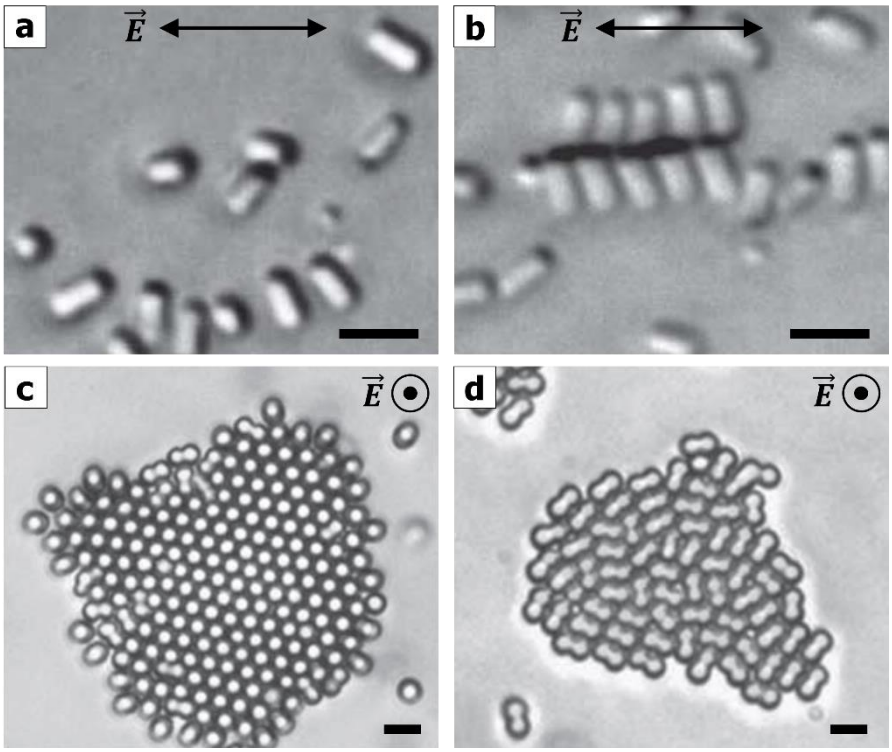

Figure 1.8: Electric field-directed control of assembly patterns of anisotropic particles. (**a–b**) Assembly of Janus matchsticks in a horizontal AC electric field: (**a**) Janus matchsticks began reorienting to co-align their metallic patch in the field direction at 2 MHz and (**b**) self-assembled into staggered bilayers at 3.5 MHz. Scale bar: 3 μm. Reproduced with permission.[110] Copyright 2014, Royal Society of Chemistry. (**c–d**) Assembly of symmetric dimers under a vertical electric field: (**c**) formation of close-packed standing dimers (perpendicular to the surface) at ~6 kHz where each dimer viewed from above appears as a circle in the assembled structure because its long axis aligns in the applied field direction and (**d**) reconfiguration of close-packed standing dimers into close-packed lying dimers (parallel to the surface) at ~0.6 kHz. Scale bar: 3 μm. Reproduced with permission.[111] Copyright 2012, Wiley.

Beyond controlling assembly patterns of colloidal particles under external fields, directional reconfiguration of assembled structures such as contraction and elongation was produced by modulating polarization patterns of each particle within the assemblies. For example,

Kretzschmar and co-workers demonstrated the contraction of chains assembled from Fe_3O_4-capped Janus particles in overlapping external electric and magnetic fields.[118] When an AC electric field is applied solely, the Janus particles assembled into staggered chains in the field direction (**Figure 1.9a**). Upon successive application of a parallel magnetic field, the staggered chains reconfigured into double chains in which Fe_3O_4 patches were connected in series along the center of the assembled chains (**Figure 1.9a→b**). This dynamic reconfiguration (i.e., chain contraction) was driven by the newly added magnetic dipolar interactions between the Fe_3O_4 patches. The staggered chains initially formed by the electric field provided an optimized reaction vessel for the formation of double chains. Although this chain contraction was irreversible because of the residual magnetism in the Fe_3O_4 patches, the authors showed that the reconfiguration dynamics of the contraction process can be employed to measure the local viscosity of the surrounding medium.[119]

The electric dipolar interactions can be utilized to address the issue of irreversible reconfiguration of permanent magnetic polarization because the electric polarization of materials disappears immediately after the electric field is removed. For example, Solomon and co-workers demonstrated that assemblies of gold-coated Janus polystyrene ellipsoids can be reversibly elongated and contracted via toggling an external electric field.[120] The Janus ellipsoids self-assembled into the ordered fiber (OrF) equilibrium structures at a salt concentration of 5 mM. The reduced electrostatic repulsion between the particles facilitated gold-gold binding within the assemblies. Upon application of an external electric field, the OrF structures reconfigured into chain-link (CL) structures with elongation of a four-particle unit cell (i.e., from a to $\sqrt{2}a$; **Figure 1.9c→d**) driven by the induced electric dipolar interactions between the gold patches. Once the electric field was removed, the induced electric dipole in the gold patches no longer existed such

that the CL structures snapped back into the OrF structures with contraction of the unit cell (i.e., from $\sqrt{2}a$ to a; **Figure 1.9d→c**). Such chain elongation and contraction were completely reversible by merely turning the field on and off, which could find applications in artificial muscles and shape-memory materials because the potential energy barrier between the OrF and CL state was relatively low.

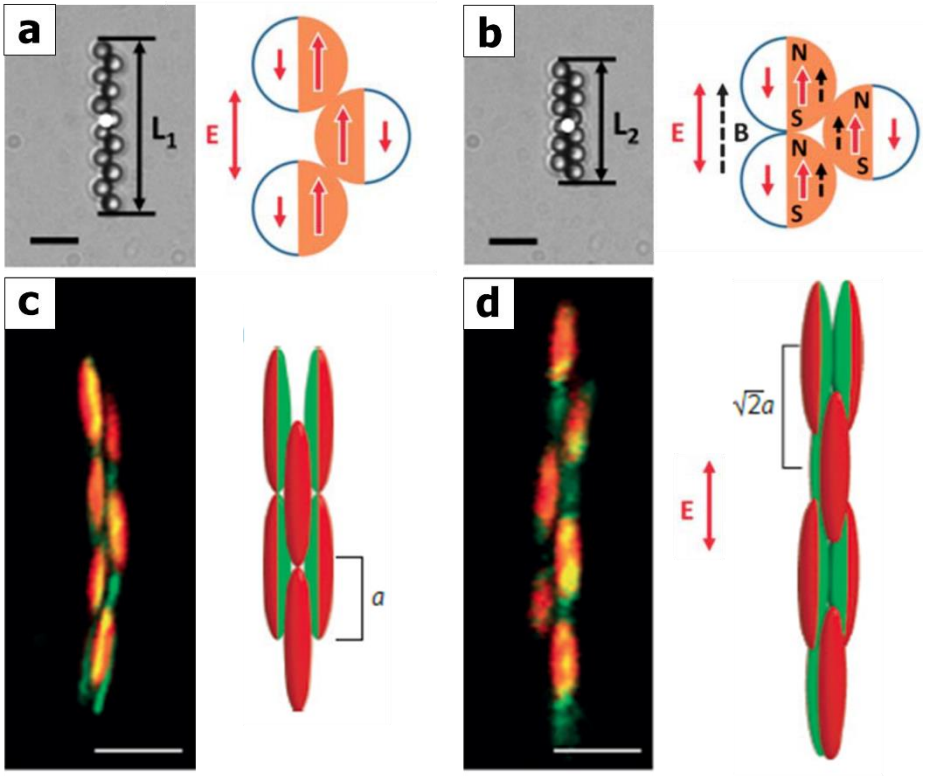

Figure 1.9: Electric field-driven directional reconfiguration of assemblies of anisotropic particles. (**a–b**) Contraction of a chain of Janus spheres in overlapping magnetic and AC electric fields: (**a**) formation of a staggered chain from Janus spheres in an AC electric field and (**b**) contraction of the staggered chain into a double chain ($L_1 > L_2$) upon subsequent application of a parallel magnetic field. Scale bar: 10 μm. Reproduced with permission.[119] Copyright 2013, American Chemical Society. (**c-d**) Reversible elongation and contraction of an assembly of Janus ellipsoids by toggling an external AC electric field: (**c**) self-assembly of an ordered fiber (OrF) structure with a four-particle unit cell (a represents the unit cell size) from Janus ellipsoids at a salt concentration of 5 mM and (**d**) reconfiguration of the OrF structure into a chain-link (CL) structure with elongation of the unit cell from a to $\sqrt{2}a$ upon application of an external AC electric field. The CL structure snapped back into the OrF structure upon removal of the field. Scale bar: 3 μm. Reproduced with permission.[120] Copyright 2014, Nature Publishing Group.

Assembling these simple anisotropic particles in external fields has shown promise in generating the early examples of reconfigurable structures. The next frontier in this field is increasing the complexity of assembly patterns and diversifying the functionalities of assembled structures to make microbots and microdevices. One approach is using more complex anisotropic particles as building blocks. Examples of such building blocks include a large variety of shaped particles with metallic patches along specific regions of their surfaces.[121] These complex particles and assemblies can attain another level of dynamic functionality by being made of active (or self-propelling) particles, which will be introduced in the following sections.

1.4 Field Powered Self-Propelling Particles

In recent years, researchers have developed ways to create anisotropic particles with sophisticated design elements such as shape, polarizability, surface pattern (e.g., biofunctional patches) and bulk functionality (e.g., integrated circuits and scaffolds for drug release).[31] The particles with these design element may form the basis of building self-propelling microbots and microdevices. A schematic example of a hypothetical self-propelling particle that possesses each of these design elements is illustrated in **Figure 1.10**. The asymmetric shape of this engineered particle allows it to harvest energy from external fields for directed propulsion (the possible mechanisms for which are discussed later). Its direction of propulsion can be steered by, e.g., a magnetic field through the magnetic torque between the field and the magnetic patch. Additional functionalities can be incorporated into the bulk of such particles, via so-called device integration, and onto the surfaces of the particles. For instance, doping crystalline silicon with boron, phosphorus or other atoms can lead to the formation of p-n junctions, as a basis of making microdiode particles.[122] Further, biosensing patches can be added to the surfaces of the particles to recognize key biomarkers (e.g.,

cytokines, viruses or DNA), which may enable the realization of motile particle-based biomedical assays.[123]

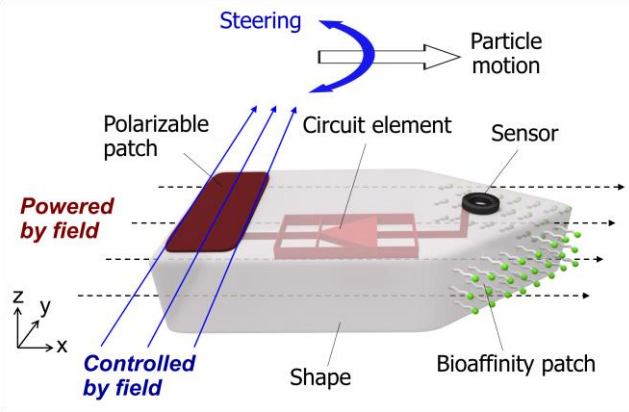

Figure 1.10: Schematic example of a field-powered, self-propelling particle with representative design elements. A hypothetical engineered particle may self-propel by transducing energy, in this case, from an external electric field along the x-axis (black dotted lines), into a local gradient. A magnetic patch can be used as an additional means of control (e.g., to impart torque) for steering, in this case, via an external magnetic field that rotates around the x/y-plane (blue lines). The bulk material of the particle can be modified (e.g., doped to form a p-n semiconductor junction) to rectify an external electric field, as in this case, towards a microdiode particle. A sensor connected to the circuit can be used to control the motion of the particle (e.g., turning on or off the diode) by responding to external stimuli (e.g., light). Bioaffinity tags (e.g., antibodies or aptamers), as shown along the front of the particle, can be used to capture bioanalytes in solution, allowing the particle to serve as a self-propelling biosensor.

Unlike particles that move in response to gradients of force or energy, active particles draw energy from their environment to autonomously self-propel. To illustrate this difference, we compare schematically a particle driven by a field gradient and a particle driven by active propulsion in **Figure 1.11**. **Figure 1.11a** shows the case where an externally applied field gradient is used to pull a particle toward a field maximum. We note that the forces are dependent on the relative polarizabilities of the particles and media, thus their direction can change. For example, a particle that is less polarizable than the medium will be repelled from the field maximum (e.g., a dielectric particle in a ferrofluid near a magnet). Such types of motions are well understood in the form of magnetophoresis,[124] electrophoresis,[125] dielectrophoresis,[126] acoustophoresis[127] and

thermophoresis.[128] A self-propelling particle, in contrast, converts energy from its surroundings into a local gradient, leading to active self-propulsion (**Figure 1.11b**). As discussed above, diverse dynamic patterns can be encoded into the design of an engineered active particle.

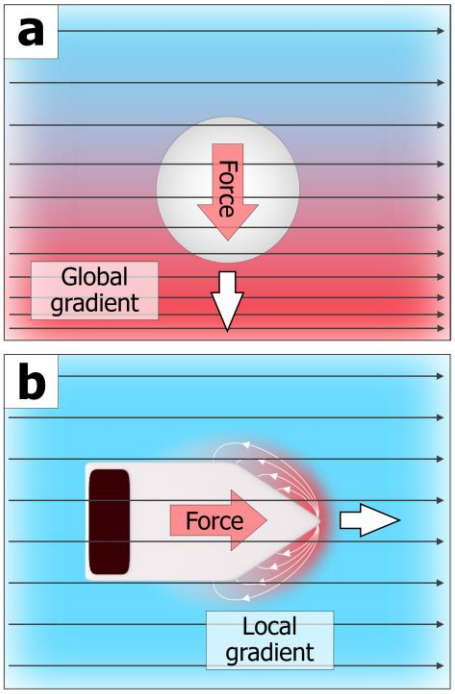

Figure 1.11: Schematic comparison of the origin of motion of a non-active (global field gradient-driven) and an active (local field gradient-driven) particle in an external field. (**a**) A non-active, spherical particle with tri-axial symmetry is pulled by a positive gradient toward the field maximum (downward). (**b**) An engineered active particle moves itself rightward by transducing energy from a uniform external field to generate a local field gradient. The gradient is indicated by a change in color from blue to red, which is global for (**a**) and local for (**b**).

A rationally engineered active particle can harvest energy from its surroundings (e.g., from liquid fuel or external fields) and convert it into local gradients driving asymmetric fluid flows around the particles to induce their motion. The most common means for powering active particles include catalytic fuels as well as acoustic, optical, magnetic and electric fields. While we focus on the design and locomotion of active particles powered by magnetic and electric fields, such basic engineering principles can be applied to particles powered by catalytic,[129–134] acoustic[135–139] and optical[140–146] energy sources.

The main mechanism for powering active particles by magnetic fields is based on mechanical generation of asymmetric hydrodynamic flows (i.e., asymmetric fluid drag; **Figure 1.12a-c**). When subjected to a uniform magnetic field, a magnetically responsive particle undergoes torque to align its easy axis with the direction of the applied field.[147] Accordingly, a rotating or an oscillating magnetic field generates corresponding particle movements below a certain critical rate or frequency.[148] When a rotating field is used as a power source, the velocity of active particles is usually proportional to the frequency of the field, as long as the particles rotate synchronously with the field. Above a critical frequency, the particles do not have sufficient time to align their magnetic dipole with the field, and thus the velocity decreases and often ceases. The inspiration for several types of active magnetic particles comes from biological microorganisms observed in nature. The most prominent examples are particles with a rigid helix for generating rotational motions (**Figure 1.12a**; inspired by the motion of bacterial flagella) and particles with a flexible filament for generating beating motions (**Figure 1.12b**; inspired by the motion of eukaryotic flagella). Even though these particles are driven in different way, the movement resulting from their slender tails generates a net imbalance of drag along their tails. More specifically, such particles move parallel to their body length because drag in the perpendicular direction is greater than the drag in the parallel direction (**Figure 1.12a, b**).[149–151] Another type of active motion is seen with magnetic rotors (e.g., magnetic rods and dimers with asymmetric lobes) in surface-assisted motion.[152,153] In the presence of a rotating magnetic field, these particles exhibit a tumbling motion when placed in the proximity of a wall or surface (**Figure 1.12c**). As stronger frictional forces (and thus stronger drag forces) exist near the wall, the center of rotation is shifted toward the wall and thus the distal end of the particle moves faster, as depicted in **Figure 1.12c**, resulting in a net displacement with each rotation. Since this mechanism of propulsion is

applicable to other particle designs, we believe that a variety of motions could be attained using similar principles.

The mechanism for powering active particles by electric fields is usually based on the generation of asymmetric flows from induced charges around the particle (**Figure 1.12d-f**). Alternating current (AC) electric fields are usually applied to generate these motions instead of direct current (DC) electric fields, as to eliminate the effect of electrophoresis; although, we note that a few examples of active particles powered by DC electric fields have also been reported.[154–156] An external electric field polarizes a particle, accumulating counter charges in the electric double layer (EDL) around the particle and acts on these induced charges to drive an electroosmotic flow. The direction of this flow is dictated by the type of the particle and the direction of the field.[157] Breaking the surface symmetry of the particle (e.g., Janus sphere) into a more polarizable half and a less polarizable half can induce its active propulsion in an AC electric field (**Figure 1.12d**).[158] When an electric field is applied, the EDL on the metallic side is more strongly polarized than that on the dielectric side. As a result, stronger induced-charge electroosmosis (ICEO) occurs around the metal region (as depicted by red arrows in **Figure 1.12d**), which propels the particle with the dielectric side facing forward. This mechanism of propulsion is referred to as an induced-charge electrophoresis (ICEP).[159] Such ICEO persists only in between lower and upper characteristic frequencies, where the lower and upper limits are determined by the resistive-capacitive (RC) time for the formation of the EDL around the electrodes and the particle, respectively.[158] In comparison to classical electroosmosis, where the velocity of the particle is proportional to the strength of the applied electric field due to the constant charge density of the EDL around the particle, ICEO (and correspondingly ICEP) features a

quadratic dependence on the field strength, where the charge density of the EDL around the particle is proportional to the field strength.

Without a difference in polarizability, asymmetry in shape can also generate active motions when subjected to an electric field, for example, between two conducting plates, as illustrated in **Figure 1.12e**. In a vertical electric field, a charged particle near the bottom substrate experiences electrohydrodynamic (EHD) flows resulting from the interaction between the induced dipole of the particle and the induced charges in the EDL of the substrate.[160] Breaking the symmetry of such EHD flows can lead to propulsion.[161] For example, in case of the particle shown in **Figure 1.12e**, the large lobe generates stronger repulsive EHD flows than the small lobe, leading to motion with the small lobe facing forward. However, this effect can be reversed at certain frequencies and is also dependent on the size, shape and composition of the particle, as discussed in detail by Wu and coworkers.[161,162] Since the dipole of the particle and the charges close to the substrate are both induced by the applied field, the velocity of the particle is proportional to the field strength squared.

Another mechanism for electric field-powered propulsion is based on field rectification from a diode-containing particle (**Figure 1.12f**).[163] The application of an AC electric field along the body of a diode can induce a local DC electric field because of the role of the current-rectifying element inside of the particle. Since only half of each cycle of the AC electric field results in one-directional electrical current through the diode, induced charges on the diode surface also move in one direction, leading to DC electroosmotic flow in that direction and propulsion in the opposite direction. This effect allows the diode particle to move at the same speed regardless of the frequency of the AC electric field. The velocity of the diode is proportional to the strength of the applied AC electric field, as the electroosmotic flux is induced by the rectified DC voltage.

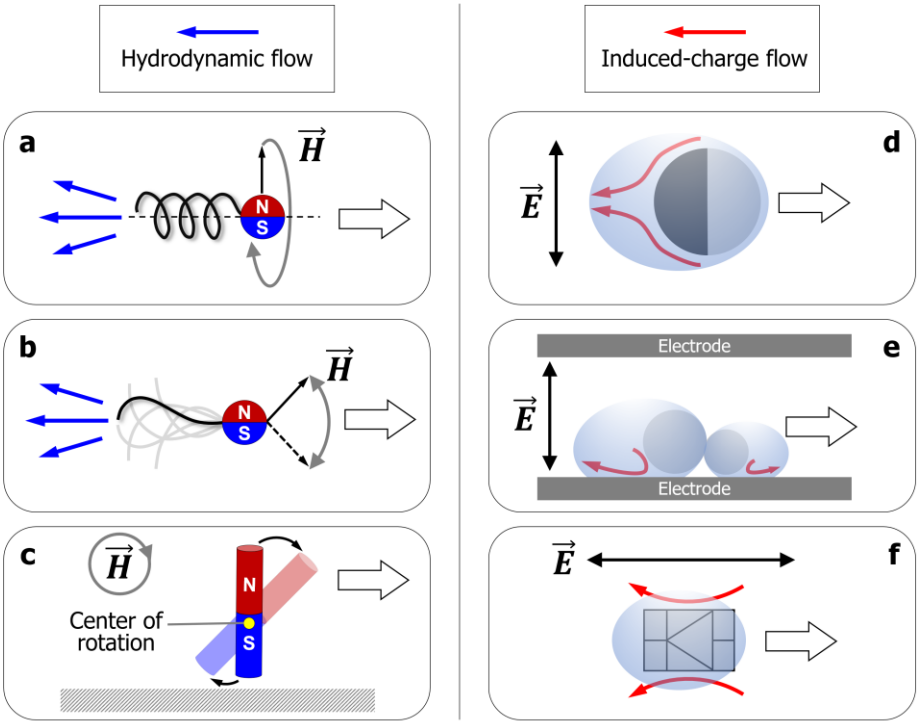

Figure 1.12: Methods for powering the active propulsion of particles by magnetic and electric fields. (**a-c**) Asymmetric hydrodynamic flows generated by external magnetic fields. (**a**) Axial propulsion of a rigid helical body by a rotating magnetic field. (**b**) Traveling-wave propulsion of a flexible magnetic flagellum by an oscillating magnetic field. (**c**) Surface-assisted propulsion of a magnetic rod by a rotating magnetic field. (**d-f**) Asymmetric induced-charge flows generated by external AC electric fields. (**d**) Induced-charge electroosmosis of a metallo-dielectric Janus particle. In a horizontal AC electric field, the more strongly polarizable metallic side (black hemisphere) generates a stronger electroosmotic slip (red arrows), resulting in motion toward the dielectric side (gray hemisphere). (**e**) Asymmetric surface electrohydrodynamic (EHD) flows of a fused particle dimer. In a vertical AC electric field, the dimer experiences surface EHD flows adjacent to the conducting surface (red arrows). Unbalanced EHD flows around the dimer leads to motion, in this case, in the direction of the smaller particle. (**f**) Self-rectified electroosmosis of a diode particle. The embedded diode rectifies an external AC electric field into a local DC electric field, leading to self-electroosmotic flows (red arrows).

1.4.1 Magnetic Field-Driven Self-Propelling Particles

Helical propulsion is one of the most popular ways to power active particles by magnetic fields due to the ease of fabrication. Using the rolling technique, Nelson and coworkers developed the first prototype of an active helical particle, which they named an artificial bacterial flagellum (ABF).[44] Its rigid body (47 μm in length) generated propulsive thrust along its long axis due to

rotation induced from a magnetic field, while its magnetic head (4.5 μm in length) remained aligned with the field (**Figure 1.13a**).[164] The ABF can move in three dimensions using three orthogonal pairs of electromagnetic coils. They can also exhibit forward and backward motions by changing the direction of the rotating field. The authors demonstrated the 3D locomotive control capabilities of the method by capturing and transporting a 6 μm particle using an ABF with a microholder fabricated by the DLW technique, described earlier.[45] More recently, Schmidt and coworkers employed similar helical structures to assist in the fertilization process by mounting naturally immotile sperm cells on motile microhelices and transporting the sperm-helix hybrids to oocytes.[165] Using the GLAD technique (**Figure 1.13a**), Fischer and coworkers fabricated smaller, nanoscopic helical structures with a non-magnetic head and a magnetic tail.[166,167] Their nanostructured helical propellers (~70 nm in diameter) allowed the particles to swim through complex viscoelastic media with mesh sizes in the range of tens to hundreds of nanometers (**Figure 1.13b**).[167]

Despite the conceptual simplicity of particles that move by traveling-wave propulsion, the reproducible fabricatation of such types of particles on the microscale remains a challenge. Dreyfus *et al*. developed an artificial flagellum by assembling a flexible filament from magnetic particles linked by hybridized strands of DNA (**Figure 1.13c**).[168] The authors attached a red blood cell to one end of the filament to break the time-reversal symmetry in the motion of the filament. In an oscillating magnetic field, the filament directionally pulls the attached cell because the undulatory motion of the filament propagates from the free end to the tethered end. Spermatozoa, in contrast, move in the direction of their head, as the undulatory wave propagates from head to tail, which is similar to the model illustrated in **Figure 1.12b**. Such types of structures have also been experimentally demonstrated on a millimeter scale.[169,170] Gao *et al*. have demonstrated

traveling-wave propulsion of a flexible nanoparticle fabricated by TAE (**Figure 1.13d**).[171] After synthesizing the Au/Ag/Ni tri-metallic-block, partial dissolution of the center Ag layer has been performed in hydrogen peroxide to create a flexible joint.[172] In a rotating magnetic field, the presence of the flexible Ag joint facilitates rotation of the magnetic Ni tail along a concentric patch, which causes rotation of the non-magnetic Au head at a lower amplitude. As a result, the broken symmetry in the cyclic deformation between two ends leads to propulsion. Following this research, the same fabrication approach has been adopted to produce other complex geometries of flexible nanowires capable of undulatory locomotion.[173–175]

In comparison to the previous mechanisms, the surface-assisted propulsion mechanism is relatively easier to implement since it only requires a rotating magnetic field and a material with magnetic anisotropy that can rotate with the field placed near a solid boundary. The simplest example of this is the tumbling motion of rigid Ni nanowires (200 nm in diameter and 10-30 μm in length, synthesized by TAE) near a solid surface in water (**Figure 1.13e**).[152] As shown in the inset of **Figure 1.13e**, given the torque (τ_{m}) induced by a rotating magnetic field, the Ni wire moves slower at the "b" end at this point in its cycle due to a stronger fluid drag, caused by viscous friction, near the solid boundary in comparison to the liquid boundary at the "a" end. This allows the particle to follow a prolate cycloid trajectory, which is responsible for its active propulsion. Since these asymmetric boundaries are present at any solid surface in contact with a liquid suspension, the Ni wire can traverse and scale complex topographies, such as beveled surfaces and walls. Tierno and coworkers showed the tumbling motion of asymmetric magnetic dimers (2.8 and 1.0 μm in each diameter) linked by hybridized DNA strands on a flat plate in a precessing magnetic field (**Figure 1.13f**).[176] This motion is also attributed to the asymmetric viscous frictional forces, which in this case, are encountered during the rotation of the small lobe in the x/z-plane (i.e., the

friction is higher when the small lobe is closer to the plate). The authors also provided a detailed theoretical analysis of these experimental results.[177] Other types of particles or structures, which can perform surface-assisted propulsion, include polymer spheres with an embedded magnetic cube,[178] microrods,[179] *in situ*-assembled colloidal asters,[180,181] wheels,[182] carpets,[104] lassos[183] and chains.[184]

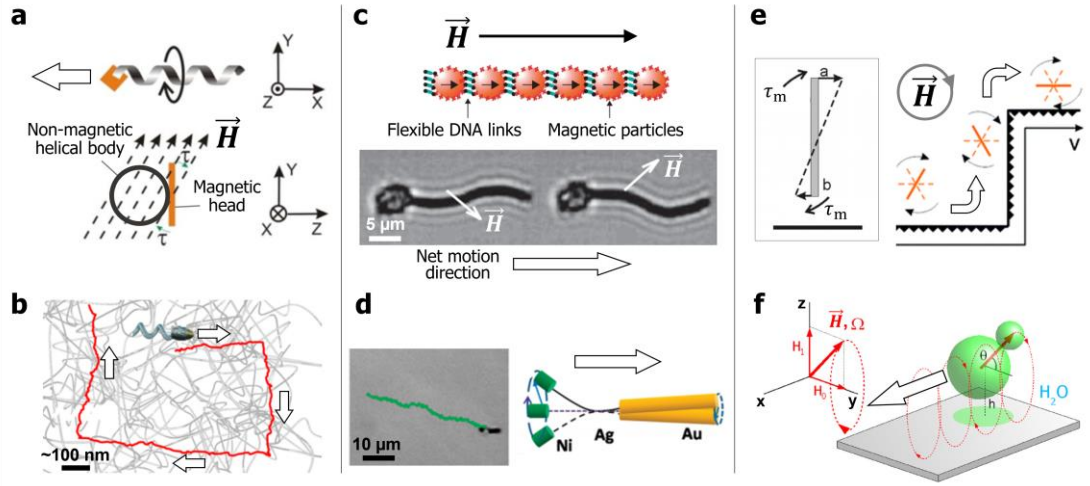

Figure 1.13: Representative examples of magnetically powered self-propelling particles. (**a**-**b**) Helical propulsion. (**a**) Artificial bacterial flagellum (ABF) consisting of a magnetic head bound to a non-magnetic helical tail. In a continuously rotating magnetic field, the ABF head remains aligned with the field, resulting in rotation and propulsion from the helical tail. Adapted with permission.[164] Copyright 2009 American Physical Society. (**b**) Schematic of a nano-helical swimmer passing through a gelatinous network. Adapted with permission.[167] Copyright 2014 American Chemical Society. (**c**-**d**) Traveling-wave propulsion. (**c**) A flexible artificial flagellum consisting of a chain of magnetic particles connected by flexible DNA linkages. Under an oscillating magnetic field, the flexible magnetic tail that is attached to a red blood cell moves in the direction of its free end by a field-induced undulating motion. Adapted with permission.[168] Copyright 2005 Nature Publishing Group. (**d**) A magnetic nanowire swimmer consisting of an Au head and Ni tail is linked by a flexible Ag bridge. Under a rotating magnetic field, the flexible bridge allows the tail to freely rotate and as the head rotates at a different amplitude, the breaking of the symmetry of the system leads to propulsion. Reprinted with permission.[185] Copyright 2010 American Chemical Society. (**e**-**f**) Surface-assisted propulsion. (**e**) A rigid Ni nanowire near a solid surface in water. When subjected to a rotating magnetic field, the asymmetric boundary condition around the particle, as shown in the inset, allows the particle to propel along the wall. Reprinted with permission.[152] Copyright 2010 American Chemical Society. (**f**) A paramagnetic, asymmetric dimer on a glass plate. Under a magnetic field precessing about the y-axis, the dimer propels along the x-axis due to the periodic rotation of the small lobe in the x/z-plane (i.e., about the y-axis). Reprinted with permission.[176] Copyright 2008 American Physical Society.

1.4.2 Electric Field-Driven Self-Propelling Particles

Motion by ICEP typically occurs in particles with asymmetric polarizability. This effect was experimentally observed by our group[158] using metallo-dielectric Janus particles (JPs) fabricated from the deposition of a thin Au film (20 nm) onto the top half of a monolayer of polystyrene spheres (PS, 4.0-8.7 μm). This effect has been predicted by Bazant and Squires with a model of a metallic cylinder with an insulative coating on one side.[159] The JPs were suspended in water and placed in a horizontal AC electric field at low frequencies (i.e., between 0.1–10 kHz; **Figure 1.13a**). The low frequencies allow time for the charging of the EDL, where the EDL of the Au coating has a much higher induced charge because of its stronger polarizability. As a result, stronger slip from ICEO occurs along the Au side of the particles, leading to ICEP in the direction of the PS hemisphere, as shown in **Figure 1.13a**. In a horizontal electric field, the direction of motion is always perpendicular to the direction of the field, with two possible orientations (e.g., bidirectional movements in the snapshot of **Figure 1.13a**) due to the torque between the applied field and the long axis of the metallic coating. Recently, Lavrentovich and coworkers experimentally described the patterns of such flows from ICEO around immobilized metallo-dielectric JPs made from silica and Au using fluorescent tracers and microparticle image velocimetry.[186] The authors also demonstrated the propulsion of symmetric particles in liquid crystals in AC electric fields, which broke the symmetry of the medium (i.e., distortion of the orientation of liquid crystal molecules around the particles) rather than of the particles.[187]

Boymelgreen *et al*. recently showed that metallo-dielectric JPs can also exhibit active motion in the opposite direction (i.e., with the metallic side facing forward) in a vertical electric field between two conducting substrates at high frequencies (i.e., > 100 kHz). The authors refer to this type of motion as self-dielectrophoresis (**Figure 1.13b**).[188] Conventional dielectrophoresis

(DEP) should be distinguished from this mechanism because it is a result of a gradient between particles in an AC electric field, causing them to attract.[81,189] The authors experimentally and numerically confirmed this self-DEP effect in a high-frequency electric field, by revealing the presence of strong, localized field gradients between the surfaces of the Au coatings and the bottom conducting substrate, as shown in the inset of **Figure 1.13b**. The asymmetric gradients on the Au side of the particle act on the induced dipole of the particle, as in DEP, but on a single-particle level, leading to propulsion with the Au hemisphere facing forward. More recently, the same authors utilized self-DEP as a means to collect and transport neighboring particles.[190] On the basis that ICEP and self-DEP operate at different frequency regimes, the JPs can controllably shuttle back and forth by changing the electric field frequency.[188,191]

The motion of engineered active particles can also be induced by asymmetric EHD flows between the particles and a conducting substrate in electric fields at low frequencies (i.e., 0.1–10 kHz). Since the migration of the induced charges from the substrate toward the particles results in such EHD flows, particles with asymmetric polarizability are not required, in contrast to ICEO. Rather, more general types of particle asymmetry (e.g., geometry, composition and surface charge) can be used to achieve unbalanced EHD flows.[161] Ma *et al*. utilized this concept to propel dielectric particle doublets whose ICEO was negligible due to their weak polarizability.[117] Such a particle can self-propel when placed on a conducting substrate and subjected to a vertical AC electric field. As an example, the authors demonstrated the active motion of asymmetric dimers (made from 2 and 3 μm PS spheres fused together by the salting out-quenching-fusing technique; **Figure 1.13c**).[161] Depending on the frequency of the electric field, the asymmetric dimers can move in opposite directions, which is attributed to the transition between attractive and repulsive EHD flows (e.g., the transition frequency is ~1.4 kHz for the asymmetric PS dimers shown in

Figure 1.13c when suspended in 10^{-5} M KCl). The direction of propulsion is determined by the asymmetry of the constituent particles, as illustrated in the top schematic of **Figure 1.13c**. The authors also demonstrated that symmetrical hybrid dimers (made from 2 μm spheres) with asymmetric compositions or surface charges exhibit similar propulsion behaviors. The authors derived an analytical expression to estimate the EHD streamlines, including the flow direction (i.e., from attractive or repulsive EHD flow), for all of their particle dimers. Following this work, Ni *et al*. investigated the EHD flows of geometrically and compositionally asymmetric particles made by sCAPA.[192] For example, the authors demonstrated the circular motion of a L-shaped particle assembly (**Figure 1.13d**, left) from a L-shaped template (**Figure 1.13d**, right) by sequentially filling the template with isotropic spheres.

Another type of electrically powered active motion is by self-rectified electrophoresis in a semiconductor diode particle, which constrains the electrical current to flow in one direction. Our group originally demonstrated this propulsion mechanism using commercial diodes (1.0 and 3.7 mm in length) floating on the surface of water in a horizontal AC electric field (**Figure 1.13e**).[163] The diodes rectify the externally applied AC electric field by converting it into a local DC electric field between its electrodes. When the diode is positively charged, the DC electric field drives the negative charges in the EDL around the surface of the diode toward the cathode and thus the diode propels in the direction of the anode, as illustrated in **Figure 1.13e** (the opposite is true when the diode is negatively charged). In a horizontal field, the direction of motion is always parallel to the field, whereby the diode can move either left or right depending on its orientation. This unusual class of circuit-based particles can also be endowed with a range of additional electrical and sensing functionalities. For example, the local DC voltage can be used to power other types of diodes with pre-programmed functions, such as light emitting diodes that can move and emit light

as well as photodiodes, where the movement of the particle stops when illuminated with a strong light source.[163] Our group also showed that the flows generated by diodes in an AC electric field can be used to pump and mix liquids in microfluidic channels when the diodes are immobilized within a microfluidic device.[193] Recently, we demonstrated a way to remotely steer the diodes by electrically modifying the applied AC signal (i.e., by introducing wave asymmetry).[194] Concurrently, Wang and coworkers achieved dramatic miniaturization of such diodes, by using the TAE technique to fabricate nanowire diodes (e.g., Cd/Polypyrrole) and showed that self-rectified electrophoretic motion in AC electric field does not depend on the diode particle size (**Figure 1.13f**).[195]

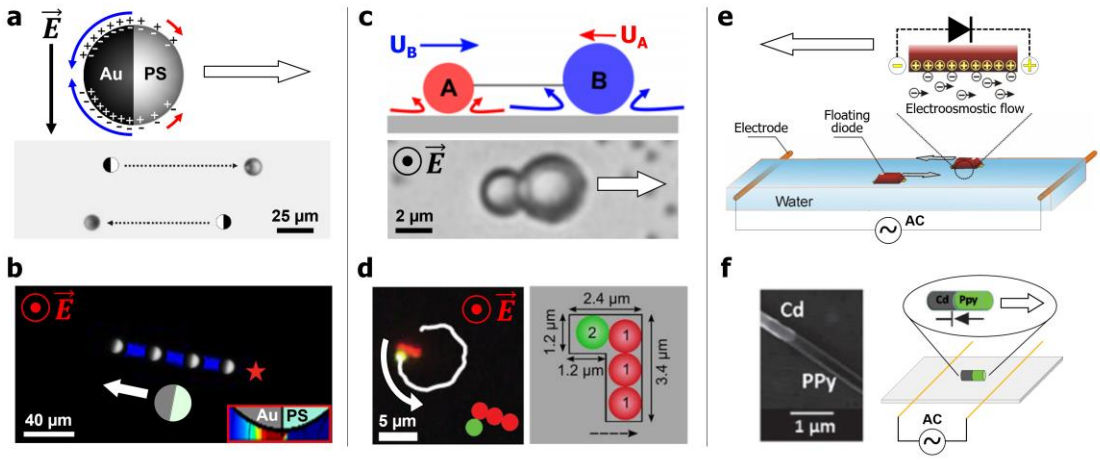

Figure 1.14: Representative examples of electrically powered self-propelling particles. (**a**) Induced-charge electrophoresis of a Janus particle (JP). The schematic on the top depicts the induced-charge electroosmotic (ICEO) flow in the electric double layer for one half cycle of an AC electric field. Under a horizontal AC electric field with a low frequency (e.g., 0.1–10 kHz), a stronger slip from ICEO around the Au side drives the JP to propel in the direction of the polystyrene (PS) side. Adapted with permission.[158] Copyright 2008 American Physical Society. (**b**) Self-dielectrophoresis of a JP. Under a vertical electric field at a high frequency (i.e., > 100 kHz), the JP travels with its Au side facing forward due to strong induced field gradients between the Au hemisphere and the conducting substrate (bottom, right inset). Adapted with permission.[188] Copyright 2016 American Chemical Society. (**c-d**) Asymmetric surface electrohydrodynamic (EHD) flows for particle self-propulsion. (**c**) An asymmetric PS dimer self-propels by asymmetric EHD flows in a vertical electric field, in this case, at frequencies between 1.4 and 6.0 kHz. The top schematic illustrates a dumbbell model where two spheres, A and B, are connected by an imaginary rod. The dimer moves toward the B end since the B particle generates stronger attractive EHD flows. Adapted with permission.[161] Copyright 2015 American Physical Society. (**d**) Circular motion of a L-shaped particle overlaid with its trajectory (left). A schematic of the template used to assemble the L-shaped particle (right). Adapted with permission.[192] Copyright 2017 Royal Society of Chemistry. (**e-f**) Self-rectified electrophoretic motion. (**e**) A millimeter-sized diode self-propels on a liquid-air interface due to an applied AC electric field. The rectified DC electric field between the electrodes of the diode leads to electroosmotic flows, propelling the diode in the direction of its anode. Adapted with permission.[163] Copyright 2007 Nature Publishing Group. (**f**) Nanosized-diode self-propulsion. A SEM image (left) and a schematic diagram (right) of a Cd/Polypyrrole nanowire diode propelling away from its Cd end. Adapted with permission.[195] Copyright 2010 American Chemical Society.

1.5 Layout of this dissertation

My graduate research was focused on understanding the fundamental principles of dynamic behaviors of anisotropic colloidal particles in external fields that can form the basis of making microbots, microswimmers, and microdevices. This Chapter 1 has served to introduce the background of dynamic colloidal systems and to provide early examples of external field-driven reconfigurable assemblies and self-propelling (or active) particles. Chapter 2 discusses how magnetically responsive patchy microcubes can be assembled into self-reconfiguring microclusters. We demonstrate that these self-reconfiguring clusters can be served as microbots based on their sequence-encoded reconfiguration function. Chapter 3 presents how to make the magnetically self-reconfiguring microcube assemblies self-propel. We assembled single-hinged microscallop structures in non-Newtonian fluids and applied cyclic time-asymmetric magnetic fields for their directional swimming motions. Chapter 4 investigates active rotation of engineered anisotropic particles in AC electric fields. Particles with engineered anisotropy in shape and polarizabilities transduced external electrical energy into directed rotational motions. We demonstrate how to electrokinetically tune their dynamic responses using the AC field parameters, including field frequency and strength. Chapter 6, the final chapter of this dissertation, summarizes my graduate research and provides future directions for stimuli-responsive functional materials and active particles.

1.6 References

[1] D. H. Everett. *Basic Principles of Colloid Science*; The Royal Society of Chemistry: London, 1988.

[2] L. S. Hirst. *Fundamentals of Soft Matter Science*; CRC Press: Boca Raton, 2012.

[3] J. Israelachvili, P. Mcguiggan. Forces between Surfaces in Liquids. *Science* **1988**, *241*, 795.

[4] J. Israelachvili, H. Wennerström. Role of Hydration and Water Structure in Biological and Colloidal Interactions. *Nature* **1996**, *379*, 219.

[5] Y. Min, M. Akbulut, K. Kristiansen, Y. Golan, J. Israelachvili. The Role of Interparticle and External Forces in Nanoparticle Assembly. *Nat. Mater.* **2008**, *7*, 527.

[6] K. J. M. Bishop, C. E. Wilmer, S. Soh, B. A. Grzybowski. Nanoscale Forces and Their Uses in Self-Assembly. *Small* **2009**, *5*, 1600.

[7] P. Walstra. Colloidal Interactions. *Phys. Chem. Foods* **2003**, *12*, 455.

[8] A. Yethiraj. Tunable Colloids: Control of Colloidal Phase Transitions with Tunable Interactions. *Soft Matter* **2007**, *3*, 1099.

[9] M. Oettel, S. Dietrich. Colloidal Interactions at Fluid Interfaces. *Langmuir* **2008**, *24*, 1425.

[10] N. D. Denkov, O. D. Velev, P. A. Kralchevsky, I. B. Ivanov, H. Yoshimura, K. Nagayama. Mechanism of Formation of Two-Dimensional Crystals from Latex Particles on Substrates. *Langmuir* **1992**, *8*, 3183.

[11] N. D. Denkov, O. D. Velev, P. A. Kralchevsky, I. B. Ivanov, H. Yoshimura, K. Nagayama. Two-Dimensional Crystallization. *Nature* **1993**, *361*, 26.

[12] P. A. Kralchevsky, N. D. Denkov. Capillary Forces and Structuring in Layers of Colloid Particles. *Curr. Opin. Colloid Interface Sci.* **2001**, *6*, 383.

[13] A. D. Dinsmore, J. C. Crocker, A. G. Yodh. Self-Assembly of Colloidal Crystals. *Curr. Opin. Colloid Interface Sci.* **1998**, *3*, 5.

[14] O. D. Velev. Self-Assembly of Unusual Nanoparticle Crystals. *Science* **2006**, *312*, 376.

[15] O. D. Velev, A. M. Lenhoff, E. W. Kaler. A Class of Microstructured Particles Through Colloidal Crystallization. *Science* **2000**, *287*, 2240.

[16] O. D. Velev, E. W. Kaler. Structured Porous Materials via Colloidal Crystal Templating: From Inorganic Oxides to Metals. *Adv. Mater.* **2000**, *12*, 531.

[17] T. Tørring, N. V. Voigt, J. Nangreave, H. Yan, K. V. Gothelf. DNA Origami: A Quantum Leap for Self-Assembly of Complex Structures. *Chem. Soc. Rev.* **2011**, *40*, 5636.

[18] Y. Mai, A. Eisenberg. Self-Assembly of Block Copolymers. *Chem. Soc. Rev.* **2012**, *41*, 5969.

[19] Y. Gao, J. Shi, D. Yuan, B. Xu. Imaging Enzyme-Triggered Self-Assembly of Small Molecules inside Live Cells. *Nat. Commun.* **2012**, *3*, 1033.

[20] J. C. Huie. Guided Molecular Self-Assembly: A Review of Recent Efforts. *Smart Mater. Struct.* **2003**, *12*, 264.

[21] J.-M. Lehn. Toward Self-Organization and Complex Matter. *Science* **2002**, *295*, 2400.

[22] R. Chakrabarty, P. S. Mukherjee, P. J. Stang. Supramolecular Coordination: Self-Assembly of Finite Two- and Three-Dimensional Ensembles. *Chem. Rev.* **2011**, *111*, 6810.

[23] Z. Nie, A. Petukhova, E. Kumacheva. Properties and Emerging Applications of Self-Assembled Structures Made from Inorganic Nanoparticles. *Nat. Nanotechnol.* **2010**, *5*, 15.

[24] N. Vogel, M. Retsch, C. A. Fustin, A. Del Campo, U. Jonas. Advances in Colloidal Assembly: The Design of Structure and Hierarchy in Two and Three Dimensions. *Chem. Rev.* **2015**, *115*, 6265.

[25] K. R. Phillips, G. T. England, S. Sunny, E. Shirman, T. Shirman, N. Vogel, J. Aizenberg. A Colloidoscope of Colloid-Based Porous Materials and Their Uses. *Chem. Soc. Rev.* **2016**, *45*, 281.

[26] Y. Zhao, L. Shang, Y. Cheng, Z. Gu. Spherical Colloidal Photonic Crystals. *Acc. Chem. Res.* **2014**, *47*, 3632.

[27] J. Hou, M. Li, Y. Song. Patterned Colloidal Photonic Crystals. *Angew. Chemie - Int. Ed.* **2018**, *57*, 2544.

[28] I. Moriguchi, Y. Shono, H. Yamada, T. Kudo. Colloidal Crystal-Derived Nanoporous Electrode Materials of Cut SWNTs-Assembly and TiO2/SWNTs Nanocomposite. *J. Phys. Chem. B* **2008**, *112*, 14560.

[29] Y. Fang, Y. Ni, S.-Y. Leo, C. Taylor, V. Basile, P. Jiang. Reconfigurable Photonic Crystals Enabled by Pressure-Responsive Shape-Memory Polymers. *Nat. Commun.* **2015**, *6*, 7416.

[30] J. S. Sander, R. M. Erb, L. Li, A. Gurijala, Y. M. Chiang. High-Performance Battery Electrodes via Magnetic Templating. *Nat. Energy* **2016**, *1*, 1.

[31] S. C. Glotzer, M. J. Solomon. Anisotropy of Building Blocks and Their Assembly into Complex Structures. *Nat. Mater.* **2007**, *6*, 557.

[32] J. M. Chem, G. Loget, A. Kuhn. Bulk Synthesis of Janus Objects and Asymmetric Patchy Particles. *J. Mater. Chem.* **2012**, *22*, 15457.

[33] A. Walther, A. H. E. Müller. Janus Particles: Synthesis, Self-Assembly, Physical Properties, and Applications. *Chem. Rev.* **2013**, *113*, 5194.

[34] B. G. Prevo, O. D. Velev. Controlled , Rapid Deposition of Structured Coatings from Micro- and Nanoparticle Suspensions. *Langmuir* **2004**, *20*, 2099.

[35] A. Perro, S. Reculusa, S. Ravaine, E. Bourgeat-Lami, E. Duguet. Design and Synthesis of Janus Micro- and Nanoparticles. *J. Mater. Chem.* **2005**, *15*, 3745.

[36] A. B. Pawar, I. Kretzschmar. Patchy Particles by Glancing Angle Deposition. *Langmuir* **2008**, *24*, 355.

[37] M. M. Hawkeye, M. J. Brett. Glancing Angle Deposition: Fabrication, Properties, and Applications of Micro- and Nanostructured Thin Films. *J. Vac. Sci. Technol. A Vacuum, Surfaces, Film.* **2007**, *25*, 1317.

[38] A. J. Swiston, C. Cheng, S. H. Um, D. J. Irvine, R. E. Cohen, M. F. Rubner. Surface Functionalization of Living Cells with Multilayer Patches. *Nano Lett.* **2008**, *8*, 4446.

[39] E. Briand, V. Humblot, J. Landoulsi, S. Petronis, C. Pradier, B. Kasemo, S. Svedhem. Chemical Modifications of Au/SiO 2 Template Substrates for Patterned Biofunctional

Surfaces. *Langmuir* **2011**, *27*, 678.

[40] K. E. Peyer, S. Tottori, F. Qiu, L. Zhang, B. J. Nelson. Magnetic Helical Micromachines. *Chem. Eur. J.* **2013**, *19*, 28.

[41] A. G. Mark, J. G. Gibbs, T. Lee, P. Fischer. Hybrid Nanocolloids with Programmed Three-Dimensional Shape and Material Composition. *Nat. Mater.* **2013**, *12*, 802.

[42] D. Schamel, M. Pfeifer, J. G. Gibbs, B. Miksch, A. G. Mark, P. Fischer. Chiral Colloidal Molecules And Observation of The Propeller Effect. *J. Am. Chem. Soc.* **2013**, *135*, 12353.

[43] O. G. Schmidt, K. Eberl. Thin Solid Films Roll up into Nanotubes. *Nature* **2001**, *410*, 168.

[44] D. J. Bell, S. Leutenegger, K. M. Hammar, L. X. Dong, B. J. Nelson. Flagella-like Propulsion for Microrobots Using a Nanocoil and a Rotating Electromagnetic Field. *Proc. IEEE Int. Conf. Rob. Autom.* **2007**, 1128.

[45] S. Tottori, L. Zhang, F. Qiu, K. K. Krawczyk, A. Franco-Obregón, B. J. Nelson. Magnetic Helical Micromachines: Fabrication, Controlled Swimming, and Cargo Transport. *Adv. Mater.* **2012**, *24*, 811.

[46] C. N. Lafratta, J. T. Fourkas, T. Baldacchini, R. A. Farrer. Multiphoton Fabrication. *Angew. Chem. Int. Ed.* **2007**, *46*, 6238.

[47] B. R. Martin, D. J. Dermody, B. D. Reiss, M. Fang, L. A. Lyon, M. J. Natan, T. E. Mallouk. Orthogonal Self-Assembly on Colloidal Gold-Platinum Nanorods. *Adv. Mater.* **1999**, *11*, 1021.

[48] M. J. Banholzer, L. Qin, J. E. Millstone, K. D. Osberg, C. A. Mirkin. On-Wire Lithography: Synthesis , Encoding and Biological Applications. *Nat. Protoc.* **2009**, *4*, 838.

[49] Y. Xia, G. M. Whitesides. Soft Lithography. *Annu. Rev. Mater. Sci.* **1998**, *28*, 153.

[50] W. F. Paxton, K. C. Kistler, C. C. Olmeda, A. Sen, S. K. St Angelo, Y. Cao, T. E. Mallouk, P. E. Lammert, V. H. Crespi. Catalytic Nanomotors: Autonomous Movement of Striped Nanorods. *J. Am. Chem. Soc.* **2004**, *126*, 13424.

[51] H. Masuda, K. Fukuda. Ordered Metal Nanohole Arrays Made by a Two-Step Replication of Honeycomb Structures of Anodic Alumina. *Science* **1995**, *268*, 1466.

[52] S. Kang, A. Kumar, C. Choi, K. E. Tettey, C. Lee, D. Lee, B. J. Park. Triblock Cylinders at Fluid−Fluid Interfaces. *Langmuir* **2014**, *30*, 13199.

[53] J. P. Rolland, B. W. Maynor, L. E. Euliss, A. E. Exner, G. M. Denison, J. M. DeSimone. Direct Fabrication and Harvesting of Monodisperse, Shape-Specific Nanobiomaterials. *J. Am. Chem. Soc.* **2005**, *127*, 10096.

[54] C. W. Shields IV, S. Zhu, Y. Yang, B. Bharti, J. Liu, B. B. Yellen, O. D. Velev, G. P. López. Field-Directed Assembly of Patchy Anisotropic Microparticles with Defined Shape. *Soft Matter* **2013**, *9*, 9219.

[55] Z. Nie, W. Li, M. Seo, S. Xu, E. Kumacheva. Janus and Ternary Particles Generated by Microfluidic Synthesis: Design, Synthesis, and Self-Assembly. *J. Am. Chem. Soc.* **2006**, *128*, 9408.

[56] D. Dendukuri, D. C. Pregibon, J. Collins, T. A. Hatton, P. S. Doyle. Continuous-Flow Lithography for High-Throughputmicroparticle Synthesis. *Nat. Mater.* **2006**, *5*, 365.

[57] T. S. Shim, S. Yang, S. Kim. Dynamic Designing of Microstructures by Chemical Gradient-Mediated Growth. *Nat. Commun.* **2015**, *6*, 6584.

[58] A. M. Yake, R. A. Panella, C. E. Snyder, D. Velegol. Fabrication of Colloidal Doublets by a Salting Out - Quenching - Fusing Technique. *Langmuir* **2006**, *22*, 9135.

[59] S. Ni, J. Leemann, I. Buttinoni, L. Isa, H. Wolf. Programmable Colloidal Molecules from Sequential Capillarity-Assisted Particle Assembly. *Sci. Adv.* **2016**, *2*, e1501779.

[60] J. A. Champion, Y. K. Katare, S. Mitragotri. Making Polymeric Micro- and Nanoparticles of Complex Shapes. *Proc. Natl. Acad. Sci.* **2007**, *104*, 11901.

[61] J. W. Kim, R. J. Larsen, D. A. Weitz. Uniform Nonspherical Colloidal Particles with Tunable Shapes. *Adv. Mater.* **2007**, *19*, 2005.

[62] S.-H. Kim, A. D. Hollingsworth, S. Sacanna, S.-J. Chang, G. Lee, D. J. Pine, G.-R. Yi. Synthesis and Assembly of Colloidal Particles with Sticky Dimples. *J. Am. Chem. Soc.* **2012**, *134*, 16115.

[63] S. Sacanna, M. Korpics, K. Rodriguez, L. Colón-Meléndez, S.-H. Kim, D. J. Pine, G.-R. Yi. Shaping Colloids for Self-Assembly. *Nat. Commun.* **2013**, *4*, 1688.

[64] J. Ge, Y. Hu, T. Zhang, Y. Yin. Superparamagnetic Composite Colloids with Anisotropic Structures. *J. Am. Chem. Soc.* **2007**, *129*, 8974.

[65] S. Sacanna, L. Rossi, D. J. Pine. Magnetic Click Colloidal Assembly. *J. Am. Chem. Soc.* **2012**, *134*, 6112.

[66] G. M. Whitesides, M. Boncheva. Beyond Molecules: Self-Assembly of Mesoscopic and Macroscopic Components. *Proc. Natl. Acad. Sci. U. S. A.* **2002**, *99*, 4769.

[67] F. Bai, D. Wang, Z. Huo, W. Chen, L. Liu, X. Liang, C. Chen, X. Wang, Q. Peng, Y. Li. A Versatile Bottom-up Assembly Approach to Colloidal Spheres from Nanocrystals. *Angew. Chemie - Int. Ed.* **2007**, *46*, 6650.

[68] M. H. Lash, M. V Fedorchak, J. J. McCarthy, S. R. Little. Scaling up Self-Assembly: Bottom-up Approaches to Macroscopic Particle Organization. *Soft Matter* **2015**, *11*, 5597.

[69] G. M. Whitesides, B. Grzybowski. Self-Assembly at All Scales. *Science* **2002**, *295*, 2418.

[70] M. Boncheva, G. M. Whitesides. Making Things by Self-Assembly. *MRS Bull.* **2005**, *30*, 736.

[71] S. C. Glotzer, M. J. Solomon, N. A. Kotov. Self-Assembly: From Nanoscale to Microscale Colloids. *AIChE J.* **2004**, *50*, 2978.

[72] B. A. Grzybowski, C. E. Wilmer, J. Kim, K. P. Browne, K. J. M. Bishop. Self-Assembly: From Crystals to Cells. *Soft Matter* **2009**, *5*, 1110.

[73] G. M. Whitesides, J. P. Mathias, C. T. Seto. Molecular Self-Assembly and Nanochemistry: A Chemical Strategy for the Synthesis of Nanostructures. *Science* **1991**, *254*, 1312.

[74] E. Winfree, F. Liu, L. A. Wenzler, N. C. Seeman. Design and Self-Assembly of Two-Dimensional DNA Crystals. *Nature* **1998**, *394*, 539.

[75] S. Zhang, D. M. Marini, W. Hwang, S. Santoso. Design of Nanostructured Biological Materials through Self-Assembly of Peptides and Proteins. *Curr. Opin. Chem. Biol.* **2002**, *6*, 865.

[76] M. Grzelczak, J. Vermant, E. M. Furst, L. M. Liz-marza. Directed Self-Assembly of Nanoparticles. *ACS Nano* **2010**, *4*, 3591.

[77] O. D. Velev, S. Gupta. Materials Fabricated by Micro- and Nanoparticle Assembly - The Challenging Path from Science to Engineering. *Adv. Mater.* **2009**, *21*, 1897.

[78] G. A. Ozin, K. Hou, B. V. Lotsch, L. Cademartiri, D. P. Puzzo, F. Scotognella, A. Ghadimi, J. Thomson. Nanofabrication by Self-Assembly. *Mater. Today* **2009**, *12*, 12.

[79] Y. Wang, Y. Wang, D. R. Breed, V. N. Manoharan, L. Feng, A. D. Hollingsworth, M. Weck, D. J. Pine. Colloids with Valence and Specific Directional Bonding. *Nature* **2012**, *491*, 51.

[80] S. Sacanna, W. T. M. Irvine, P. M. Chaikin, D. J. Pine. Lock and Key Colloids. *Nature* **2010**, *464*, 575.

[81] K. D. Hermanson, S. O. Lumsdon, J. P. Williams, E. W. Kaler, O. D. Velev. Dielectrophoretic Assembly of Electrically Functional Microwires from Nanoparticle Suspensions. *Science* **2001**, *294*, 1082.

[82] O. D. Velev, K. H. Bhatt. On-Chip Micromanipulation and Assembly of Colloidal Particles by Electric Fields. *Soft Matter* **2006**, *2*, 738.

[83] S. Gangwal, A. Pawar, I. Kretzschmar, O. D. Velev. Programmed Assembly of Metallodielectric Patchy Particles in External AC Electric Fields. *Soft Matter* **2010**, *6*, 1413.

[84] B. Ren, A. Ruditskiy, J. H. K. Song, I. Kretzschmar. Assembly Behavior of Iron Oxide-Capped Janus Particles in a Magnetic Field. *Langmuir* **2012**, *28*, 1149.

[85] J. Yan, M. Bloom, S. C. Bae, E. Luijten, S. Granick. Linking Synchronization to Self-Assembly Using Magnetic Janus Colloids. *Nature* **2012**, *491*, 578.

[86] J. Yan, K. Chaudhary, S. Chul Bae, J. A. Lewis, S. Granick. Colloidal Ribbons and Rings from Janus Magnetic Rods. *Nat. Commun.* **2013**, *4*, 1516.

[87] T. B. Jones. *Electromechanics of Particles*; Cambridge University Press: New York, 1995.

[88] O. D. Velev, K. H. Bhatt. On-Chip Micromanipulation and Assembly of Colloidal Particles by Electric Fields. *Soft Matter* **2006**, *2*, 738.

[89] S. Sacanna, D. J. Pine, G.-R. Yi. Engineering Shape: The Novel Geometries of Colloidal Self-Assembly. *Soft Matter* **2013**, *9*, 8096.

[90] J. Zhang, E. Luijten, S. Granick. Toward Design Rules of Directional Janus Colloidal Assembly. *Annu. Rev. Phys. Chem.* **2015**, *66*, 581.

[91] G. van Anders, D. Klotsa, N. K. Ahmed, M. Engel, S. C. Glotzer. Understanding Shape Entropy through Local Dense Packing. *Proc. Natl. Acad. Sci.* **2014**, *111*, E4812.

[92] Z. Zhang, S. C. Glotzer. Self-Assembly of Patchy Particles. *Nano Lett.* **2004**, *4*, 1407.

[93] P. F. Damasceno, M. Engel, S. C. Glotzer. Predictive Self-Assembly of Polyhedra into Complex Structures. *Science* **2012**, *337*, 453.

[94] K. P. Herlihy, J. Nunes, J. M. DeSimone. Electrically Driven Alignment and Crystallization of Unique Anisotropic Polymer Particles. *Langmuir* **2008**, *24*, 8421.

[95] S. Gangwal, O. J. Cayre, O. D. Velev. Dielectrophoretic Assembly of Metallodielectric Janus Particles in AC Electric Fields. *Langmuir* **2008**, *24*, 13312.

[96] B. Bharti, O. D. Velev. Assembly of Reconfigurable Colloidal Structures by Multidirectional Field-Induced Interactions. *Langmuir* **2015**, *31*, 7987.

[97] M. J. Solomon. Tools and Functions of Reconfigurable Colloidal Assembly. *Langmuir* **2018**, DOI: 10.1021/acs.langmuir.7b03748.

[98] A. B. Pawar, I. Kretzschmar. Fabrication, Assembly, and Application of Patchy Particles. *Macromol. Rapid Commun.* **2010**, *31*, 150.

[99] S. Jiang, Q. Chen, M. Tripathy, E. Luijten, K. S. Schweizer, S. Granick. Janus Particle Synthesis and Assembly. *Adv. Mater.* **2010**, *22*, 1060.

[100] Q. Chen, J. K. Whitmer, S. Jiang, S. C. Bae, E. Luijten, S. Granick. Supracolloidal Reaction Kinetics of Janus Spheres. *Science* **2011**, *331*, 199.

[101] Q. Chen, J. Yan, J. Zhang, S. C. Bae, S. Granick. Janus and Multiblock Colloidal Particles. *Langmuir* **2012**, *28*, 13555.

[102] S. K. Smoukov, S. Gangwal, M. Marquez, O. D. Velev. Reconfigurable Responsive Structures Assembled from Magnetic Janus Particles. *Soft Matter* **2009**, *5*, 1285.

[103] P. Tierno, R. Muruganathan, T. M. Fischer. Viscoelasticity of Dynamically Self-Assembled Paramagnetic Colloidal Clusters. *Phys. Rev. Lett.* **2007**, *98*, 1.

[104] F. Martinez-Pedrero, P. Tierno. Magnetic Propulsion of Self-Assembled Colloidal Carpets : Efficient Cargo Transport via a Conveyor-Belt Effect. *Phys. Rev. Appl.* **2015**, *3*, 51003.

[105] J. Yan, S. C. Bae, S. Granick. Colloidal Superstructures Programmed into Magnetic Janus Particles. *Adv. Mater.* **2015**, *27*, 874.

[106] J. Byrom, P. Han, M. Savory, S. L. Biswal. Directing Assembly of DNA-Coated Colloids with Magnetic Fields To Generate Rigid, Semiflexible, and Flexible Chains. *Langmuir* **2014**, *30*, 9045.

[107] S. Kuei, B. Garza, S. L. Biswal. From Strings to Coils: Rotational Dynamics of DNA-Linked Colloidal Chains. *Phys. Rev. Fluids* **2017**, *2*, 1.

[108] B. Bharti, A.-L. Fameau, M. Rubinstein, O. D. Velev. Nanocapillarity-Mediated Magnetic Assembly of Nanoparticles into Ultraflexible Filaments and Reconfigurable Networks. *Nat. Mater.* **2015**, *14*, 1104.

[109] B. Bharti, A.-L. Fameau, O. D. Velev. Magnetophoretic Assembly of Flexible Nanoparticles/lipid Microfilaments. *Faraday Discuss.* **2015**, *181*, 437.

[110] K. Chaudhary, J. J. Juárez, Q. Chen, S. Granick, J. a Lewis. Reconfigurable Assemblies of Janus Rods in AC Electric Fields. *Soft Matter* **2014**, *10*, 1320.

[111] F. Ma, S. Wang, L. Smith, N. Wu. Two-Dimensional Assembly of Symmetric Colloidal Dimers under Electric Fields. *Adv. Funct. Mater.* **2012**, *22*, 4334.

[112] M. Trau, D. A. Saville, I. A. Aksay. Field-Induced Layering of Colloidal Crystals. *Science* **1996**, *272*, 706.

[113] S. R. Yeh, M. Seul, B. I. Shraiman. Assembly of Ordered Colloidal Aggregates by Electric-Field-Induced Fluid Flow. *Nature* **1997**, *386*, 57.

[114] W. D. Ristenpart, I. A. Aksay, D. A. Saville. Assembly of Colloidal Aggregates by Electrohydrodynamic Flow: Kinetic Experiments and Scaling Analysis. *Phys. Rev. E* **2004**,

69, 21405.

[115] T. J. Woehl, K. L. Heatley, C. S. Dutcher, N. H. Talken, W. D. Ristenpart. Electrolyte-Dependent Aggregation of Colloidal Particles near Electrodes in Oscillatory Electric Fields. *Langmuir* **2014**, *30*, 4887.

[116] F. Ma, S. Wang, H. Zhao, D. T. Wu, N. Wu. Colloidal Structures of Asymmetric Dimers via Orientation-Dependent Interactions. *Soft Matter* **2014**, *10*, 8349.

[117] F. Ma, S. Wang, D. T. Wu, N. Wu. Electric-Field–induced Assembly and Propulsion of Chiral Colloidal Clusters. *Proc. Natl. Acad. Sci.* **2015**, *112*, 6307.

[118] A. Ruditskiy, B. Ren, I. Kretzschmar. Behaviour of Iron Oxide (Fe_3O_4) Janus Particles in Overlapping External AC Electric and Static Magnetic Fields. *Soft Matter* **2013**, *9*, 9174.

[119] B. Ren, I. Kretzschmar. Viscosity-Dependent Janus Particle Chain Dynamics. *Langmuir* **2013**, *29*, 14779.

[120] A. A. Shah, B. Schultz, W. Zhang, S. C. Glotzer, M. J. Solomon. Actuation of Shape-Memory Colloidal Fibres of Janus Ellipsoids. *Nat. Mater.* **2014**, *14*, 117.

[121] C. W. Shields IV, S. Zhu, Y. Yang, B. Bharti, J. Liu, B. B. Yellen, O. D. Velev, G. P. López. Field-Directed Assembly of Patchy Anisotropic Microparticles with Defined Shape. *Soft Matter* **2013**, 9219.

[122] R. C. Jaeger. *Introduction to Microelectronic Fabrication*, 2nd ed.; Prentice Hall, 2002.

[123] J. C. M. Wan, C. Massie, J. Garcia-corbacho, F. Mouliere, J. D. Brenton, C. Caldas, S. Pacey, R. Baird, N. Rosenfeld. Liquid Biopsies Come of Age: Towards Implementation of Circulating Tumour DNA. *Nat. Rev. Cancer* **2017**, *17*, 223.

[124] N. Pamme, A. Manz. On-Chip Free-Flow Magnetophoresis: Continuous Flow Separation of Magnetic Particles and Agglomerates. *Anal. Chem.* **2004**, *76*, 7250.

[125] J. M. Karlinsey. Sample Introduction Techniques for Microchip Electrophoresis: A Review. *Anal. Chim. Acta* **2012**, *725*, 1.

[126] R. Pethig. Review Article–Dielectrophoresis: Status of the Theory, Technology, and Applications. *Biomicrofluidics* **2010**, *4*, 022811.

[127] T. Laurell, F. Petersson, A. Nilsson, F. Petersson. Chip Integrated Strategies for Acoustic Separation and Manipulation of Cells and Particles Resulted in Several National. *Chem. Soc. Rev.* **2007**, *36*, 492.

[128] F. Zheng. Thermophoresis of Spherical and Non-Spherical Particles : A Review of Theories and Experiments. *Adv. Colloid Interface Sci.* **2002**, *97*, 255.

[129] S. Sánchez, L. Soler, J. Katuri. Chemically Powered Micro- and Nanomotors Angewandte. *Angew. Chem. Int. Ed.* **2015**, *54*, 1414.

[130] W. Wang, W. Duan, S. Ahmed, T. E. Mallouk, A. Sen. Small Power: Autonomous Nano- and Micromotors Propelled by Self-Generated Gradients. *Nano Today* **2013**, *8*, 531.

[131] W. Wang, T. Chiang, D. Velegol, T. E. Mallouk. Understanding the Efficiency of Autonomous Nano- and Microscale Motors. *J. Am. Chem. Soc.* **2013**, *135*, 10557.

[132] H. Wang, G. Zhao, M. Pumera. Beyond Platinum: Bubble-Propelled Micromotors Based on Ag and MnO2 Catalysts. *J. Am. Chem. Soc.* **2014**, *136*, 2719.

[133] W. Gao, A. Pei, J. Wang. Water-Driven Micromotors. *ACS Nano* **2012**, *6*, 8432.

[134] W. F. Paxton, A. Sen, T. E. Mallouk. Motility of Catalytic Nanoparticles through Self-Generated Forces. *Chem. Eur. J.* **2005**, *11*, 6462.

[135] K. J. Rao, F. Li, L. Meng, H. Zheng, F. Cai, W. Wang. A Force to Be Reckoned With: A Review of Synthetic Microswimmers Powered by Ultrasound. *Small* **2015**, No. 24, 2836.

[136] W. Wang, L. A. Castro, M. Hoyos, T. E. Mallouk. Autonomous Motion of Metallic Microrods Propelled by Ultrasound. *ACS Nano* **2012**, *6*, 6122.

[137] D. Ahmed, M. Lu, A. Nourhani, P. E. Lammert, Z. Stratton, H. S. Muddana, V. H. Crespi, T. J. Huang. Selectively Manipulable Acoustic-Powered Microswimmers Daniel. *Sci. Rep.* **2015**, *5*, 9744.

[138] M. Kaynak, A. Ozcelik, A. Nourhani, P. E. Lammert, V. H. Crespi, T. J. Huang. Acoustic Actuation of Bioinspired Microswimmers. *Lab Chip* **2017**, *17*, 395.

[139] D. Kagan, M. J. Benchimol, J. C. Claussen, E. Chuluun-erdene, S. Esener, J. Wang. Acoustic Droplet Vaporization and Propulsion of Perfluorocarbon-Loaded Microbullets for Targeted Tissue Penetration and Deformation. *Angew. Chem. Int. Ed.* **2012**, *51*, 7519.

[140] A. Zöttl, H. Stark. Emergent Behavior in Active Colloids. *J. Phys. Condens. Matter* **2016**, *28*, 253001.

[141] H.-R. Jiang, N. Yoshinaga, M. Sano. Active Motion of a Janus Particle by Self-Thermophoresis in a Defocused Laser Beam. *Phys. Rev. Lett.* **2010**, *105*, 268302.

[142] C. Maggi, F. Saglimbeni, M. Dipalo, F. De Angelis, R. Di Leonardo. Micromotors with Asymmetric Shape That Efficiently Convert Light into Work by Thermocapillary Effects. *Nat. Commun.* **2015**, *6*, 7855.

[143] I. Buttinoni, G. Volpe, F. Kümmel, G. Volpe, C. Bechinger. Active Brownian Motion Tunable by Light. *J. Phys. Condens. Matter* **2012**, *24*, 284129.

[144] B. Hagen, R. Wittkowski, I. Buttinoni, R. Eichhorn, G. Volpe. Circular Motion of Asymmetric Self-Propelling Particles. *Phys. Rev. Lett.* **2013**, *110*, 198302.

[145] B. Dai, J. Wang, Z. Xiong, X. Zhan, W. Dai, C. Li, S. Feng, J. Tang. Programmable Artificial Phototactic Microswimmer. *Nat. Nanotechnol.* **2016**, *11*, 1087.

[146] F. Ku, C. Bechinger, T. Speck, H. Lo. Dynamical Clustering and Phase Separation in Suspensions of Self-Propelled Colloidal Particles. *Phys. Rev. Lett.* **2013**, *110*, 238301.

[147] R. M. Erb, J. J. Martin, R. Soheilian, C. Pan, J. R. Barber. Actuating Soft Matter with Magnetic Torque. *Adv. Funct. Mater.* **2016**, *26*, 3859.

[148] R. S. M. Rikken, R. J. M. Nolte, J. C. Maan, J. C. M. van Hest, D. A. Wilson, P. C. M. Christianen. Manipulation of Micro- and Nanostructure Motion with Magnetic Fields. *Soft Matter* **2014**, *10*, 1295.

[149] B. J. Nelson, I. K. Kaliakatsos, J. J. Abbott. Microrobots for Minimally Invasive Medicine. *Annu. Rev. Biomed. Eng.* **2010**, *12*, 55.

[150] E. Lauga, T. R. Powers. The Hydrodynamics of Swimming Microorganisms. *Reports Prog. Phys.* **2009**, *72*, 96601.

[151] K. E. Peyer, L. Zhang, B. J. Nelson. Bio-Inspired Magnetic Swimming Microrobots for

Biomedical Applications. *Nanoscale* **2013**, *5*, 1259.

[152] L. Zhang, T. Petit, Y. Lu, B. E. Kratochvil, K. E. Peyer, R. Pei, J. Lou, B. J. Nelson. Controlled Propulsion and Cargo Transport of Rotating Nickel Nanowires near a Patterned Solid Surface. *ACS Nano* **2010**, *4*, 6228.

[153] P. Tierno, R. Golestanian, I. Pagonabarraga, F. Sagués. Magnetically Actuated Colloidal Microswimmers. *J. Phys. Chem. B* **2008**, *112*, 16525.

[154] G. Loget, A. Kuhn. Propulsion of Microobjects by Dynamic Bipolar Self-Regeneration. *J. Am. Chem. Soc.* **2010**, *132*, 15918.

[155] G. Loget, A. Kuhn. Electric Field-Induced Chemical Locomotion of Conducting Objects. *Nat. Commun.* **2011**, *2*, 535.

[156] Y. Dou, C. A. Cartier, W. Fei, S. Pandey, S. Razavi, I. Kretzschmar, K. J. M. Bishop. Directed Motion of Metallodielectric Particles by Contact Charge Electrophoresis. *Langmuir* **2016**, *32*, 13167.

[157] T. M. Squires, M. Z. Bazant. Breaking Symmetries in Induced-Charge Electro-Osmosis and Electrophoresis. *J. Fluid Mech.* **2006**, *560*, 65.

[158] S. Gangwal, O. Cayre, M. Z. Bazant, O. D. Velev. Induced-Charge Electrophoresis of Metallodielectric Particles. *Phys. Rev. Lett.* **2008**, *100*, 58302.

[159] M. Z. Bazant, T. M. Squires. Induced-Charge Electrokinetic Phenomena: Theory and Microfluidic Applications. *Phys. Rev. Lett.* **2004**, *92*, 66101.

[160] W. D. Ristenpart, I. A. Aksay, D. A. Saville. Electrohydrodynamic Flow around a Colloidal Particle near an Electrode with an Oscillating Potential. *J. Fluid Mech.* **2007**, *575*, 83.

[161] F. Ma, X. Yang, H. Zhao, N. Wu. Inducing Propulsion of Colloidal Dimers by Breaking the Symmetry in Electrohydrodynamic Flow. *Phys. Rev. Lett.* **2015**, *115*, 208302.

[162] X. Yang, N. Wu. Change the Collective Behaviors of Colloidal Motors by Tuning Electrohydrodynamic Flow at the Sub-Particle Level. *Langmuir* **2017**, *34*, 952

[163] S. T. Chang, V. N. Paunov, D. N. Petsev, O. D. Velev. Remotely Powered Self-Propelling Particles and Micropumps Based on Miniature Diodes. *Nat. Mater.* **2007**, *6*, 235.

[164] L. Zhang, J. J. Abbott, L. Dong, B. E. Kratochvil, D. Bell, B. J. Nelson. Artificial Bacterial Flagella: Fabrication and Magnetic Control. *Appl. Phys. Lett.* **2014**, *94*, 64107.

[165] M. Medina-Sánchez, L. Schwarz, A. K. Meyer, F. Hebenstreit, O. G. Schmidt. Cellular Cargo Delivery: Toward Assisted Fertilization by Sperm- Carrying Micromotors. *Nano Lett.* **2016**, *16*, 555.

[166] A. Ghosh, P. Fischer. Controlled Propulsion of Artificial Magnetic Nanostructured Propellers. *Nano Lett.* **2009**, *9*, 2243.

[167] D. Schamel, A. G. Mark, J. G. Gibbs, C. Miksch, K. I. Morozov, A. M. Leshansky, P. Fischer. Nanopropellers and Their Actuation in Complex Viscoelastic Media. *ACS Nano* **2014**, *8*, 8794.

[168] R. Dreyfus, J. Baudry, M. L. Roper, M. Fermigier, H. A. Stone, J. Bibette. Microscopic Artificial Swimmers. *Nature* **2005**, *437*, 862.

[169] S. Sudo, S. Segawa, T. Honda. Magnetic Swimming Mechanism in a Viscous Liquid. *J.*

Intell. Mater. Syst. Struct. **2006**, *17*, 729.

[170] S. Guo, Q. Pan, M. B. Khamesee. Development of a Novel Type of Microrobot for Biomedical Application. *Microsyst. Technol.* **2008**, *14*, 307.

[171] W. Gao, S. Sattayasamitsathit, K. M. Manesh, D. Weihs, J. Wang. Magnetically Powered Flexible Metal Nanowire Motors. *J. Am. Chem. Soc.* **2010**, *132*, 14403.

[172] T. Mirkovic, M. L. Foo, A. C. Arsenault, S. Fournier-Bidoz, N. S. Zacharia, G. A. Ozin. Hinged Nanorods Made Using a Chemical Approach to Flexible Nanostructures. *Nat. Nanotechnol.* **2007**, *2*, 565.

[173] B. Jang, E. Gutman, N. Stucki, B. F. Seitz, P. D. Wendel-garc, T. Newton, J. Pokki, O. Ergeneman, S. Pane, Y. Or, et al. Undulatory Locomotion of Magnetic Multilink Nanoswimmers. *Nano Lett.* **2015**, *15*, 4829.

[174] T. Li, J. Li, H. Zhang, X. Chang, W. Song, Y. Hu, G. Shao, E. Sandraz, G. Zhang, L. Li, et al. Magnetically Propelled Fish-Like Nanoswimmers. *Small* **2016**, *12*, 6098.

[175] T. Li, J. Li, K. I. Morozov, Z. Wu, T. Xu, I. Rozen, A. M. Leshansky, L. Li, J. Wang. Highly Efficient Freestyle Magnetic Nanoswimmer. *Nano Lett.* **2017**, *17*, 5092.

[176] P. Tierno, R. Golestanian, I. Pagonabarraga, F. Sague. Controlled Swimming in Confined Fluids of Magnetically Actuated Colloidal Rotors. *Phys. Rev. Lett.* **2008**, *101*, 218304.

[177] P. Tierno, O. Güell, F. Sagués, R. Golestanian, I. Pagonabarraga. Controlled Propulsion in Viscous Fluids of Magnetically Actuated Colloidal Doublets. *Phys. Rev. E* **2010**, *81*, 11402.

[178] M. Driscoll, B. Delmotte, M. Youssef, S. Sacanna, A. Donev, P. Chaikin. Unstable Fronts and Motile Structures Formed by Microrollers. *Nat. Phys.* **2017**, *13*, 375.

[179] L. O. Mair, B. A. Evans, A. Nacev, P. Y. Stepanov, R. Hilaman, S. Chowdhury, S. Jafari, W. Wang, B. Shapiro, I. N. Weinberg. Magnetic Microkayaks : Propulsion of Microrods Precessing near a Surface by Kilohertz Frequency. *Nanoscale* **2017**, *9*, 3375.

[180] A. Snezhko, M. Belkin, I. S. Aranson, W. Kwok. Self-Assembled Magnetic Surface Swimmers. *Phys. Rev. Lett.* **2009**, *102*, 118103.

[181] A. Snezhko, I. S. Aranson. Magnetic Manipulation of Self-Assembled Colloidal Asters. *Nat. Mater.* **2011**, *10*, 698.

[182] T. O. Tasci, P. S. Herson, K. B. Neeves, D. W. M. Marr. Surface-Enabled Propulsion and Control of Colloidal Microwheels. *Nat. Commun.* **2016**, *7*, 10225.

[183] T. Yang, T. O. Tasci, K. B. Neeves, N. Wu, D. W. M. Marr. Magnetic Microlassos for Reversible Cargo Capture , Transport , and Release. *Langmuir* **2017**, *33*, 5932.

[184] C. E. Sing, L. Schmid, M. F. Schneider, T. Franke, A. Alexander-Katz. Controlled Surface-Induced Flows from the Motion of Self-Assembled Colloidal Walkers. *Proc. Natl. Acad. Sci.* **2010**, *107*, 535.

[185] W. Gao, S. Sattayasamitsathit, K. M. Manesh, D. Weihs, J. Wang. Magnetically Powered Flexible Metal Nanowire Motors. *J. Am. Chem. Soc.* **2010**, *132*, 14403.

[186] C. Peng, I. Lazo, S. V Shiyanovskii, O. D. Lavrentovich. Induced-Charge Electro-Osmosis around Metal and Janus Spheres in Water : Patterns of Flow and Breaking Symmetries. *Phys. Rev. E* **2014**, *90*, 51002.

[187] O. D. Lavrentovich, I. Lazo, O. P. Pishnyak. Nonlinear Electrophoresis of Dielectric and Metal Spheres in a Nematic Liquid Crystal. *Nature* **2010**, *467*, 947.

[188] A. Boymelgreen, G. Yossifon, T. Miloh. Propulsion of Active Colloids by Self-Induced Field Gradients. *Langmuir* **2016**, *32*, 9540.

[189] N. R. Wood, A. I. Wolsiefer, R. W. Cohn, S. J. Williams. Dielectrophoretic Trapping of Nanoparticles with an Electrokinetic Nanoprobe. *Electrophoresis* **2013**, *34*, 1922.

[190] A. M. Boymelgreen, T. Balli, T. Miloh, G. Yossifon. Active Colloids as Mobile Microelectrodes for Unified Label-Free Selective Cargo Transport. *Nat. Commun.* **2018**, *9*, 760.

[191] J. Yan, M. Han, J. Zhang, C. Xu, E. Luijten, S. Granick. Reconfiguring Active Particles by Electrostatic Imbalance. *Nat. Mater.* **2016**, *15*, 1095.

[192] S. Ni, E. Marini, I. Buttinoni, H. Wolf, L. Isa. Hybrid Colloidal Microswimmers through Sequential Capillary Assembly. *Soft Matter* **2017**, *13*, 4252.

[193] S. T. Chang, E. Beaumont, D. N. Petsev, O. D. Velev. Remotely Powered Distributed Microfluidic Pumps and Mixers Based on Miniature Diodes. *Lab Chip* **2008**, *8*, 117.

[194] R. Sharma, O. D. Velev. Remote Steering of Self-Propelling Microcircuits by Modulated Electric Field. *Adv. Funct. Mater.* **2015**, *25*, 5512.

[195] P. Calvo-marzal, S. Sattayasamitsathit, S. Balasubramanian, J. R. Windmiller, C. Dao, J. Wang. Propulsion of Nanowire Diodes. *Chem. Commun.* **2010**, *46*, 1623.

Chapter 2

Sequence-Encoded Reconfigurable Assemblies in Magnetic Fields*

* Partially based on Han and Velev *et al.*, *Sci. Adv.* **2017**, *3*, e1701108.

2.1 Introduction

There is a growing need to develop miniaturized machines that address critical challenges in science and medicine, such as delivering drugs to remote regions in the body and performing precise microscale surgical operations.[1,2] The primary challenges in realizing such miniaturized devices include remote supply of energy, control over their response, and directional translocation.[2,3] Even though early examples of miniaturized robots made by a "top-down" fabrication have shown promise for in vivo manipulation, their feasible size has been limited to the sub-millimeter scale.[4,5] Miniaturizing robotic devices down to microscale could be effectively managed by a "bottom-up" assembly of micron-size particles.[6,7]

The key requirement in fabricating materials via bottom-up assembly is directing the interactions between the particles.[8,9] One of the most tractable ways to control such dynamic behaviors of the particles is the use of external fields.[10–13] The directional interactions induced in colloidal particles by external fields enabled forming simple responsive materials,[14–24] yet endowing them with more complex functionality has been challenging. One way to overcome this challenge is to assemble colloidal particles with tailored form factors and surface polarizabilities in external fields.[25–29] We have previously shown that anisotropically shaped metallic patchy particles can acquire complex polarization patterns in electric and magnetic fields, leading to multidirectional interactions and to formation of assemblies of unusual structure and symmetry.[30] Here, we describe and analyze the emergent, sequence-specific, self-reconfiguration dynamics in supracolloidal assemblies of cube-shaped particles with one metal-coated facet.

2.2 Materials and methods

2.2.1 Particle Fabrication

One-side coated patchy microcubes, comprised of polymer and thin cobalt (Co) films deposited along one of the six facets, were fabricated using standard photolithography and metal deposition techniques.[30] SU-8 10 photoresist (MicroChem, Corp.) was spin-coated on a 3" single-side polished silicon (Si) wafer (Addison Engineering, Inc.) and exposed to UV light (365 nm, MA/BA6 Mask Aligner, Süss MicroTec AG) through a chrome-patterned photomask (consisting of an array of 10 μm transparent squares with a 20 μm pitch; Photo Sciences, Inc.) to form the microcubes, which were revealed after development of the photoresist (following the procedures by MicroChem). We note that the fabricated microcubes can sometimes display slightly rounded edges due the resolution of chrome-printed photomask or due to the inadequate exposure of UV light through the photomask. The wafer was then mounted inside of an electron beam metal evaporator (Solution E-Beam, CHA Industries, Inc.) to allow for the deposition of 10 nm of Cr followed by 100 nm of Co on the topside of the wafer. The patchy microcubes were then harvested from the wafer by the application of shear forces from a rubber scraper and dispersed in Milli-Q water, containing 0.1 vol.% Tween 20 (Sigma-Aldrich, Corp.).

2.2.2 Experimental Setup

A 30 μL solution of the patchy microcubes was placed into the assembly chamber (**Fig. 2.1**) where a hydrophobic ring secured a 20-30 μm gap between a glass slide and a cover slip. A collinear pair of electromagnets (**1 and 2**) placed on either side of the assembly chamber generated a uniform magnetic field in the range 0.1-10 kA/m and a single electromagnet (**3**) placed on the bottom side of the assembly chamber generated a gradient magnetic field in the range of 1-100 kA/m^2, as

measured by a gauss meter (GM-2, AlphaLab, Inc.). The assembly chamber was housed on the table of an optical microscope (BX-61, Olympus, Co.) to enable the observation of the field-directed assembly and manipulation of patchy microcubes. Videos were taken using a CCD camera (DP-70, Olympus, Co.) at 15 frames/sec. The videos were analyzed in ImageJ (NIH, USA) to measure the interdipolar angle between metallic facets on adjacent particles within an assembly.

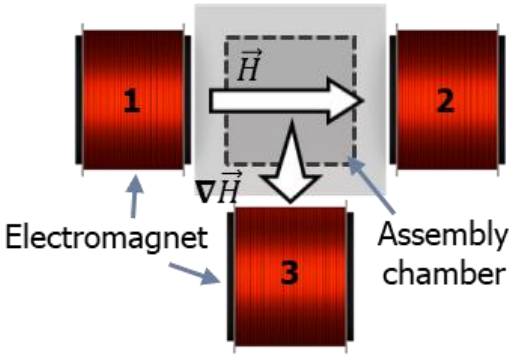

Figure 2.1: Schematic of the experimental setup used to assemble and manipulate the patchy microcubes. A uniform magnetic field was generated by a collinear pair of electromagnets (**1** and **2**) and a magnetic field gradient was imposed by a single electromagnet (**3**).

2.2.3 Numerical Simulation

Magnetostatic calculations were performed using the AC/DC module of COMSOL Multiphysics® modeling software (COMSOL, Inc.) to investigate the local magnetic field distribution around an assembled chain of patchy microcubes under various configurations. The magnetic permeability of the Co coating (1.1676×10^{-1} H/m), the SU-8 polymer (1.257×10^{-6} H/m) and the surrounding water medium (1.257×10^{-6} H/m) were incorporated into the model. The geometry of the system was confined to a two-dimensional area (200 μm × 200 μm) with an extremely fine triangular mesh at the center of the assembly chamber. The simulations were carried out by solving Maxwell's equations with a fully coupled linear solver.

2.3 Results and Discussion

2.3.1 Magnetic Field Driven Assembly of Multi-Cube Clusters

We applied intermittent external magnetic fields to drive the assembly of patchy microcubes of edge length ~10 μm, where one face of the microcube is selectively coated with 100 nm of cobalt (Co) metal. When a uniform magnetic field of 0.1-10 kA/m is generated (e.g., by a collinear pair of electromagnets, as depicted in **Fig. 2.1**) and applied across a chamber containing an aqueous suspension of randomly dispersed microcubes, the magnetic patch on each cube acquires a dipole leading to long-range attraction between the cubes, and chain assembly. The sequence of cubes within an assembled structure is dependent on the initial orientation of the randomly dispersed cubes, as illustrated in **Figure 2.2**. When the external field is applied to randomly dispersed particles, they align with the field in a sequence of so-called *"A"* or *"B"* cube orientation (**Fig. 2.2a→b**), and assemble into a stretched chain configuration while retaining the cube orientation (i.e., *ABBAB*; **Fig. 2.2b→c**).

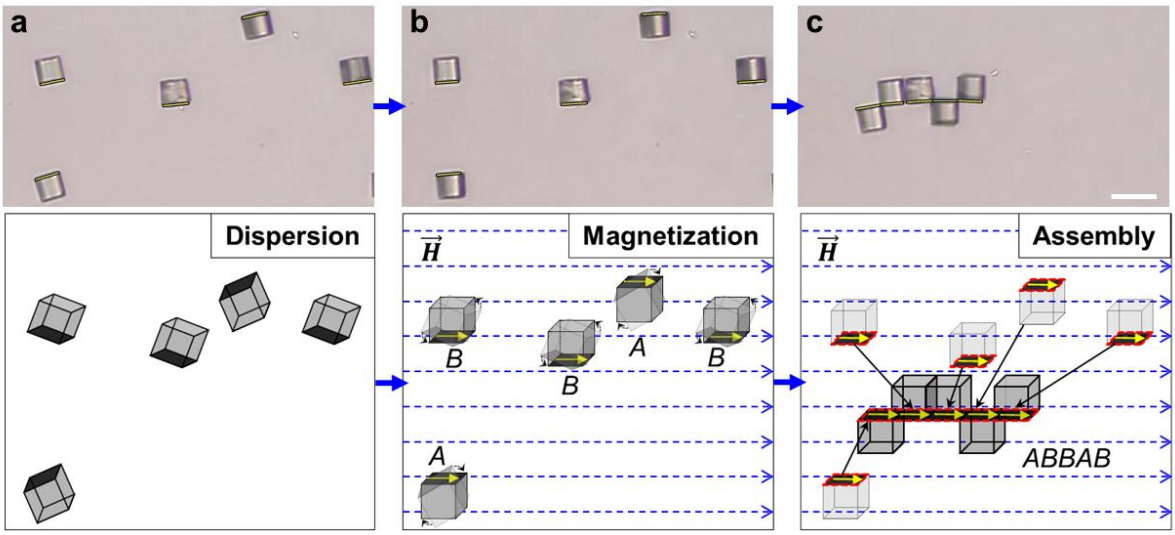

Figure 2.2: Example of the assembly of patchy microcubes under a uniform magnetic field. (**a**) Randomly dispersed microcubes, (**b**) magnetic polarization of the Co patches in the direction of the applied magnetic field ($\vec{H}$), leading to either *A* or *B* cube orientations, and (**c**) formation of multi-cube clusters that retain such *A* or *B* orientations. The superimposed yellow lines in the experimental micrographs denote the location of the magnetic patches. Scale bar = 20 μm.

Figure 2.3 shows an example set of images of an assembled chain of patchy microcubes dried on a glass substrate. Applying a uniform magnetic field to the sample throughout the evaporation process conserved the configuration of the assembled chain. The coloration from an energy dispersive spectroscopy (EDS) recording displayed (**Fig. 2.3c**) on its corresponding scanning electron microscope (SEM) image (**Fig. 2.3b**). The EDS recording in **Figure 2.3c** revealed that the Co patches are connected in series along the center of the assembled chain, confirming the role of the Co patches as a structural director of the chain.

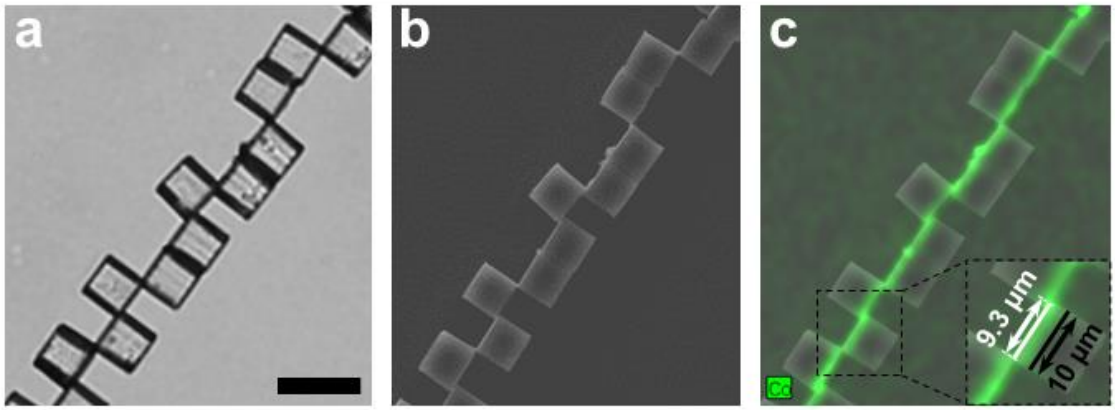

Figure 2.3: (**a**) An image from an optical microscope, (**b**) An image from an SEM and (**c**) An EDS recording overlaid on the image shown in (**b**) (green color indicates the presence of Co) of an assembled chain of patchy cubes. Scale bar = 20 µm.

2.3.2 Magnetic Field Driven Actuation of Multi-Cube Clusters

The ferromagnetic Co patch was selected as a coating material to utilize its residual magnetism (or residual magnetic dipole) retained even after the removal of an external magnetic field (**Fig. 2.4**). The residual magnetic dipole-dipole interaction allowed for the conservation of the overall sequence of patchy cubes within the assembly and the reconfiguration of the assembled structure (**Fig. 2.5**). **Figure 2.4** shows the magnetic hysteresis of a collection of dried microcubes with one face coated with Co, revealing the ferromagnetic nature of the Co patches. Before the

application of the external magnetic field, randomly oriented patchy cubes are not magnetized (**Fig. 2.4a**); however, when an external magnetic field is applied, the Co patches acquire a magnetic dipole (**Fig. 2.4b**), leading to their assembly into multi-cube chains where the Co patches are connected along the center of the chain, as shown in **Figure 2.3c**. Once assembled, even though the magnetic field is removed, the residual magnetization **(M_r)** of the Co patches prevents the chains from disassembling within the experimental timescales investigated (i.e., up to several days; **Fig. 2.4c**). More specifically, when a sufficiently strong magnetic field is applied (e.g., 160 kA/m in **Fig. 2.4b**), the Co patches attain a saturated magnetization state **(M_s; Fig. 2.4b).** They retain a saturated residual magnetization state when the field is removed **(M_{rs}; Fig. 2.4c)**. However, our experimental range of 2-8 kA/m results in an unsaturated residual magnetization. We normalized the degree of residual magnetization as the relative residual magnetization and found that it was linearly dependent on the strength of initially applied magnetic field **(M_r/M_{rs}, where M_r is the residual magnetism**; **Fig. 2.4d).**

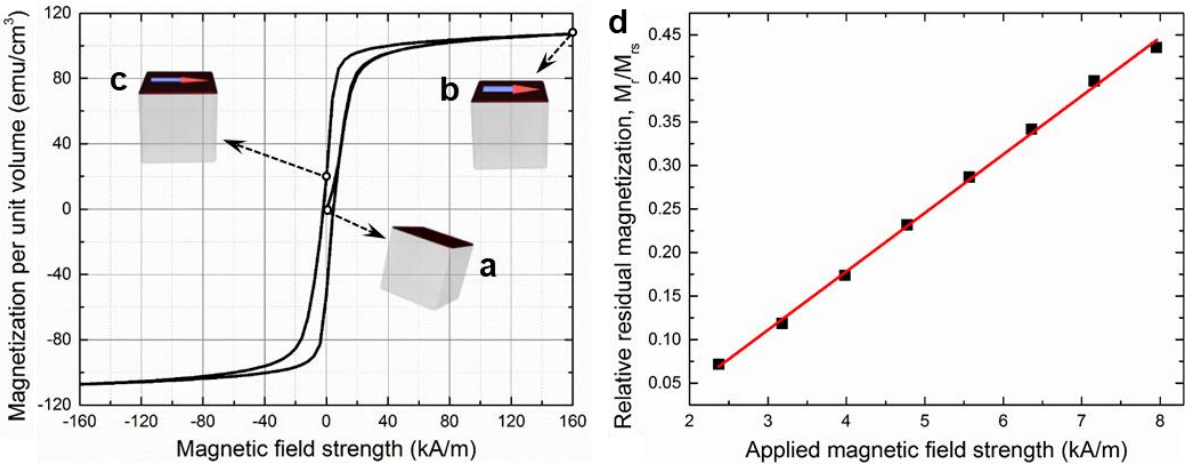

Figure 2.4: Magnetic hysteresis curve of a collection of dried Co-coated patchy microcubes. Measurements and schematics illustrate: (**a**) The initial state of randomly dispersed microcubes, (**b**) The saturated magnetization state of the microcubes, (**c**) The saturated residual magnetization state (M_{rs}) of the microcubes and (**d**) The relative residual magnetization (M_r/M_{rs}, where M_r is the residual magnetism) of the microcubes as a function of the strength of initially applied magnetic field, which is in the range of the field strengths used in our experiments.

The focus of this research is the unusual dynamic rearrangement of the assembled chains of microcubes into partially wrapped and bundled states every time the field is toggled on or off. One example of such dynamics is shown in **Figure 2.5**. This phenomenon originates from the change in configurational energy of the assembled chain, which can be divided into two major components: (1) field-dipole and (2) dipole-dipole interaction energies. The field-dipole interaction predominates in the presence of the external field, which extends the dipolar chain into a stretched linear configuration (**Fig. 2.5a**). Upon eliminating this field, the quasi-equilibrium configuration is governed by the residual dipole-dipole interaction energies, resulting in a collapsed, self-folded structure (**Fig. 2.5b**). As we explain in detail below, the pattern of this rearrangement is determined by the sequence of the patchy cubes with coated sides facing in the same or opposite direction along the chain (analogically to "cis/trans" orientation).

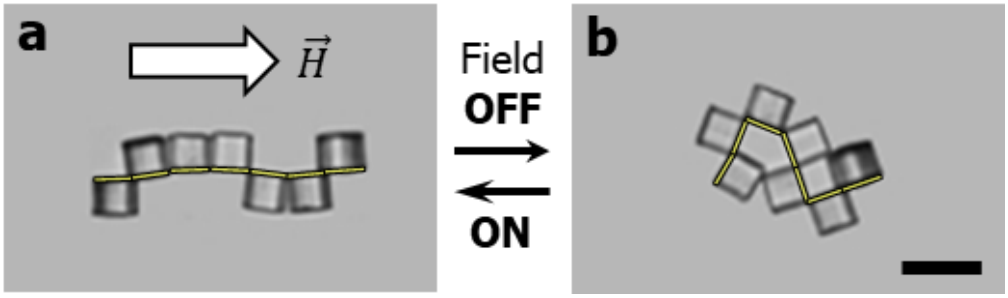

Figure 2.5: Magnetic field driven self-reconfiguration of an assembled cluster. (**a**) Example of a linear chain of patchy microcubes formed upon the application of uniform magnetic field. (**b**) Reversible self-reconfiguration of the linear chain in (**a**) into a structure of two closed loops upon removing the applied field**.** The superimposed yellow lines denote the magnetic patches. scale bar: 20 μm.

2.3.3 Configurational Interaction of Cube Doublets

To understand the driving forces and control the self-reconfiguration of patchy microcube chains, we first analyze the interactions between microcube doublets. The two basic sequence units attained by a doublet are illustrated in **Figure 2.6**. We refer to the sequence as *AB* when the cube

body of the two adjacent microcubes is on the *opposite* side of the plane of metal patches, and conversely *AA* denotes a sequence of two cubes on the *same* side of the metal plane. Depending upon the type of doublet (i.e., *AA* or *AB*), the energetics of the magnetic dipolar interactions upon removing the external field leads to two distinct responses. These configurational interaction can be modeled on the basis of two independent finite dipoles,[31,32] which will be discussed in detail below. Briefly, in the case of an *AB* sequence, the two adjacent microcubes form a rigid link due to partial overlap between the metallic patches, whereby two adjoining residual dipoles have minimized their interaction energy, resulting in rigid bonding (**Fig. 2.6a**). In contrast, when the metallic patches are on the same side, as in the *AA* sequence, the magnetic interaction energy between the residual dipoles is minimized by self-folding of the doublet along the common vertex when the external field is removed (**Fig. 2.6b**).

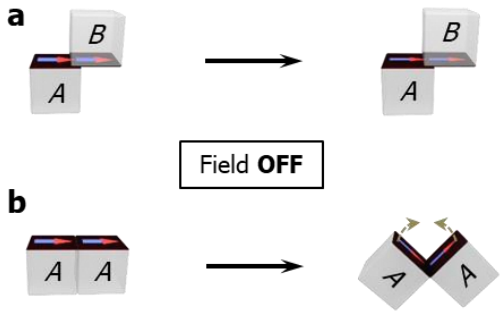

Figure 2.6: Schematics of the two basic unit doublets, *AB* and *AA*, which correspond to assembled particles on the same side or opposite sides of the assembled magnetic films, respectively. Upon removal of an external magnetic field, *AB* in (**a**) shows no reconfiguration while *AA* in (**b**) self-folds to minimize the magnetic interaction energy between the metallic patches.

As long as the magnetic field is applied, the field-dipole interactions dominate and enable the assembled chains to align along the direction of the field. Once the applied field is removed, however, the residual dipole-dipole interaction determines the quasi-equilibrium configuration of the assembled chains. To estimate the equilibrium configurations, the dipolar interaction between two dipoles of finite length 2*l* can be analytically characterized by the equation:[31,32]

$$E_{\text{int}} = \frac{\mu_0}{4\pi}\left(\frac{m}{2l}\right)^2 \sum_{x=1}^{2}\sum_{y=1}^{2}\left[\frac{(-1)^{x\text{-}y+1}}{\left|\vec{r}_{ij} + l\{(-1)^x \vec{n}_i + (-1)^y \vec{n}_j\}\right|}\right]$$

$$= \frac{\mu_0}{4\pi}\left(\frac{m}{2l}\right)^2 \left[\frac{1}{\left|\vec{r}_{ij} + l(\vec{n}_i - \vec{n}_j)\right|} - \frac{1}{\left|\vec{r}_{ij} + l(\vec{n}_i + \vec{n}_j)\right|} - \frac{1}{\left|\vec{r}_{ij} + l(-\vec{n}_i - \vec{n}_j)\right|} + \frac{1}{\left|\vec{r}_{ij} + l(-\vec{n}_i + \vec{n}_j)\right|}\right] \quad \textbf{(Equation 2.1)}$$

$$= \frac{\mu_0}{4\pi}\left(\frac{m}{2l}\right)^2 \left[\frac{1}{|\vec{r}_{13}|} - \frac{1}{|\vec{r}_{14}|} - \frac{1}{|\vec{r}_{23}|} + \frac{1}{|\vec{r}_{24}|}\right] \quad \textbf{(Equation 2.2)}$$

where μ_0 is the permeability of free space ($4\pi \times 10^{-7}$ H/m), m is the residual magnetic moment, $2l$ is the length of each dipole. In **Equation 2.1**, $\vec{r}_{ij}$ is the position vector between the centers of each dipole, $\vec{n}_i$ and $\vec{n}_j$ (the right top inset of **Fig. 2.7**). In **Equation 2.2**, an equivalent form of **Equation 2.1**, $\vec{r}_{13}$, $\vec{r}_{14}$, $\vec{r}_{23}$ and $\vec{r}_{24}$ are the position vector between magnetic charges (the right bottom inset of **Fig. 2.7**). For $l \rightarrow 0$, the **Equation 2.1** is transformed into the well-known point-dipole equation, $E_{\text{point}} = \frac{\mu_0}{4\pi}\frac{m^2}{r_{ij}^3}(\cos\alpha - 3\cos^2\beta)$ where $\frac{\alpha}{2} = \beta = \gamma$ for the case of symmetric folding (the right top inset of **Fig. 2.7**), using Taylor series expansion.[33] The main challenge to use the point-dipole model for our system is that the point-dipole approximation is only valid when the mean distance between dipoles is much larger than the lengths of the dipoles,[31,32] which is not the case for the metallic patch-to-patch overlap of *AB* sequence and *C* configuration (**Fig. 2.7**). To address this limitation, we assumed that positive and negative magnetic charges are separately distributed along each Co patch with the finite length of $2l$, and we calculated the dipolar interaction energy based on the following assumptions: 1) the metallic patch-to-patch separation is 50 nm, considering surface roughness and surfactant layer; 2) the length of the finite dipole is 9.3±0.4 μm, as estimated by measuring the overlapping length of *AB* sequences SEM images (**Fig. 2.3c**); 3) the two-dimensional axial symmetry approximation: the width of finite dipole is 200 nm, taken from Ref. 33 where the finite-dipole model explains the interaction between magnetic nanorods (6 μm in length and 200 nm in diameter).

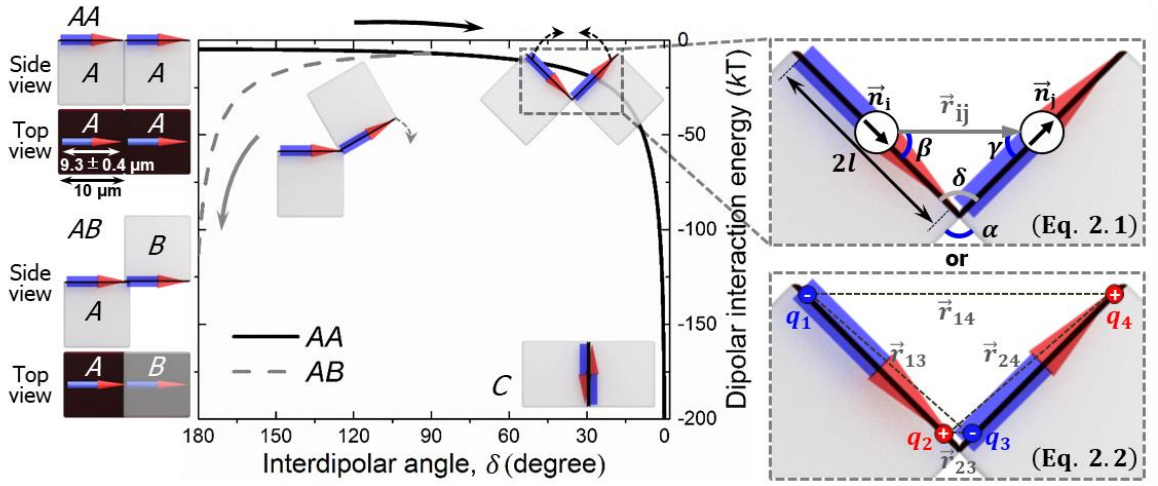

Figure 2.7: Calculation of the dipole-dipole interaction energy for patchy microcube doublets as a function of bending angle in the absence of an external magnetic field. The black solid line represents the trajectory of the spontaneous self-folding motion of an *AA* doublet into a *C* configuration (where the global minimum occurs at $\delta = 0°$). The grey dashed line reveals that the *AB* doublet favors its initial configuration of the local minimum at $\delta = 180°$. The top right inset (indicating the key parameters of **Eq. 2.1**) illustrates the interaction between two dipoles of finite length $2l$ in terms of the unit vector of each dipole, $\vec{n}_i$ and $\vec{n}_j$, and the position vector $\vec{r}_{ij}$ between $\vec{n}_i$ and $\vec{n}_j$, where α is the angle between $\vec{n}_i$ and $\vec{n}_j$, β is the angle between $\vec{n}_i$ and $\vec{r}_{ij}$, γ is the angle between $\vec{n}_j$ and $\vec{r}_{ij}$, and δ is the interdipolar angle, $180 - \alpha$. The right bottom inset (indicating the key parameters of **Eq. 2.2**, an equivalent form of **Eq. 2.1**) illustrates the interaction between two dipoles of finite length $2l$ in terms of the position vector between magnetic charges, $\vec{r}_{13}$, $\vec{r}_{14}$, $\vec{r}_{23}$ and $\vec{r}_{24}$, which are separately distributed along each Co patch.

After removing the external magnetic field, the Co patch on each cube retains a residual magnetic dipole moment of a finite length that can be expressed by the positive and negative magnetic charges, as shown in the right bottom inset of **Figure 2.7**. The smaller dipole length (≈9.3±0.4 μm) with respect to geometric edge of the microcube (10 μm) leads to a slight difference in the dipole-dipole separation length, $\vec{r}_{23}$, in *AB* sequences compared to *AA* sequences. This is because the *AB* doublet possesses the shortest possible length of dipole-dipole separation, $\vec{r}_{23}$, as the adjacent cubes partially overlap such that the dipoles attain an effective head-to-tail orientation, which is conformationally impossible for the *AA* doublet (e.g., see **Fig. 2.3**, where *AB* links within the assembled chain share a small, but non-negligible overlap). Accordingly, the *AB* doublet has a

lower energy than the *AA* doublet at $\delta = 180°$. The *AB* doublet shows no reconfiguration after the field is removed as it achieves a local energy minimum at 180°. Accessing its conformationally bended state ($180° > \delta > 90°$) would require additional energy input (as indicated by the grey dotted line in **Fig. 2.7**). In contrast, the dipoles in the *AA* doublet energetically favor a process of self-folding into an antiparallel side-by-side orientation (as indicated by the black solid line in **Fig. 2.7**), whereby a global energy minimum is obtained at $\delta = 0°$, upon removal of the external magnetic field.

2.3.4 Cluster Folding Rules: Identifying Reversibly Reconfigurable Cube Triplets

A variety of self-reconfiguring and actuating structures could be obtained by programming the sequence of *AB* and *AA* configurations along a larger chain-like assembly. In order to analyze the phenomenon, we focus on the change in the residual dipole-dipole interaction energy of small cluster ensembles (i.e., *AA*, *AAA* and *AAB*), which is analytically calculated using the **Equation 2.1** (or **Equation 2.2**) as shown in **Figure 2.8a**.

In the case of the *AA*, *AAA* and *AAB* chain sequences, the linear microcube clusters self-fold upon removing the field (**Fig. 2.8b-j**), reaching a state with a deep minimum of the interaction energy between the residual dipoles in the reorganized metal patches (**Fig. 2.8a**). In the simplest case, an *AA* doublet, the ground state is achieved as $|\overline{\delta}| \to 0°$, where the two adjacent dipoles are antiparallel. We refer to this structure as configuration *C* (**Fig. 2.8d**). At this configuration, the magnetized patches of the two cubes attract strongly and are inseparable by reintroduction of the external field (**Fig. 2.8c-d**). The interaction of the residual magnetic dipoles in the *AAA* sequence leads to the formation of a triangular cyclic shape after the external field is removed (**Fig. 2.8f**). This structure is metastable and further collapses into the lower energy permanent *AC*

configuration upon reintroduction of the field (**Fig. 2.8f-g).** The formation of such non-reconfigurable states can be averted by programming the sequence of the microcube chain to include spatial restriction/barrier against its collapse into ground state. The simplest example of such spatial restriction is encountered in the sequence *AAB*, where the steric constraint of the *AB* link physically blocks the first microcube *A* from completely closing on the second one and prevents the formation of a non-reconfigurable collapsed state, *AC* sequence. This steric restriction leads to completely reversible reconfiguration (between the states shown in **Fig. 2.8i-j**) each time the external magnetic field is toggled on or off.

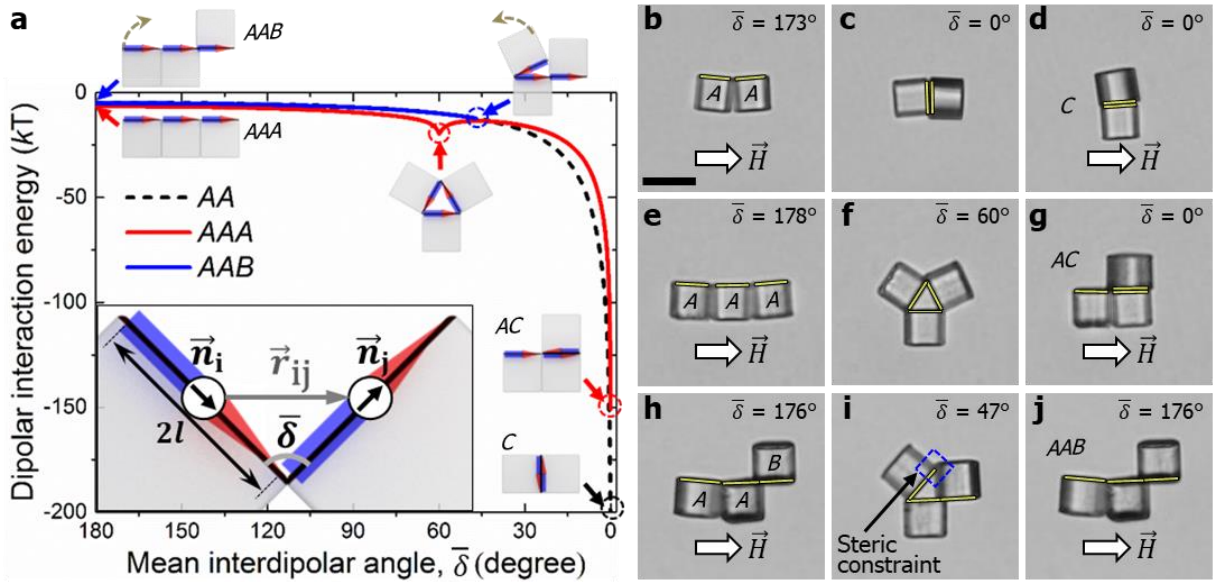

Figure 2.8: Reconfiguration patterns of short chains of microcubes driven by dipole-field and residual dipole-dipole interactions. (**a**) Change in the magnetic dipolar energy per microcube during the reconfiguration process as a function of the interdipolar angle $\bar{\delta}$, the angle between planes of magnetic patches on adjacent microcubes, adapting self-folding toward the ground state. The inset illustrates the interaction between two dipoles of finite length $2l$ in terms of the unit vector of each dipole, $\vec{n}_i$ and $\vec{n}_j$, and the position vector $\vec{r}_{ij}$ between $\vec{n}_i$ and $\vec{n}_j$. (**b-j**) Snapshots of the reconfiguration patterns intrinsic to *AA*, *AAA* and *AAB* sequences. After the applied field is removed, the microcube chains self-fold (**b-c**, **e-f** and **h-i**) until (i) a ground state configuration is attained (e.g., **c**), (ii) a metastable structure is formed (e.g., **f**) or (iii) a sterically restricted conformation is attained (e.g., **i**). When the external field is imposed again, (i) the ground state configuration *C* is retained (e.g., **d**), (ii) the metastable *AAA* structure usually reconfigures into *AC* (e.g., **g**), (iii) and the partially wrapped structure *AAB* re-attains its initial stretched state (e.g., **j**). Scale bar = 20 μm.

2.3.5 Sequence-Controlled Assembly of Multi-Cube Clusters

One route to programmed assembly of reconfigurable multi-cube chains is magnetic rotation of the assemblies and sequential addition of single cubes to their chains. By modifying the field parameters, one can dynamically alter the orientation of the chains as a means to control its relative sequence (i.e., the overall sequence is conserved, but the orientation is changed). As an example, a chain with a *BAA* sequence was converted to a different sequence (e.g., *BBA* or *ABB*) by modifying its orientation. **Figure 2.9** shows two distinct conversions (i.e., *BAA*→*BBA*→*ABB*), which are both controlled by altering the magnetic field direction and strength. First, by gradually decreasing the strength of the magnetic field to 0 A/m, and by increasing the strength of the field back to the same magnitude in the opposite direction, a chain with a *BAA* sequence can rotate about the z-axis and effectively convert to a chain with a *BBA* sequence relative to the same viewing plane. Then, by rapidly reversing the direction of the field from left to right with the same magnitude, the *BBA* chain can rotate about y-axis and effectively convert to a chain with an *ABB* sequence. Therefore, we note that the *BAA*, *BBA*, *ABB* and *AAB* chain sequences can be defined as members of the *ABB* chain family.

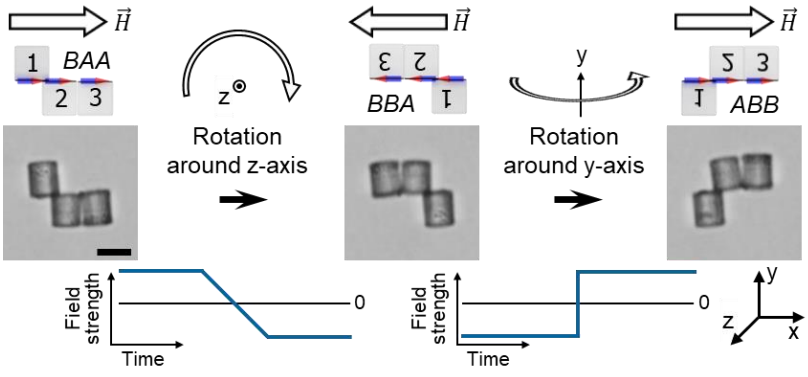

Figure 2.9: Chain reorientation techniques for reprogramming the relative sequence of a microbot assembly (*BAA*→*BBA*→*ABB*). The first conversion (i.e., *BAA*→*BBA*) is achieved by a 180° z-axis rotation via gradually switching the magnetic field from -0.8 kA/m to +0.8 kA/m. The second conversion (i.e., *BBA*→*ABB*) is achieved by a 180° y-axis rotation via rapidly switching the magnetic field from +0.8 kA/m to -0.8 kA/m. The numbers 1, 2 and 3 on the schematic are correspondingly reoriented along with the cubes during the conversions. Scale bar = 10 μm.

Using the chain reorientation principles described above, we controlled the orientation of three cubes (as an example) prior to assembly as a means to program their sequence within an ordered chain. More specifically, we reoriented a chain with a *BBA* sequence (i.e., within the *ABB* chain family) to display an *ABB* sequence from the view of observation and to assemble with a single cube to form a chain with an *ABBA* sequence (**Fig. 2.10**). Initially, given the relative orientation of the *BBA* chain and the single cube in an *"A"* orientation, a *BBAA* chain sequence would emerge if the magnetic field were continuously applied. However, by rapidly reversing the direction of the field from right to left with the same magnitude to induce the 180° y-axis rotation, the *BBA* chain reoriented into an *ABB* chain, which allowed it to assemble with the cube in an "*A"* orientation (having an unchanged orientation due to its lower responsiveness to the applied field) into a reconfigurable *ABBA* microbot (**Fig. 2.11a**). In more scalable, parallelized fabrication of such structures, an underlying template may allow the assembly of preprogramed sequences on a large scale by directing the cubes onto patterned micromagnets.[34]

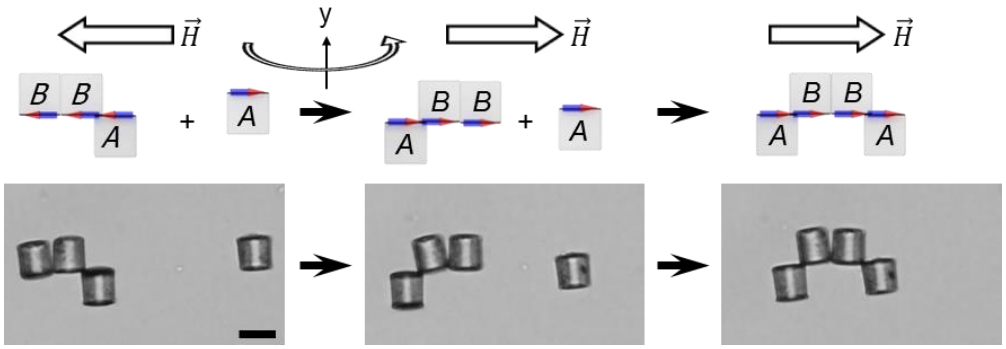

Figure 2.10: Chain reorientation technique to program the sequence of a microbot**.** A *BBA* chain is reoriented into an *ABB* chain by a y-axis rotation via rapidly changing the magnetic field strength from -0.8 kA/m to +0.8 kA/m. The continuous field application then leads to the assembly of an *ABBA* chain from the newly oriented *ABB* chain and a single cube with an "*A*" orientation. Scale bar = 10 μm.

2.3.6 Sequence-Encoded Dynamic Reconfiguration of Cube Quadruplets

Two key examples of dynamic reconfiguration are revealed by "isomeric" clusters of four microcubes, whose sequence encodes distinct field-triggered reconfiguration patterns (**Fig. 2.11a**). The *ABBA* assembly forms a cyclic configuration that opens and closes on demand, while the *BBAA* cluster symmetrically wraps and unwraps. The rate of self-folding can be tuned by the magnitude of the applied external magnetic field. For an *ABBA* sequence, for example, the folding rate is proportional to $|\vec{H}^2|$, where $|\vec{H}|$ is the strength of initially applied magnetic field (**Fig. 2.11b**). Such dependencies are typical for second-order field-induced interactions and dynamics [35].

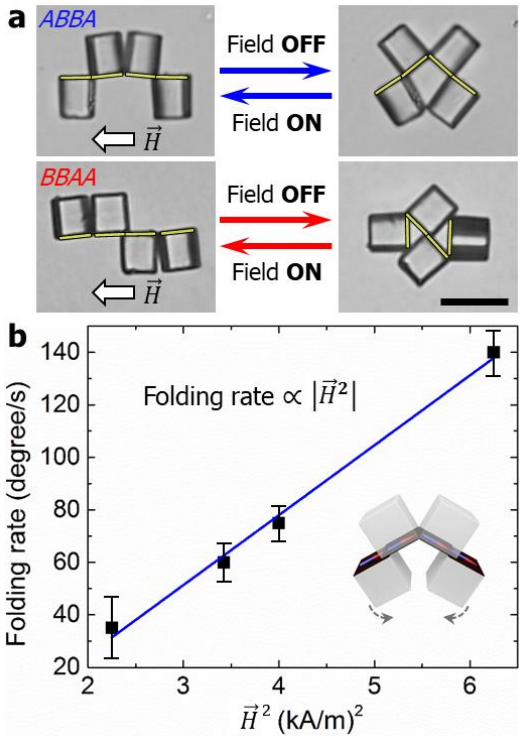

Figure 2.11: Examples of dynamic reconfiguration of chain sequences comprising four microcubes. (**a**) Snapshots of field-on and -off states of the four particle colloidal isomers, i.e., *ABBA* and *BBAA*. Scale bar = 20 µm. (**b**) Dependence of folding rate measured for the initial 0.5 s of the *ABBA* microcube sequence on the applied magnetic field strength after the field is removed. The folding rate is linearly dependent on the square of the strength of initially applied magnetic field. The error bars correspond to the standard deviation of the folding rate per the square of the field strength from 5 different *ABBA* structures.

The dynamics of the self-folding and field-driven unfolding can be expressed in terms of change in interdipolar angle (or mean interparticle angle), $\bar{\delta}$, with time over repeated folding cycles (**Fig. 2.12**). *ABBB*, *ABBA* and *BBAA* chain sequences exhibit consistent self-folding and unfolding motions with remarkable dexterity over 20 or more field-off-and-on duty cycles. Whereas the *AAAA* chain sequence reconfigures to the *CC* configuration after the first cycle; it does not display any further reconfiguration. We found that the folding rate (i.e., the slope of interdipolar angles, $\bar{\delta}$ *vs.* time) measured for the initial 0.5 s remains independent. The magnitude of the inertial torque is balanced by the viscous torque of the surrounding fluid, thus resulting in such a constant terminal bending speed.[36]

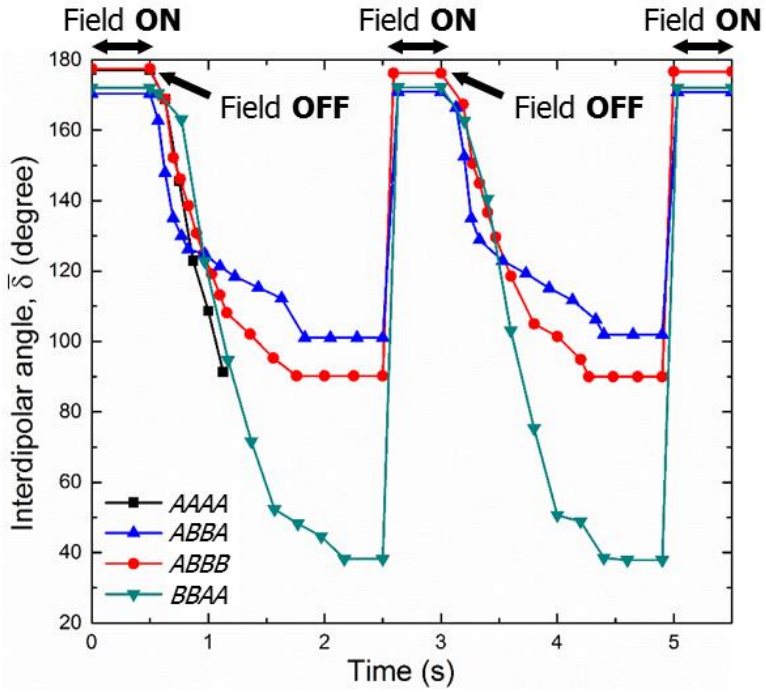

Figure 2.12: The kinetics of the self-reconfiguration of four particle clusters expressed by mean interparticle (≡ interdipolar) angle $\bar{\delta}$. Changes in the interdipolar angle for clusters with an *ABBA*, *ABBB* and *BBAA* sequence from two consecutive folding cycles are shown in this diagram. The self-reconfiguration of an *AAAA* particle cluster is also shown in this diagram.

2.3.7 Examples of Microbots and Colloidal Origami with Sequence-Encoded Function

The reversible, sequence-dependent, reconfiguration described above is actuated by a uniform magnetic field. A further level of control over the dynamics of these assemblies can be achieved by superimposing a non-uniform gradient magnetic field ($\nabla\vec{H}$) that can remotely translocate the assemblies. We illustrate how, by combining the uniform field-triggered reversible actuation with field gradient-driven spatial navigation, a microcube assembly with a *BABBAB* sequence can form a prototype of a microbot that can manipulate single live cells. Snapshots of this microbot grabbing, transporting and releasing a target yeast cell are shown in **Figure 2.13a-e**. The microbot cluster is transported to the target location in its open configuration (**Fig. 2.13a**) by the application of a transversal uniform magnetic field with an imposed additional longitudinal gradient (by turning on all three coils **1**, **2**, **3** in **Fig. 2.1**). In the subsequent step, the transverse magnetic field is removed, resulting into chain self-folding into the closed state. Thus, the cluster acts as a "micro-tweezer" and captures the target yeast cell. The cell is then transported in two-dimensional space by tuning the magnitude and direction of the applied magnetic field gradient (**Fig. 2.13c-d**). Upon reaching a target location, the yeast cell is released by activating the uniform magnetic field (**Fig. 2.13e**).

To verify and illustrate the origin of the dynamics of these assemblies, we simulated the different scenarios of field interaction with a *BABBAB* microbot using COMSOL^{TM} Multiphysics software package (**Fig. 2.13f-j**). For simplicity, the calculations were carried out in two dimensions, where the three-dimensional microcube was represented as a square and the magnetic plane as a rectangular patch on one of its sides. The calculated field distribution, plotted by color-coding, elucidates the migration of the chain structure in the direction of positive magnetic field gradient (**Fig. 2.13f, h**). This analysis confirms the role of the applied uniform magnetic field in

unfolding the chain (**Fig. 2.13g, j**) and shows that the re-configuration of the microbot in the absence of external field is driven by strong cluster-localized magnetic interactions (as shown by the location of the high field intensity areas in **Fig. 2.13i, h**).

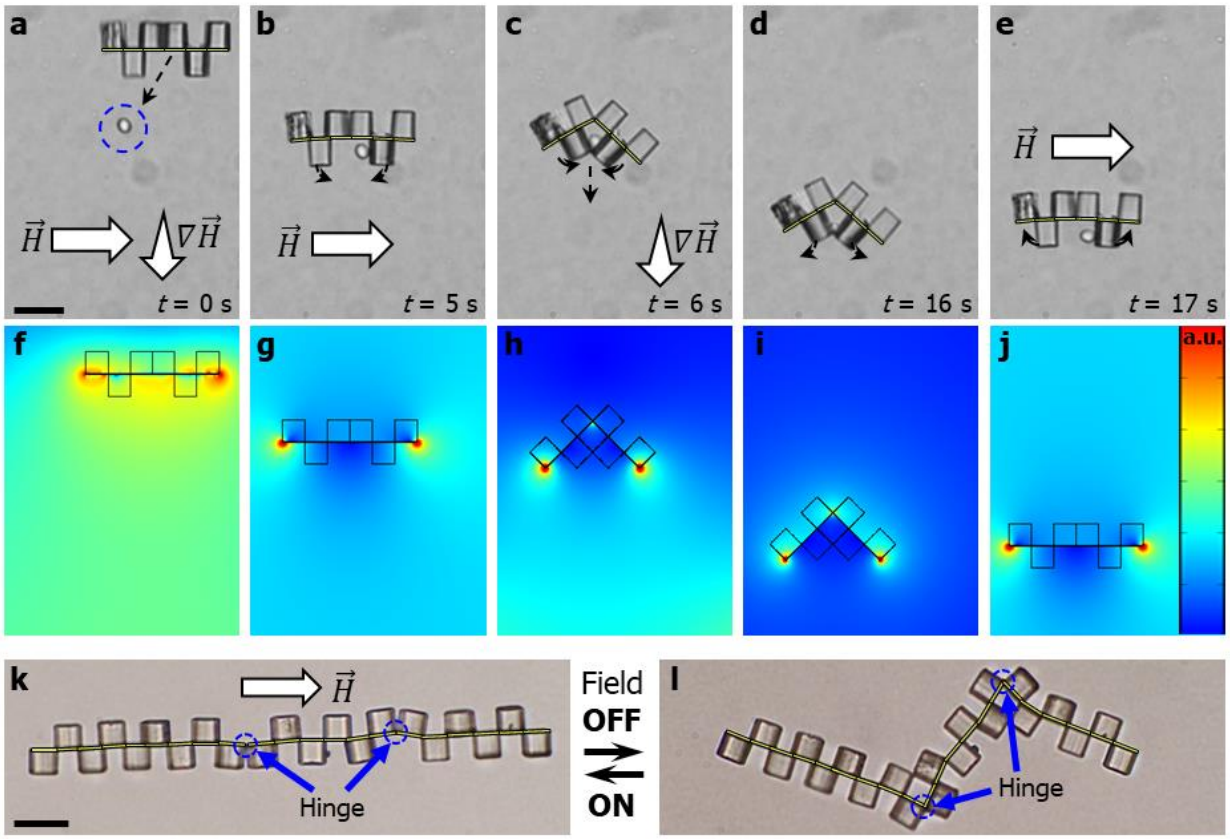

Figure 2.13: Microcube assemblies as prototypes of microbots for transporting cells and as colloidal origami. (**a-e**) Snapshots of a microbot comprising six microcubes (*BABBAB*) used for transporting a yeast cell. (**a**) Spatial migration of the assembly in its open state under uniform external magnetic field with longitudinally imposed gradient. (**b**) The microcube chain is brought to the yeast cell by attraction along the gradient. (**c**) The cluster self-closes upon removing the uniform field, which results in the capture of the yeast cell. (**d**) The microbot is transported to the target location by a magnetic gradient force. (**e**), Finally, the cell is released by re-activating the uniform magnetic field. (**f-j**) Distribution of magnetic field intensity around the *BABBAB* assembly during each stage of manipulation shown in (**a-e**), as calculated by COMSOL™ Multiphysics. (**k-l**) Snapshots of a repeatedly self-reconfigurable multi-cube chain as an example of programmable colloidal origami. Scale bars in (**a**) and (**k**) = 20 µm.

The *BABBAB* "microbot" is one of many possible examples of small, reversibly actuatable clusters. A larger scale application of longer "origami" chains could involve embedding reversibly

collapsible chains within flexible matrices for making responsive materials that can be expanded, contracted or folded by magnetic fields. We present one example of such reconfigurable chains in **Figure 2.13k-l**. As highlighted by the blue circles (**Fig. 2.13k-l**), the folding behavior is consistently observed at either the *AA* or *BB* "hinge" segments, even within a large cluster.

2.4 Conclusion

We demonstrate how microcubes with one metal-coated side can be assembled into structures that store and release magnetic field energy when the steric constraints of their cubic building blocks guide their residual magnetic interactions. These assemblies attain various equilibrium and non-equilibrium states, depending upon the sequence of the microcubes, which make it possible to program their self-folding and wrapping patterns. Field-manipulated "microbot" clusters with sequence-determined folding pattern and function (**Fig. 2.13**) may find utility in soft robotics, microsurgery, biological separation and bioinspired colloidal origami.[37] In addition to biological manipulations on the microscale, these assemblies can be used to locally probe and interact with their microenvironment. As an example, we will show that reversible self-reconfiguration of specific microcube chains could lead to new classes of "active" microswimmers for biological non-Newtonian media in the following chapter. Since the engineered metallic patches provide a foundation for effective magnetic energy storage, the principles of this simple platform actuator can be extended to more advanced, hierarchical structures by using more complex particle shapes, compositions, and field parameters to address a broad range of applications, from robotics and micromanipulation, to responsive materials and on-demand reconfigurable structures.

2.5 Acknowledgements

We acknowledge S. Roh, J. C. Ledford and L. Reynolds for useful discussions and experimental assistance. This work was supported by the NSF Research Triangle MRSEC (DMR-1121107), NSF grant CBET-1604116, and an NSF graduate research fellowship to C. W. Shields IV (GRF-1106401).

2.6 References

[1] J. Wang, W. Gao. Nano/Microscale Motors: Biomedical Opportunities and Challenges. *ACS Nano* **2012**, *6*, 5745.

[2] B. J. Nelson, I. K. Kaliakatsos, J. J. Abbott. Microrobots for Minimally Invasive Medicine. *Annu. Rev. Biomed. Eng.* **2010**, *12*, 55.

[3] M. Sitti. Voyage of the Microrobots Speciation Affects Ecosystems. *Nature* **2009**, *458*, 1121.

[4] S. Tasoglu, E. Diller, S. Guven, M. Sitti, U. Demirci. Untethered Micro-Robotic Coding of Three-Dimensional Material Composition. *Nat. Commun.* **2014**, *5*, 3124.

[5] E. Diller, M. Sitti. Three-Dimensional Programmable Assembly by Untethered Magnetic Robotic Micro-Grippers. *Adv. Funct. Mater.* **2014**, *24*, 4397.

[6] L. Cademartiri, K. J. M. Bishop. Programmable Self-Assembly. *Nat. Mater.* **2015**, *14*, 2.

[7] S. C. Glotzer, M. J. Solomon. Anisotropy of Building Blocks and Their Assembly into Complex Structures. *Nat. Mater.* **2007**, *6*, 557.

[8] O. D. Velev, S. Gupta. Materials Fabricated by Micro- and Nanoparticle Assembly - The Challenging Path from Science to Engineering. *Adv. Mater.* **2009**, *21*, 1897.

[9] Y. Wang, Y. Wang, D. R. Breed, V. N. Manoharan, L. Feng, A. D. Hollingsworth, M. Weck, D. J. Pine. Colloids with Valence and Specific Directional Bonding. *Nature* **2012**, *491*, 51.

[10] O. D. Velev, K. H. Bhatt. On-Chip Micromanipulation and Assembly of Colloidal Particles by Electric Fields. *Soft Matter* **2006**, *2*, 738.

[11] B. Bharti, G. H. Findenegg, O. D. Velev. Co-Assembly of Oppositely Charged Particles into Linear Clusters and Chains of Controllable Length. *Sci. Rep.* **2012**, *2*, 1004.

[12] H. Schmidle, S. Jäger, C. K. Hall, O. D. Velev, S. H. L. Klapp. Two-Dimensional Colloidal Networks Induced by a Uni-Axial External Field. *Soft Matter* **2013**, *9*, 2518.

[13] B. Bharti, G. H. Findenegg, O. D. Velev. Analysis of the Field-Assisted Permanent Assembly of Oppositely Charged Particles. *Langmuir* **2014**, *30*, 6577.

[14] M. Grzelczak, J. Vermant, E. M. Furst, L. M. Liz-marza. Directed Self-Assembly of Nanoparticles. *ACS Nano* **2010**, *4*, 3591.

[15] Z. Nie, A. Petukhova, E. Kumacheva. Properties and Emerging Applications of Self-Assembled Structures Made from Inorganic Nanoparticles. *Nat. Nanotechnol.* **2010**, *5*, 15.

[16] J. Kim, S. E. Chung, S.-E. Choi, H. Lee, J. Kim, S. Kwon. Programming Magnetic Anisotropy in Polymeric Microactuators. *Nat. Mater.* **2011**, *10*, 747.

[17] J. Ge, Y. Yin. Responsive Photonic Crystals. *Angew. Chemie - Int. Ed.* **2011**, *50*, 1492.

[18] S. Sacanna, L. Rossi, D. J. Pine. Magnetic Click Colloidal Assembly. *J. Am. Chem. Soc.* **2012**, *134*, 6112.

[19] Y. Yang, L. Gao, G. P. Lopez, B. B. Yellen. Tunable Assembly of Colloidal Crystal Alloys Using Magnetic Nanoparticle Fluids. *ACS Nano* **2013**, *7*, 2705.

[20] T. Lin, W. Huang, I. Jun, P. Jiang. Bioinspired Assembly of Colloidal Nanoplatelets by Electric Field. *Chem. Mater.* **2009**, *21*, 2039.

[21] E. Bukusoglu, M. Bedolla Pantoja, P. C. Mushenheim, X. Wang, N. L. Abbott. Design of Responsive and Active (Soft) Materials Using Liquid Crystals. *Annu. Rev. Chem. Biomol. Eng.* **2016**, *7*, 163.

[22] B. Bharti, A.-L. Fameau, M. Rubinstein, O. D. Velev. Nanocapillarity-Mediated Magnetic Assembly of Nanoparticles into Ultraflexible Filaments and Reconfigurable Networks. *Nat. Mater.* **2015**, *14*, 1104.

[23] B. Bharti, D. Rutkowski, K. Han, A. U. Kumar, C. K. Hall, O. D. Velev. Capillary Bridging as a Tool for Assembling Discrete Clusters of Patchy Particles. *J. Am. Chem. Soc.* **2016**, *138*, 14948.

[24] A. Kaiser, A. Snezhko, I. S. Aranson. Flocking Ferromagnetic Colloids. *Sci. Adv.* **2017**, *3*, e1601469.

[25] B. Bharti, O. D. Velev. Assembly of Reconfigurable Colloidal Structures by Multidirectional Field-Induced Interactions. *Langmuir* **2015**, *31*, 7987.

[26] J. Yan, K. Chaudhary, S. Chul Bae, J. A. Lewis, S. Granick. Colloidal Ribbons and Rings from Janus Magnetic Rods. *Nat. Commun.* **2013**, *4*, 1516: 1.

[27] A. A. Shah, B. Schultz, W. Zhang, S. C. Glotzer, M. J. Solomon. Actuation of Shape-Memory Colloidal Fibres of Janus Ellipsoids. *Nat. Mater.* **2014**, *14*, 117.

[28] A. Snezhko, I. S. Aranson. Magnetic Manipulation of Self-Assembled Colloidal Asters. *Nat. Mater.* **2011**, *10*, 698.

[29] A. Ruditskiy, B. Ren, I. Kretzschmar. Behaviour of Iron Oxide (Fe_3O_4) Janus Particles in Overlapping External AC Electric and Static Magnetic Fields. *Soft Matter* **2013**, *9*, 9174.

[30] C. W. Shields IV, S. Zhu, Y. Yang, B. Bharti, J. Liu, B. B. Yellen, O. D. Velev, G. P. López. Field-Directed Assembly of Patchy Anisotropic Microparticles with Defined Shape. *Soft Matter* **2013**, *9*, 9219.

[31] M. D. Costa, Y. G. Pogorelov. Criteria for Long-Range Magnetic Order in Planar Lattices of Dipolar Coupled Magnetic Nanoparticles. *Phys. Status Solidi A* **2001**, *927*, 923.

[32] Y. Gu, R. Burtovyy, J. Custer, I. Luzinov, K. G. Kornev. A Gradient Field Defeats the Inherent Repulsion between Magnetic Nanorods. *R. Soc. Open Sci.* **2014**, *1*, 140271.

[33] E. Z. Meilikhov, R. M. Farzetdinova. Magnetic Properties of a Random System of Rodlike Ising Dipoles. *J. Exp. Theor. Phys.* **2003**, *97*, 593.

[34] A. F. Demirörs, P. P. Pillai, B. Kowalczyk, B. A. Grzybowski. Colloidal Assembly Directed by Virtual Magnetic Moulds. *Nature* **2013**, *503*, 99.

[35] R. M. Erb, J. J. Martin, R. Soheilian, C. Pan, J. R. Barber. Actuating Soft Matter with Magnetic Torque. *Adv. Funct. Mater.* **2016**, *26*, 3859.

[36] A. W. Mahoney, J. J. Abbott. Managing Magnetic Force Applied to a Magnetic Device by a Rotating Dipole Field. *Appl. Phys. Lett.* **2011**, *99*, 134103.

[37] C. M. Andres, J. Zhu, T. Shyu, C. Flynn, N. A. Kotov. Shape-Morphing Nanocomposite Origami. *Langmuir* **2014**, *30*, 5378.

Chapter 3

Active Swimming of Self-Assembled Microbots in Non-Newtonian Fluids*

* Partially based on Han and Velev *et al*., Manuscript in preparation

3.1 Introduction

Microscale swimming machines have shown promise for future biomedical applications such as targeted treatment or drug delivery inside the body.[1–5] One major challenge to direct the propulsion of microscale objects in liquid media is overcoming the viscous forces at low Reynolds number (*Re*).[6–8] According to Purcell's "scallop theorem," a reciprocal motion like the one from a single-hinged scallop structure cannot generate net displacement at low *Re* regime (i.e., $Re \ll 1$) in Newtonian fluids due to its time-reversal symmetry.[9] In natural microorganisms the viscous forces at low *Re* are overcome by non-reciprocal deformations of their body, and thus breaking time-reversal symmetry.[10–12] Recent advances in micro- and nanofabrication have enabled the making of artificial swimmers that can mimic the swimming mechanisms of microorganisms such as helical propulsion of *E. coli* and traveling-wave propulsion of sperm flagella.[13–17] Although these early examples have shown promise for motility and performing functions at micron scale,[18–21] they are based on devices that require relatively complex fabrication processes and cumbersome operations.

To reduce the complexity of artificial active machines, one can consider combining simple reciprocal motions with non-Newtonian rheology because the scallop theorem does not hold in non-Newtonian fluids. Although there has been a few reports on investigating swimming dynamics of natural microorganisms in non-Newtonian fluids,[22,23] there is need to understand how the dynamics of artificial swimmers leads to propulsion in fluids with non-Newtonian rheological properties. Microswimmers with a simple actuation mechanism may facilitate understanding the principles of motility in non-Newtonian fluids. In an pioneering example of this approach, Fisher and co-workers reported that a magnetically controlled single-hinged scallop of submillimeter size can generate net displacement by time-asymmetric flapping strokes in non-Newtonian fluids.[24]

Decreasing the size of such swimmers to analyze the propulsion on the microscale remains a challenge due to complexity of top-down fabrication processes. We present here a miniaturized self-propelling "microscallop" device made by bottom-up assembly of micron-size engineered blocks into a single-hinged microscallop using an external magnetic field. It is based on the magnetically reconfigurable assemblies of patchy microcubes discussed in Chapter 2 in which the reconfiguration pattern of the assemblies can be encoded in the sequence of the cube orientations within the assemblies.[25] Assembling these devices in non-Newtonian fluids provides a means of making self-propelling microswimmers based on their sequence-encoded reconfiguration function. This approach also allows for investigating apparently different swimming dynamics of self-assembled devices depending on their geometric design, which can be controlled by the number of building blocks.

3.2 Materials and methods

3.2.1 Materials

One-side coated patchy microcubes were used as building blocks to assemble microswimmer structures. The microcubes were made from SU-8 10 (MicroChem Corp.) via photolithography and coated with 10 nm of Cr followed by 100 nm of Co along their top facet via metal evaporation.[26] The patchy microcubes were assembled in two different types of media: Milli-Q water used as a Newtonian fluid and 0.01wt% xanthan gum (Sigma-Aldrich, Corp.) solution was used as a non-Newtonian fluid. The rheological property of the fluids was characterized using a stress-controlled cone-plate rheometer (AR-G2, TA instruments, Inc.). The xanthan gum solution exhibited a shear-thinning rheological behavior, which is a lower viscosity at a higher shear rate as shown in **Figure 3.1**.

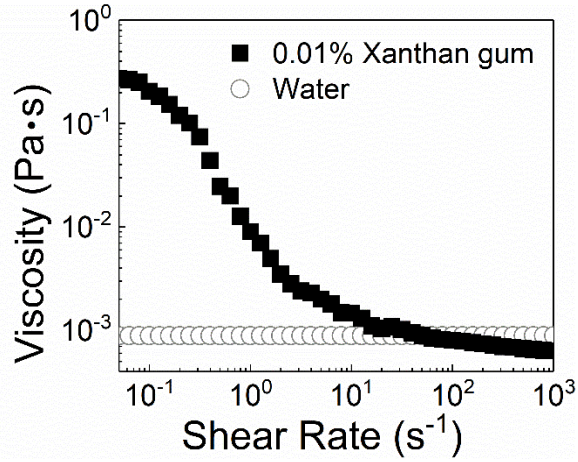

Figure 3.1: Shear-rate dependent viscosity data of water and 0.01wt% xanthan gum solution. Water exhibited constant viscosity regardless of shear rate. The xanthan gum solution exhibited a lower viscosity at a high shear rate revealing shear-thinning non-Newtonian rheological behavior.

3.2.2 Experimental Setup

A 30 μL suspension of the patchy microcubes was injected into the assembly cell (**Fig. 3.2a**) where an imaging spacer (Grace Bio-Labs, Inc.) confined it to a "corral" between a glass slide and a cover slip. The patchy microcubes responded to a uniform magnetic field generated by a collinear pair of electromagnetic coils placed on either side of the assembly cell. The pair of electromagnetic coils was connected to a function generator (33120A, Agilent Technologies, Inc.) to externally control the strength of the magnetic field as a function of time. Three different signals of the function generator were used to generate time-symmetric (**Fig. 3.2b**) and time-asymmetric (**Fig. 3.2c-d**) magnetic fields. The peak strength of the magnetic fields was 5 kA/m, as measured by a gauss meter (GM-2, AlphaLab, Inc.). The assembly cell was housed on the table of an optical microscope (BX-61, Olympus, Co.) to enable the real-time observation of the dynamic behaviors of patchy microcubes. Videos were taken using a CCD camera (DP-70, Olympus, Co.) at 15 frames/sec. The videos were analyzed in ImageJ (NIH, USA) to measure the actuation speed and angle of the assembled microswimmer structures.

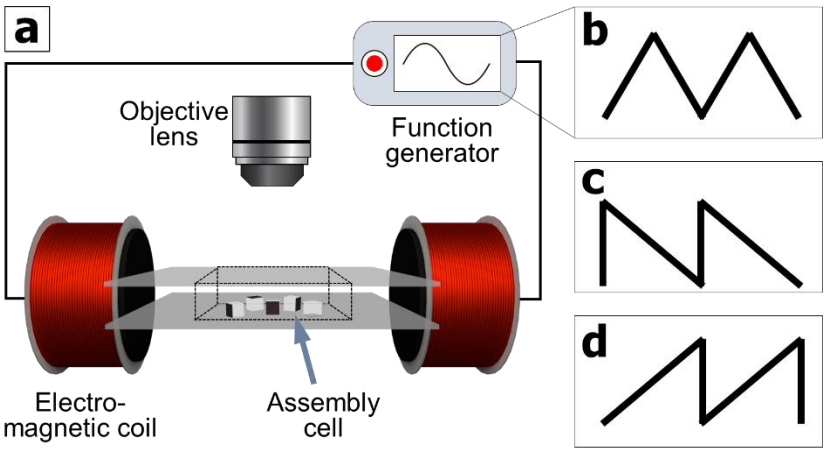

Figure 3.2: (**a**) Schematic of the experimental setup, comprising an assembly cell and a collinear pair of electromagnetic coils connected to a function generator. (**b-d**) Three signal outputs from the function generator to control the strength of the magnetic field as a function of time: (**b**) Time symmetrical gradual increase and decrease in the field strength; (**c**) Time asymmetrical sudden increase and slow decrease in the field strength; (**d**) Time asymmetrical slow increase and sudden increase in the field strength.

3.2.3 Numerical Simulation

Finite element analysis on fluid-structure interaction was performed using ANSYS® modeling software to investigate the local distribution of fluid shear around microswimmer structures during their flapping strokes. The transient structural module was used to model the microswimmer structures in which motion speed and angle were programmed based on our experimental data. Then, the fluid flow module was coupled with the transient structural module through the system coupling module for two-way fluid-structure interaction. Multiphysics simulation of this model system was carried out by solving the equations of the conservation of mass and momentum.

3.3 Results and Discussion

3.3.1 Self-Propulsion Principle of Microscallops

The mechanism of making self-propelling “microscallop” assemblies is schematically described in **Figure 3.3**. Magnetically responsive engineered particles - one-side cobalt coated patchy

microcubes - are dispersed in a liquid medium contained inside a thin chamber (**Fig. 3.2a**). They can be remotely assembled into multi-cube clusters by application of an external magnetic field from a pair of electromagnets. Their assembly patterns can be controlled by sequentially adding single cubes to a target structure, which can be magnetically rotated during the directed cube addition by adjusting the field parameters, as reported earlier.[25] These assemblies can preserve their assembled sequence because of magnetic polarization of the metallic facets, which is retained in the form of residual dipoles even after removal of the field.[27] Switching between directional field-dipole and dipole-dipole interactions of the metallic facets by tuning the magnetic field on and off allows the assembled clusters to reconfigure themselves, as exemplified in **Figure 3.3a**. Upon removal of the field, a scallop-like assembled cluster self-folds to minimize the magnetic interaction energy between the polarized metallic facets, leading to the "closing" stroke (**Fig. 3.3ai→ii**). Upon reintroduction of the field, the folded cluster returns to its original stretched state by co-aligning the metallic facets in the field direction, leading to the "opening" stroke (**Fig. 3.3aii→i**). Consequently, on-demand reciprocal opening and closing stroke of microscallop assemblies can be achieved by merely turning the magnetic field on and off.

The rate of opening and closing stroke of the reconfigurable assemblies can be externally controlled by the strength of a magnetic field as a function of time using a function generator, as exemplified in **Figure 3.3b**. **Figure 3.3c** and **d** illustrate one example of displacement of a self-assembled microscallop under the cycle of slow opening and rapid closing stroke (**Fig. 3.3b**) in different liquid media. Here the experiments were performed in water as a Newtonian fluid (**Fig. 3.3c**) and 0.01wt% xanthan gum solution as a non-Newtonian fluid (**Fig. 3.3d**). We define the virtual magnetic "hinge" of an assembled cluster (highlighted by a red circle) as a coordinate representing the position of the whole cluster, which will be referred to as a central hinge

throughout this manuscript. In the xy-coordinate plane (**Fig. 3.3ai**), the central hinge displaces downward and upward along y-axis during the cycle of reciprocal opening and closing stroke, respectively (**Fig. 3.3c**, **d**). In a Newtonian fluid, the cluster exhibits no net displacement under the complete cycle of either time-symmetric or time-asymmetric reciprocal actuation as it has the similar extent of downward and upward displacement (**Fig. 3.3c**). Because the sequence of cluster reconfiguration by the closing stroke is identical to that by the opening stroke after a time-reversal transformation, at low *Re* the opening and closing strokes guide the same pattern of cluster motion regardless of the difference in their relative stroke speed, which corresponds to the scallop theorem.[9]

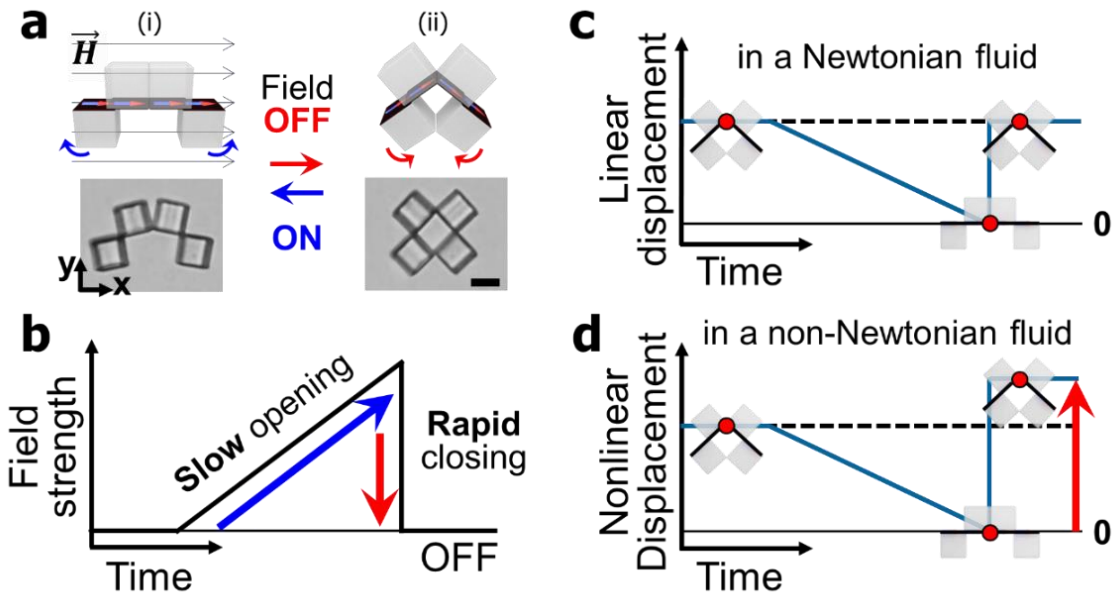

Figure 3.3: Self-propulsion mechanism of a magnetically reconfigurable self-assembled microscallop based on cyclic time-asymmetric reciprocal strokes in non-Newtonian fluids. (**a**) A schematic illustration and a snapshot of a scallop-like assembled cluster exhibiting the closing stroke (**i→ii**) and the opening stroke (**ii→i**) by application and removal of an external magnetic field, respectively. Scale bar: 10 μm. The xy-coordinate plane is presented in the snapshot of (**ai**). (**b**) A diagram depicting the change in the strength of a magnetic field for slow opening and rapid opening stroke. (**c-d**) Displacement of the central hinge (red circle) of the self-assembled microscallop along y-axis under the slow opening and rapid closing stroke by the applied magnetic field in (**b**): (**c**) linear displacement in a Newtonian fluid; (**d**) nonlinear displacement in a non-Newtonian fluid.

In a non-Newtonian fluid, the cluster shows net displacement under the cycle of time-asymmetric slow opening and rapid closing stroke. Similar to the case in the Newtonian fluid, the cluster travels downward during the slow opening stroke. The cluster may travel the same distance upward and there is no net displacement if its closing stroke is also slow. However, upon the rapid closing stroke, the cluster moves further back beyond where it originally was, leading to net displacement (**Fig. 3.3d**). In summary, the cycles of reciprocal opening and closing strokes can lead to net swimming motion only when actuated with a time-asymmetric manner in non-Newtonian fluids. In this scenario, the rapid stroke portion of time-asymmetric strokes plays a key role in nonlinear displacement. Tracking analysis in **Figure. 3.4** confirmed that the nonlinear displacement of the cluster occurred by the rapid closing stroke in a shear-thinning non-Newtonian fluid. In contrast, the cluster showed linear displacement in the Newtonian fluid regardless of its closing speed. This linear displacement persisted with slow closing strokes of the cluster in the non-Newtonian fluid.

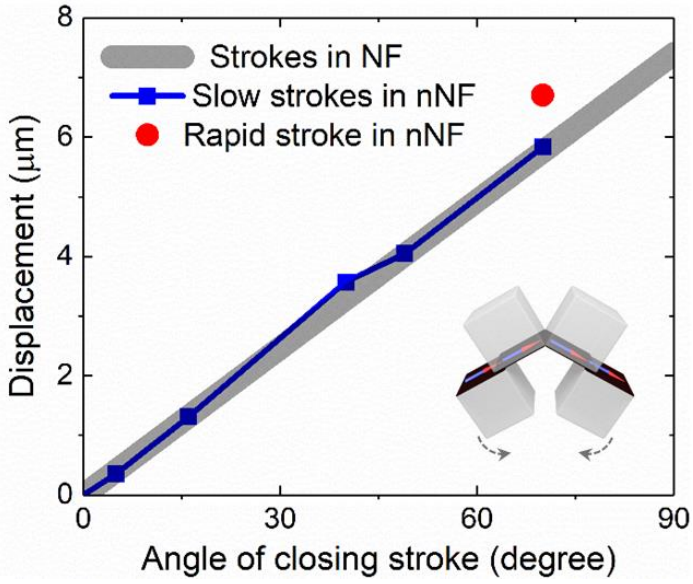

Figure 3.4: Tracking analysis on displacement of the central hinge of the 4-cube symmetric cluster as a function of the angle of closing stroke for strokes in NF (grey line), slow strokes in nNF (blue line) and rapid stroke in nNF (red circle; net displacement). Note: nF represents Newtonian fluid (water in this case); nNF represents non-Newtonian fluid (shear-thinning fluid in this case).

3.3.2 Active Swimming Modes of Microscallops

Active swimming mode of microscallop assemblies depends not only on the type of time-asymmetric flapping patterns, but also on their geometric length and sequence (**Fig. 3.5**). Two distinct assembled forms of microscallops, i.e., 10-cube and 4-cube clusters were actuated with three different reciprocal flapping patterns (i.e., **Fig. 3.5ai**, **bi**, **ci**) in 0.01wt% xanthan gum solution. The shear rate-dependent viscosity data of the xanthan gum solution showed a shear-thinning rheological behavior, characterized by a lower viscosity at a higher shear rate (**Fig. 3.1**).[28] Both a 10-cube and a 4-cube symmetric cluster exhibit no net displacement under the time-symmetric opening and closing stroke (**Fig. 3.5a**). This is likely because the extent of y-directional downward and upward displacement of each cluster is almost the same while their arms flap back and forth with similar speed. In contrast, both clusters move either upward or downward (**Fig. 3.5b**, **c**) when time-asymmetric reciprocal strokes are applied through the magnetic field (**Fig. 3.5bi**, **ci**). These clusters exhibit nonlinear displacement each time they execute a rapid (opening or closing) stroke. Their accumulated net displacement after several complete cycles (4 cycles for the 10-cube cluster; 16 cycles for the 4-cube cluster) of time-asymmetric flapping strokes is indicated by displaying two lines representing the initial (with solid line) and final (with dashed line) location of the central hinge (**Fig. 3.5bii&iii**, **3.5cii&iii**). Adjusting the relative speed between the opening and closing stroke through the applied magnetic fields in **Figure 3.5ai**, **bi**, **and ci** in a sequential manner allowed the 10-cube and 4-cube clusters to switch their active swimming modes among forward, backward and stationary motion. Below, we analyze these complex dynamic behaviors in the shear-thinning non-Newtonian fluid by focusing on one cluster with different types of time-asymmetric flapping patterns and two distinct clusters with the same type of time-asymmetric flapping pattern, separately.

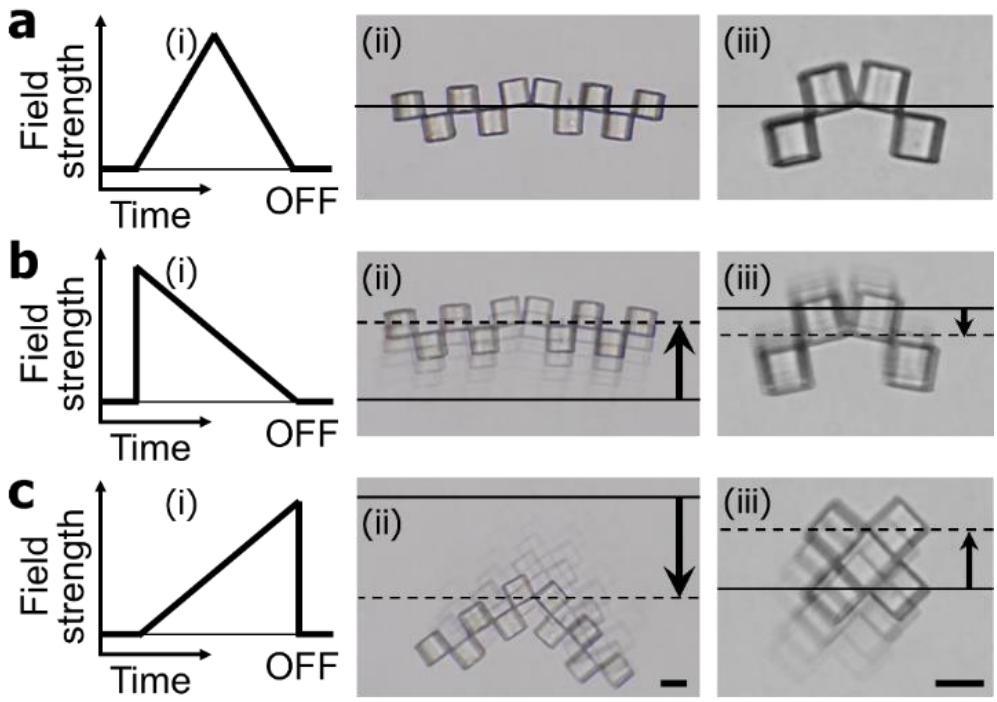

Figure 3.5: Directional active swimming modes of self-assembled microscallops. (**a**) No net displacement of a 10-cube cluster and a 4-cube cluster under a time-symmetric reciprocal actuation. The diagram in (**i**) depicts the change in the strength of the magnetic field for time-symmetric opening and closing strokes. Both the (**ii**) 10-cube and (**iii**) 4-cube clusters reveal no net displacement after 10 cycles of the time-symmetric stroke. (**b-c**) Net displacement of the 10-cube and 4-cube clusters under time-asymmetric reciprocal actuations: (**bi**) rapid opening & slow opening strokes; (**ci**) slow opening & rapid opening strokes. A snapshot of the 10-cube cluster overlaid with 5 frames at an interval of 1 sec. reveals the net (**bii**) upward and (**cii**) downward displacement under the applied magnetic field in (**bi**) and (**ci**), respectively. A snapshot of the 4-cube cluster overlaid with 5 frames at an interval of 4 sec. reveals the net (**biii**) downward and (**ciii**) upward displacement under the applied magnetic field in (**bi**) and (**ci**), respectively. Duty cycle of the signal in (**ai**), (**bi**), and (**ci**): 1 sec. Scale bar: 10 μm.

3.3.3 Effects of Time-Asymmetric Flapping Strokes on Swimming Dynamics

Figure 3.6 illustrates how time-symmetry change in the complete cycle of opening and closing strokes affects the net displacement of the 10-cube cluster. Given the relatively high aspect ratio of the 10-cube cluster (i.e., width:height=5:1), the cluster can be approximated in a simplified way as a body of long flapping arms with a single hinge (e.g., **Fig. 3.6aii**, **aiii**). This simplified model of the 10-cube cluster is geometrically similar to the previously reported model of macro scallop

made of brushless DC-motors and carbon fibre sheets.[24] On the basis of the interpretation of the macro scallop model, the mechanism of active swimming of the cluster with long flapping arms is schematically proposed in **Figure 3.6**. The key factor for the generation of net displacement is an instantaneous perturbation in the local viscosity distribution around the long cluster upon rapid opening or closing stroke. A rapid stroke represents the actuation speed needed to generate a high shear rate and to alter the viscosity of the surrounding shear-thinning fluid. To tune the shear rate of the moving arms, we vary the ratio of the relative speed between opening and closing stroke while keeping the same period time (**Fig. 3.6ai**, **bi**, **ci**). As a result of the flapling symmetry adjustment, we have time-asymmetric actuations with rapid opening (**Fig. 3.6bi**) or rapid closing (**Fig. 3.6ci**) strokes.

Under the time-symmetric actuation (**Fig. 3.6ai**), both opening and closing strokes generate a negligible local viscosity gradient because of their low shear rate (**Fig. 3.6aii**, **iii**). As a result of the lack of local viscosity gradient during the reciprocal flapping stroke, the cluster travels a similar distance downward and upward along y-axis, leading to no net displacement. In contrast, while the cluster is rapidly opening (**Fig. 3.6bii→iii**) or closing (**Fig. 3.6ciii→ii**), its moving arms exert a higher shear rate in the direction of the motion of the arms. This non-uniform shear creates a local viscosity gradient between the top (μ_L, low viscosity) and bottom (μ_H, high viscosity) regions of the cluster (**Fig. 3.6biii**, **cii**). Such an instantaneous local viscosity gradient by the rapid strokes enables viscophoretic non-linear displacement of the cluster. One complete cycle of such time-asymmetric reciprocal stroke (**Fig. 3.6b**, **c**) results in net displacement where the cluster self-migrates from the higher to lower viscosity site (**Fig. 3.6biii**, **cii**) during the rapid strokes, which we refer to as "self-viscophoresis."

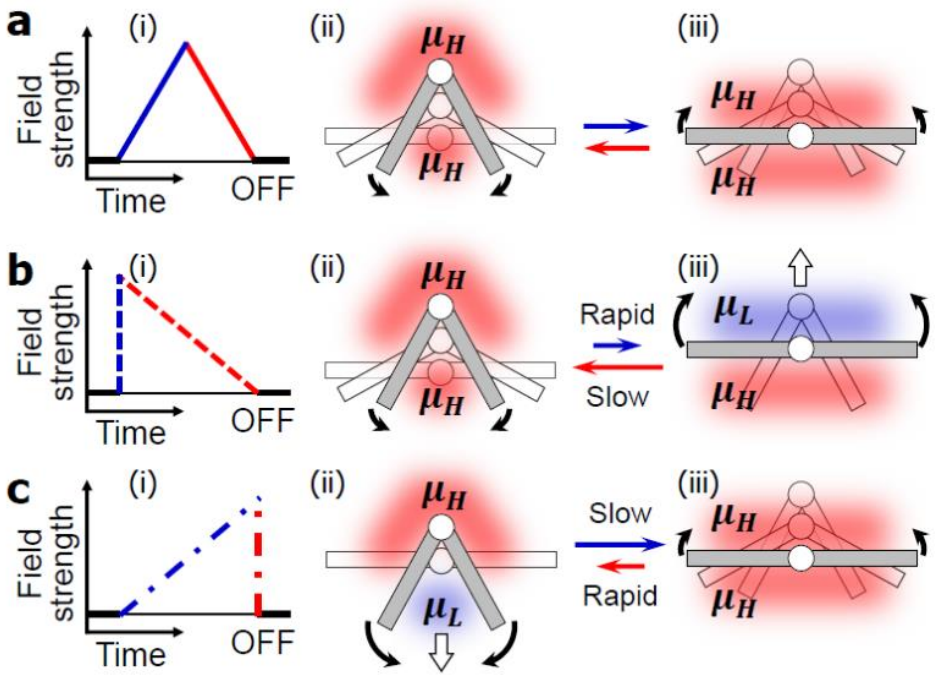

Figure 3.6: The effect of time-asymmetric strokes on the net displacement of a long cluster. (**a**) No net displacement of a cluster with long flapping arms because of lack of local viscosity gradient. The diagram in (**i**) depicts the change in the strength of a magnetic field for time-symmetric actuation. Schematic illustrations of the long cluster with a local viscosity distribution during the (**ii**) opening and (**iii**) closing stroke under the applied magnetic field in (**i**). (**b-c**) Net displacement of the cluster because of a local viscosity gradient induced by a rapid stroke. A diagram depicting the change in the strength of a magnetic field for time-asymmetric actuation: (**bi**) rapid opening & slow closing strokes; (**ci**) slow opening & rapid closing strokes. Schematic illustrations of the cluster with a local viscosity distribution: during the (**bii**) slow closing and (**biii**) rapid opening strokes under the applied magnetic field in (**bi**); during the (**cii**) rapid closing and (**ciii**) slow opening strokes under the applied magnetic field in (**ci**).

The net displacement of the cluster after each complete cycle of reciprocal opening and closing strokes is summarized in **Figure 3.7**. The cluster remains in place under the repeated time-symmetric flapping cycles (**Fig. 3.6ai**) and exhibits a continuous self-propulsion under repeated time-asymmetric flapping cycles (**Fig. 3.6bi**, **ci**). The cluster shows larger displacement by the rapid closing stoke than by rapid opening stroke. This observation can be attributed to a larger gradient of local viscosity incurred due to the higher shear rate imposed on the shear-thinning fluid sandwiched between the moving arms during the rapid stoke (**Fig. 3.6cii**).

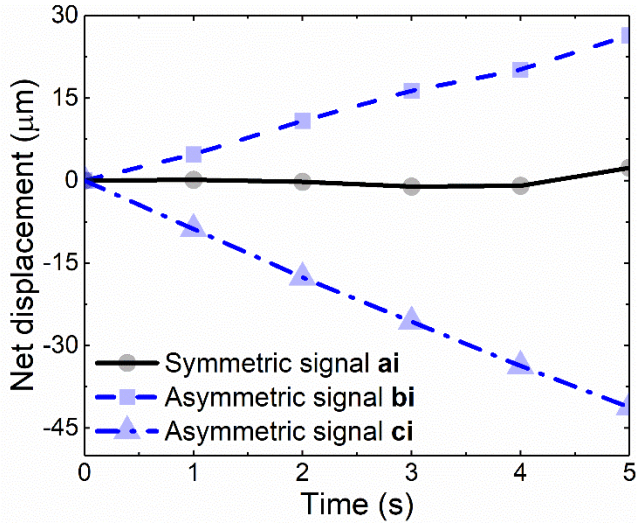

Figure 3.7: Tracking analysis on net displacement of the central hinge of the 10-cube cluster as a function of time for the applied signals in **Figure 3.6ai**, **bi** and **ci**. Duty cycle of the signal in (ai), (bi), and (ci): 1 sec.

3.3.4 Effects of Geometric Designs on Swimming Dynamics

One intriguing experimental observation is the dependence of swimming dynamics of self-assembled clusters on their geometric length and sequence. We compare the migration dynamics of a 4-cube and a 10-cube symmetric cluster and provide theoretical basis of the observed difference. Under the same type of time-asymmetric flapping cycles, the 4-cube and 10-cube clusters move in opposite directions to each other (**Fig. 3.5b**, **c**). In the case of the cycles of the slow opening and rapid closing stroke, along y-axis, the 4-cube self-propels upward while the 10-cube self-propels downward. Tracking analysis on the displacement of these clusters under one complete flapping cycle reveals that the opposite directions of nonlinear displacement arise during the rapid closing stroke (**Fig. 3.8**). Under the complete cycle of opening and closing strokes, the central hinge of both clusters swings downward and upward, respectively. The first half-cycle of the slow opening stroke leads to downward displacement of the clusters. During their upward displacement by the second half-cycle of the rapid closing stroke, the 4-cube and 10-cube cluster

move a longer and a shorter distance, respectively, than their own preceding downward displacement.

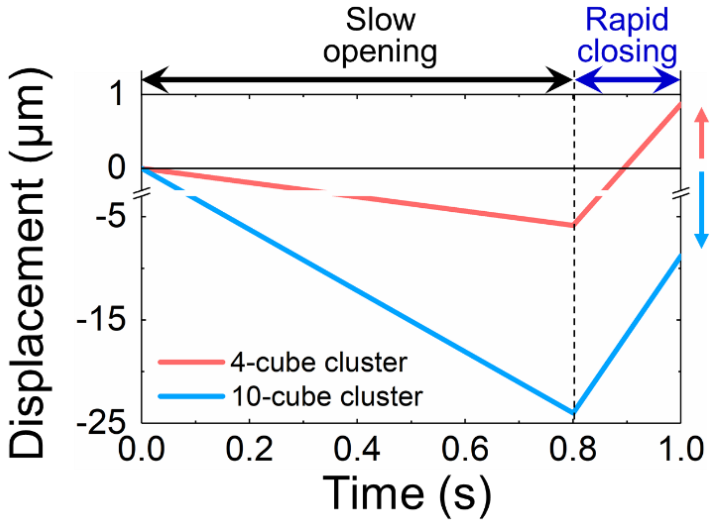

Figure 3.8: Tracking analysis on displacement of the central hinge of the 4-cube (light red) and 10-cube (light blue) clusters during the slow opening (0−0.8 s) followed by rapid closing (0.8−1.0 s) stroke. For both 4-cube and 10-cube clusters, the central hinge moves downward under the slow opening stroke and then upward under the followed rapid closing stroke while the 4-cube and 10-cube clusters show net upward and downward displacement, respectively.

We propose an explanation of this reversal of net swimming direction on the basis of a "coupled scallop" hypothesis. The complex geometry of these clusters can be conceptually simplified as if a top (white arms) and a bottom (grey arms) scallop are coupled in the clusters (the inset of **Fig. 3.9a** and **b**) and each scallop creates its own domain of fluid shear. Numerical simulation with the finite element method (via ANSYS®) was performed to investigate the local distribution of fluid shear around the clusters during their rapid closing stroke. To elucidate the concept of the "coupled scallop," we identify the formation of two discreate upper and lower domain around each cluster (**Fig. 3.9**). The larger integrated area of high shear rate over the rapid closing stroke out of the two domains represents higher energy dissipation. Such higher energy dissipation in the shear-thinning fluid gives rise to an effectively lower viscosity direction, where each cluster is directed to viscophorecially move toward.

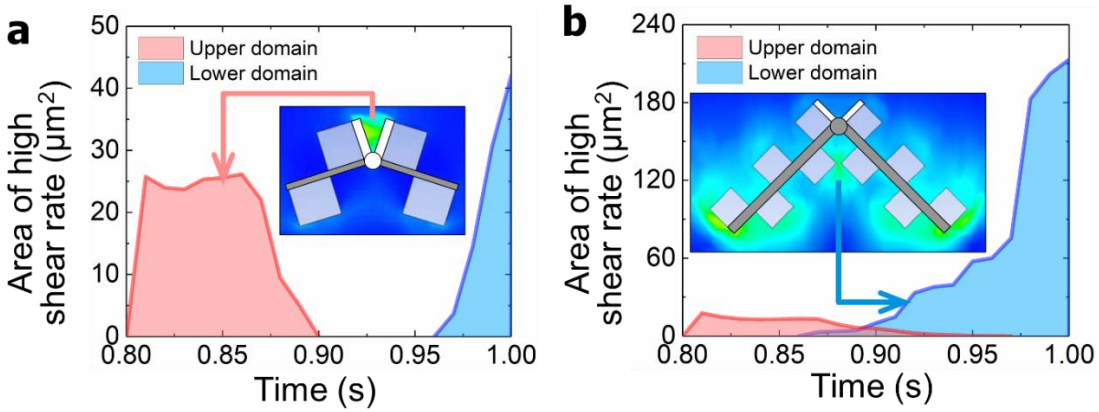

Figure 3.9: The effect of the cluster length on the direction of net displacement. (**a-b**) Integrated area of numerically simulated high shear rate region (> 30 s^{-1} calculated by ANSYS; represented by the green color in the insets) around the (**a**) 4-cube and (**b**) 10-cube clusters over the rapid closing stroke (0.8−1.0 s). As shown in the insets, a snapshot of ANSYS simulation reveals the generation of an instantaneous high shear rate (the green color) induced by the stroke. A top scallop and a bottom scallop are represented by white arms and grey arms, respectively, in the insets. These coupled scallops concurrently contribute to generate a high shear rate region where the top and bottom scallops are responsible for the upper (red line) and lower (blue line) domain of each cluster, respectively.

The upper high-shear domain is formed in-between two neighboring central cubes, acting as the top "scallop," by virtue of the geometry of an assembled cluster. It is important to take into account the effect of this domain in the case of the 4-cube cluster because the arms of its bottom scallop are too short to generate strong enough fluid shear in the region between the flapping arms, that is the lower domain. The comparison in the integrated area of the high shear rate region between the upper and lower domain of the 4-cube cluster reveals that its top scallop dissipates higher amount of energy than the bottom scallop and therefore guides the upward self-viscophoretic motion (**Fig. 3.9a**). We note that a bottom scallop grows with the addition of cubes while a top scallop maintains its size regardless of the number of cubes in an assembled cluster. As a result, in the case of the 10-cube cluster, the role of the top scallop becomes relatively smaller and the dominant bottom scallop leads to the downward self-viscophoretic motion (**Fig. 3.9b**).

Overall, these data present a remarkable case of correlation between geometric properties of micro-scaled colloidal assembly and viscous energy dissipation in non-Newtonian fluids leading to propulsion.

3.4 Conclusions

In summary, we report the dynamics of self-propulsion of a new class of microscopic swimmers. Taking advantage of a field-directed bottom-up assembly technique, we remotely assembled micron-size anisotropic cubes into scallop-like single-hinged microswimmers capable of periodic reciprocal strokes. Directional active swimming of these microscallops was achieved by locally modulating the viscosity of the surrounding non-Newtonian fluids through time-asymmetric flapping patterns. The self-propelling microswimmers could on-demand switch their swimming direction by simply reversing the time-asymmetry of the reciprocal flapping patterns and thus inverting the direction of the local viscosity gradient around the swimmers. In addition, the bottom-up approach also provided the flexibility of making microswimmers of different flapper lengths from different number of cubes as exemplified by the 4-cube and 10-cube clusters. We have confirmed that these two distinct clusters move in opposite directions to each other under the same type of time-asymmetric strokes, which reveals the critical influence of geometric designs on viscophoretic motility dynamics of the microswimmers.

We expect that by using more advanced building blocks, such self-assembled microswimmers could display more complex and more efficient swimming dynamics. Examples of such building blocks include anisotropic particles with different sizes, high aspect ratios, complex shapes and compositions.[29–31] One of the future directions of this research is making microswimmers from biocompatible or biodegradable materials for potential biological applications.[32,33] We believe the development of such self-assembled microswimmers could be a

step toward realizing synthetic microbots for in vivo biomedical applications. This would present an interesting case for the in-situ assembly and propulsion of microbots in biological media by taking specific advantage of the non-Newtonian rheological properties of such fluids.

3.5 Acknowledgements

We acknowledge Y. Lin for experimental assistance. This work was supported by the NSF Research Triangle MRSEC (DMR-1121107) and NSF grant CBET-1604116.

3.6 References

[1] B. J. Nelson, I. K. Kaliakatsos, J. J. Abbott. Microrobots for Minimally Invasive Medicine. *Annu. Rev. Biomed. Eng.* **2010**, *12*, 55.

[2] J. Wang, W. Gao. Nano/Microscale Motors: Biomedical Opportunities and Challenges. *ACS Nano* **2012**, *6*, 5745.

[3] X. Lin, Z. Wu, Y. Wu, M. Xuan, Q. He. Self-Propelled Micro-/Nanomotors Based on Controlled Assembled Architectures. *Adv. Mater.* **2016**, *28*, 1060.

[4] V. Magdanz, M. Medina-Sánchez, L. Schwarz, H. Xu, J. Elgeti, O. G. Schmidt. Spermatozoa as Functional Components of Robotic Microswimmers. *Adv. Mater.* **2017**, *29*, 1606301.

[5] X. Z. Chen, B. Jang, D. Ahmed, C. Hu, C. De Marco, M. Hoop, F. Mushtaq, B. J. Nelson, S. Pané. Small-Scale Machines Driven by External Power Sources. *Adv. Mater.* **2018**, *30*, 1705061.

[6] J. J. Abbott, K. E. Peyer, M. C. Lagomarsino, I. K. Kaliakatsos, B. J. Nelson. How Should Microrobots Swim? *Int. J. Rob. Res.* **2009**, *28*, 1434.

[7] P. Fischer, A. Ghosh. Magnetically Actuated Propulsion at Low Reynolds Numbers : Towards Nanoscale Control. *Nanoscale* **2011**, *3*, 557.

[8] D. Du, E. Hilou, S. L. Biswal. Reconfigurable Paramagnetic Microswimmers: Brownian Motion Affects Non-Reciprocal Actuation. *Soft Matter* **2018**, *14*, 3463.

[9] E. M. Purcell. Life at Low Reynolds Number. *Am. J. Phys.* **1977**, *45*, 3.

[10] E. Lauga, T. R. Powers. The Hydrodynamics of Swimming Microorganisms. *Reports Prog. Phys.* **2009**, *72*, 96601.

[11] C. Bechinger, R. Di Leonardo, C. Reichhardt, G. Volpe. Active Particles in Complex and Crowded Environments. *Rev. Mod. Phys.* **2016**, *88*, 045006.

[12] T. Xu, W. Gao, L. Xu, X. Zhang, S. Wang. Fuel-Free Synthetic Micro-/Nanomachines. *Adv. Mater.* **2017**, *29*, 1603250.

[13] A. Ghosh, P. Fischer. Controlled Propulsion of Artificial Magnetic Nanostructured Propellers. *Nano Lett.* **2009**, *9*, 2243.

[14] L. Zhang, J. J. Abbott, L. Dong, B. E. Kratochvil, D. Bell, B. J. Nelson. Artificial Bacterial Flagella: Fabrication and Magnetic Control. *Appl. Phys. Lett.* **2009**, *94*, 64107.

[15] R. Dreyfus, J. Baudry, M. L. Roper, M. Fermigier, H. A. Stone, J. Bibette. Microscopic Artificial Swimmers. *Nature* **2005**, *437*, 862.

[16] K. E. Peyer, S. Tottori, F. Qiu, L. Zhang, B. J. Nelson. Magnetic Helical Micromachines. *Chem. Eur. J.* **2013**, *19*, 28.

[17] X. Chen, M. Hoop, F. Mushtaq, E. Siringil, C. Hu, B. J. Nelson, S. Pané. Recent Developments in Magnetically Driven Micro- and Nanorobots. *Appl. Mater. Today* **2017**, *9*, 37.

[18] R. W. Carlsen, M. Sitti. Bio-Hybrid Cell-Based Actuators for Microsystems. *Small* **2014**, *10*, 3831.

[19] M. Guix, J. Orozco, M. García, W. Gao, S. Sattayasamitsathit, A. Merkoçi, A. Escarpa, J. Wang. Superhydrophobic Alkanethiol-Coated Microsubmarines for Effective Removal of Oil. *ACS Nano* **2012**, *6*, 4445.

[20] J. Li, B. Esteban-Fernández de Ávila, W. Gao, L. Zhang, J. Wang. Micro/nanorobots for Biomedicine: Delivery, Surgery, Sensing, and Detoxification. *Sci. Robot.* **2017**, *2*, eaam6431.

[21] J. Li, O. E. Shklyaev, T. Li, W. Liu, H. Shum, I. Rozen, A. C. Balazs, J. Wang. Self-Propelled Nanomotors Autonomously Seek and Repair Cracks. *Nano Lett.* **2015**, *15*, 7077.

[22] D. A. Gagnon, N. C. Keim, P. E. Arratia. Undulatory Swimming in Shear-Thinning Fluids: Experiments with Caenorhabditis Elegans. *J. Fluid Mech.* **2014**, *758*, R3.

[23] J. Park, D. Kim, J. H. Shin, D. A. Weitz. Efficient Nematode Swimming in a Shear Thinning Colloidal Suspension. *Soft Matter* **2016**, *12*, 1892.

[24] T. Qiu, T.-C. Lee, A. G. Mark, K. I. Morozov, R. Münster, O. Mierka, S. Turek, A. M. Leshansky, P. Fischer. Swimming by Reciprocal Motion at Low Reynolds Number. *Nat. Commun.* **2014**, *5*, 5119.

[25] K. Han, C. W. Shields IV, N. M. Diwakar, B. Bharti, G. P. López, O. D. Velev. Sequence-Encoded Colloidal Origami and Microbot Assemblies from Patchy Magnetic Cubes. *Sci. Adv.* **2017**, *3*, e1701108.

[26] C. W. Shields IV, S. Zhu, Y. Yang, B. Bharti, J. Liu, B. B. Yellen, O. D. Velev, G. P. López. Field-Directed Assembly of Patchy Anisotropic Microparticles with Defined Shape. *Soft Matter* **2013**, *9*, 9219.

[27] S. K. Smoukov, S. Gangwal, O. D. Velev. Reconfigurable Responsive Structures Assembled from Magnetic Janus Particles. *Soft Matter* **2009**, *5*, 1285.

[28] R. B. Bird, C. F. Curtiss, R. C. Armstrong, O. Hassager. *Dynamics of Polymeric Liquids, Volume 1: Fluid Mechanics*, 2nd ed.; Wiley: New York, 1987.

[29] Z. Zhang, S. C. Glotzer. Self-Assembly of Patchy Particles. *Nano Lett.* **2004**, *4*, 1407.

[30] S. C. Glotzer, M. J. Solomon. Anisotropy of Building Blocks and Their Assembly into Complex Structures. *Nat. Mater.* **2007**, *6*, 557.

[31] A. Walther, A. H. E. Müller. Janus Particles: Synthesis, Self-Assembly, Physical Properties, and Applications. *Chem. Rev.* **2013**, *113*, 5194.

[32] M. Guix, C. C. Mayorga-martinez, A. Merkoçi. Nano/Micromotors in (Bio)chemical Science Applications. *Chem. Rev.* **2014**, *114*, 6285.

[33] W. Gao, R. Dong, S. Thamphiwatana, J. Li, W. Gao, L. Zhang, J. Wang. Artificial Micromotors in the Mouse's Stomach: A Step toward in Vivo Use of Synthetic Motors. *ACS Nano* **2015**, *9*, 117.

Chapter 4

Active Rotation of Engineered Particles Powered by AC Electric Fields*

* Partially based on Shields IV, Han, and Velev *et al*., accepted in *Adv. Funct. Mater*.

4.1 Introduction

Active particles have emerged as a topic of scientific interest due to their ability to convert energy from their environment into autonomous propulsion.[1–3] The underlying mechanism driving their motion is encoded in their design, as they asymmetrically draw and dissipate energy, thus creating local gradients of force for propulsion.[4] Active particles are heralded for having promise in applications such as remote surgery, self-repairing systems, and self-motile devices.[5] Yet, most examples developed insofar (e.g., those powered by acoustic,[6] electric,[7] magnetic,[8–11] and optical fields[12–14]) are simple in nature, typically translating in a single direction. Some work has also been done to develop active spinners that rotate about a central axis.[15–17] Due to their more sophisticated motions, these particles may be used as constituents in systems with switchable phase transition behaviors and interlocking microgears in colloidal micromachines, for example.[18,19] However, further progress must be made to achieve these goals, by engineering particles with controlled size and shape to respond to stimuli and subsequently switch their direction of rotation in a controlled manner.

Electric fields are a facile source for powering the motion of active particles, as they enable the precise tuning of the induced propulsion forces on particles in real time (and thus particle motion) and provide a means by which to tune particle-particle interactions.[20] Furthermore, simple changes in the frequency of applied electric fields can give rise to a number of distinct electrokinetic effects that can power locomotion in different ways. For example, it has been shown that active particles can undergo movement by electrohydrodynamic (EHD) flows,[21] induced charge electrophoresis (ICEP),[22] self-dielectrophoresis (sDEP),[23] and self-electrophoresis by diode rectification.[24–26] By rationally designing particles to respond to AC electric fields by

several of these mechanisms at different frequencies, it is possible to create particles that can multimodally change their direction of motion on demand.

We have developed a supercolloidal microspinner that harvests AC electrical energy for dissipation by four phenomenological modes to enable switchable rotation on demand. The microspinners are fabricated with three bent arms, each displaying metallic patches deposited along their distal ends (**Fig. 4.1a**). After fabrication, we studied their responses to stimulation by an external AC electric field in a transparent experimental chamber, where the particles were confined in a thin gap between two parallel glass slides coated with indium tin oxide (see Methods; 4.2.2). Due to their asymmetric shape and complex metallization, the microspinners evoke multiple electrokinetic mechanisms that are a function of the applied electric field frequency. We found that, as the electric field frequency increases (e.g., 0.1 to 500 kHz), the particles invert their spin direction at three crossover frequencies (**Fig. 4.1b**). Below, we first describe in detail the phenomenological behavior of this system of sophisticated spinners and analyze the foundations of the mechanisms involved through experimental evaluation and simple scaling arguments.

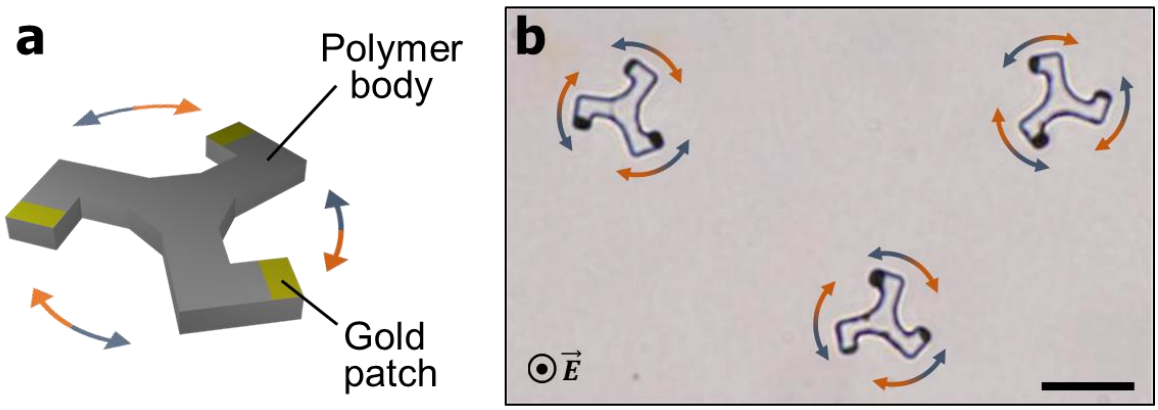

Figure 4.1: Electrically switchable rotation of supercolloidal spinners. (**a**) Schematic illustration of a particle microspinner consisting of a transparent polymer body (shown in gray) and a gold patch along the distal end of each of its three arms. (**b**) Micrograph of three particle spinners rotating in a vertical electric field (right). Note: the orientation of the spinner in (**a**) is flipped and mirrored; the correct chirality is shown in (**b**), whereby the metallic patches face downward. Scale bar: 25 μm.

4.2 Materials and Methods

4.2.1 Particle Fabrication

Patchy microspinners were fabricated using standard photolithography and metal deposition techniques as shown in **Figure 4.2**. First, SU-8 2002 photoresist (MicroChem, Corp.) was spin-coated on a 3" single-side polished silicon (Si) wafer (Addison Engineering, Inc.) to a thickness of 2 μm and exposed to UV light (365 nm, MA/BA6 Mask Aligner, Süss MicroTec AG) through a chrome-patterned photomask (**Fig. 4.2a**) to form the microspinners, which were revealed after development of the photoresist (following the procedures by MicroChem; **Fig. 4.2b-c**). Second, the wafers were spin-coated with two layers of NFR-014R photoresist (JSR Micro, Inc.) to reach a thickness of 6 μm and exposed to UV light (365 nm, MA/BA6 Mask Aligner, Süss MicroTec AG) through an aligned chrome-patterned photomask consisting of an array of 2 x 4 μm^2 rectangular patches that aligned with the distal ends of each arm of the microspinner; Photo Sciences, Inc.) to form exposed regions along the distal ends of the arms of each microspinner. The wafer was then mounted inside of an electron beam metal evaporator (Solution E-Beam, CHA Industries, Inc.) to allow for the deposition of 10 nm of Cr followed by 100 nm of Au on the topside of the wafer (**Fig. 4.2d**). The NSF-014R photoresist was separated from the SU-8 2002 photoresist by submerging the wafers in acetone at ambient temperature for 10 min. Wafers were then removed, rinsed with a steady stream of acetone followed by methanol, re-submerged in a clean bath of acetone for an additional 30 sec, and rinsed again as described above. Wafers were then dried with a stream of nitrogen gas. Particles were then wetted with Remover PG (MicroChem) and removed via shear forces from a pressed-steel razor blade. Note: the non-patchy microspinners were made by following the first step (shown in **Fig. 4.2a-b**) and extracting the particles directly from the Si wafers (**Fig. 4.2c**).

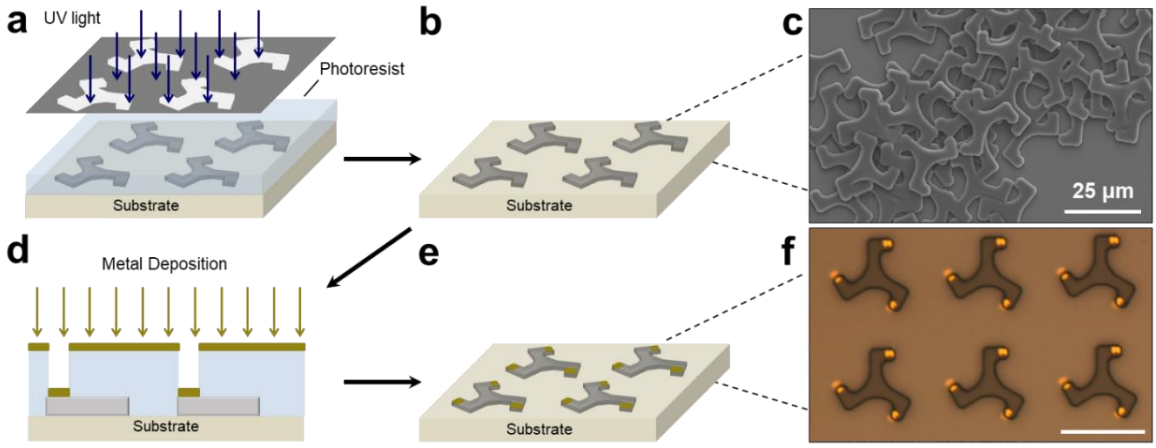

Figure 4.2: Microspinner fabrication. (**a**) UV light selectively exposes spin-coated photoresist through a patterned photomask. (**b**) Particles are obtained after washing off uncross-linked photoresist. (**c**) A scanning electron microscope (SEM) image of anisotropically shaped particles after their removal from the substrate. (**d**) While still on the wafer, the formed particles can be coated with a second layer of photoresist, where alignment photolithography is used to create exposed regions along the tops of the particles in discrete regions for metal deposition. (**e**) Particles with metallic patches are recovered by removal of the second layer of photoresist. (**f**) A SEM image of the anisotropic patchy particles before removal from the substrate.

4.2.2 Experimental Setup

A small volume particle suspension was sandwiched between two parallel glass slides coated with ITO (Sigma-Aldrich), which were separated by a 100-µm thick insulating spacer made from polyester (McMaster-Carr; **Fig. 4.3**). The external AC field was applied perpendicularly to the ITO surfaces. Before assembling the experimental cell, the microspinners were diluted 10-fold in DI water and washed with DI water at least thrice (i.e., centrifuged at 2,000xG for 3 min and re-suspended in an equal volume of DI water). Prior to use, the ITO-coated glass slides were rinsed with successive streams of acetone, isopropyl alcohol, and DI water and were wiped with a Calgiswab (QuickMedical) after each rinsing step. Once the experimental cell was assembled, strips of copper tape were connected to each ITO-coated glass slide. An alternating current electric field was applied across the ITO-coated glass slides via the copper tape using a function generator (33120A, Agilent Technologies, Inc.). All experiments were performed under an upright optical

microscope (BX61, Olympus), where the objective was placed directly above the slides, and videos were recorded using a charge-coupled device camera (DP70, Olympus) at 15 frames per second.

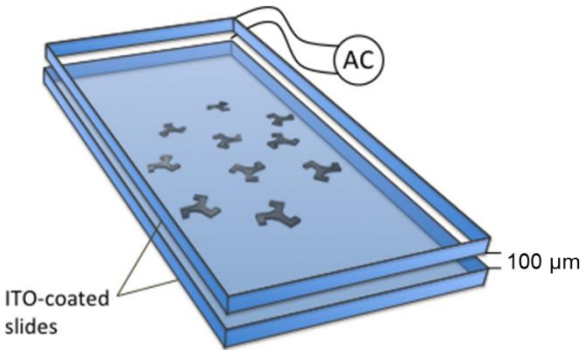

Figure 4.3: Schematic of the experimental setup used to investigate the rotation of the spinners, powered by a vertical AC electric field between the ITO-coated slides.

4.2.3 Ionic Content of Deionized Water Exposed to the Atmosphere

The deionized (DI) water (purified by Milli-Q; Millipore) had $\sigma_w = 4 \cdot 10^{-5}\, S/m$ and $pH \approx 5.6$. We presume that the increased conductivity is the result of dissolved atmospheric CO_2 forming carbonic acid, which dissociates to bicarbonate (HCO_3^-) and carbonate (CO_3^{-2}) ions, depending on the pH of the solution.[27] Recognizing that the former is found in higher concentrations, the electrolyte can be approximated as a binary symmetric electrolyte with the hydronium (H_3O^+) and bicarbonate (HCO_3^-) as the dominating cations and anions, respectively. To simplify our analysis, we approximated the solution as a binary electrolyte by calculating an average diffusivity $D = \left(D_{H_3O^+} + D_{HCO_3^-}\right)\Big/2 \approx 5.3 \cdot 10^{-9}\, m^2/s$, where $\left(D_{H_3O^+} = 9.3 \cdot 10^{-9}\, m^2/s\right)$ and $\left(D_{HCO_3^-} = 1.2 \cdot 10^{-9}\, m^2/s\right)$ are the diffusivities of H_3O^+ and HCO_3^-, respectively. Evaluating the ionic concentration, $c_0 \approx 2.5 \mu M$, from the measured *pH* of 5.6, the calculated conductivity can be

approximated as $\sigma_w = \frac{2F^2 z^2 c_0}{RT}\left(\frac{D_{H_3O^+} + D_{HCO_3^-}}{2}\right) = \frac{2F^2 z^2 c_0 D}{RT} \sim 10^{-4}\, S/m$, which is on the order of the measured conductivity, $\sigma_w = 4 \cdot 10^{-5}\, S/m$.

4.3 Results and discussion

4.3.1 Electrokinetic Rotation of Non-Patchy Microspinners

As a control, we first studied the rotation of non-patchy, dielectric microspinners made solely of SU-8 polymer (**Fig. 4.4**). The microspinners rotated clockwise at low frequencies (i.e., <3 kHz), and reversed their direction of rotation at higher frequencies. The angular speeds of the microspinners were comparatively high in the clockwise (or low frequency) regime compared to the anti-clockwise regime (e.g., 137.3 deg/sec at 0.1 kHz and 2.5 deg/sec at ~10 kHz).

Broadly speaking, the mechanisms responsible for electrokinetic rotation of a spinning particle arise from asymmetry in its geometry or polarizability.[28] In the case of the non-patchy microspinners, only geometric effects are present, suggesting that the rotation is driven by EHD flows. In the case of a simple homogeneous sphere, EHD flows are symmetrically balanced around the particle, and no movement occurs. However, when the geometric symmetry of a particle is broken, EHD flows become imbalanced, thus leading to active motion. This concept was first demonstrated by Ma *et al*. using asymmetric colloidal dimers, where the authors also observed a directional transition in the movement of the particles around 3 kHz.[29]

The angular speed of the microspinners increased with the square of the electric field strength (e.g., at 2 kHz; **Fig. 4.4a**). The quadratic scaling of the angular speed with the electric field along with its rapid frequency dispersion beyond the approximated $f_{EHD} = \frac{D}{2\pi\lambda_D H} \sim 87 Hz$ confirms that the underlying mechanism of the rotation of the non-patchy microspinners is EHD

flows,[30] which result from AC electroosmosis (ACEO) on the electrodes and the broken symmetry of the microspinner. Whenever a suspended particle is subjected to an electric field at low frequencies, liquid flows (i.e., EHD flows) are driven around the particle due to the movement of excess ions within the induced electric double layer (EDL) in response to the applied field. Herein, $D \approx 5.3 \cdot 10^{-9}\, m^2/s$ is the effective diffusion coefficient, $\lambda_D = \sqrt{\varepsilon_w RT/2F^2 z^2 c_0} \sim 194nm$ is the Debye length, and $2H = 100\mu m$ is the spacing between the electrodes (**Fig. 4.3**). Also, $\varepsilon_w \approx 80\varepsilon_0$ is the permittivity of the DI water, ε_0 is the permittivity of a vacuum, R is the gas constant, T is the absolute temperature, F the Faraday constant, z the ionic valence, and $c_0 \approx 2.5\mu M$ is the concentration approximated from the measured pH value of 5.6.

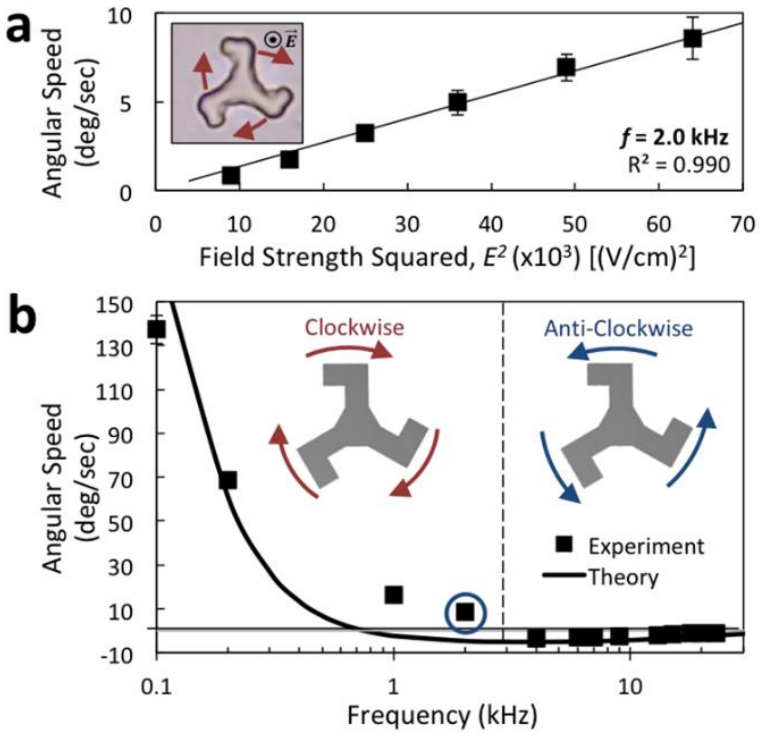

Figure 4.4: Rotation dynamics data for non-patchy polymer microspinners. (**a**) Angular speed of non-patchy microspinners as a function of E^2 at 2.0 kHz; positive values indicate clockwise rotation. (**b**) Angular speed of non-patchy microspinners as a function of frequency in an orthogonal electric field (E^2 = 6.4x10^5 V^2/cm^2). (**c**) Two non-patchy microspinners lock at low field strengths (E^2 = 1.6x10^4 V^2/cm^2) and at 2 kHz. Microspinners disassemble and separately rotate at high electric field strengths (E^2 = 6.4x10^5 V^2/cm^2).

Due to the complexity of the microspinner geometry, one cannot easily obtain an accurate quantitative description of the EHD flows. However, in order to provide a qualitative description of the particle behavior, we build upon the relations obtained for simpler particles, either a dimer[29] or a Janus Particle (JP).[22] Here, we study particles consisting of three identical structures with 120º between their arms that, unless connected so as to perform pure rotational motion, would translate away from each other linearly. According to Eqn. (3) in the article by Ma *et al.*,[21] the EHD flow velocity is expected to scale as:

$$\dot{\theta}_{EHD}\left(\bar{\Omega}\right) \propto \frac{K' + \bar{\Omega}K''}{1+\bar{\Omega}^2} \qquad \textbf{(Equation 4.1)}$$

wherein $\bar{\Omega} = \omega\lambda_D H/D$ ($\omega = 2\pi f$) and K' and K'' are the real and imaginary parts of the polarization coefficient, $\underline{K}\left(\omega\right) = \left(\frac{\sigma_p - \sigma_w}{\sigma_p + 2\sigma_w}\right)\left[\frac{j\omega\tau_0 + 1}{j\omega\tau_{MW} + 1}\right]$ (also termed the Clausius–Mossotti factor; $\tau_{MW} = \left(\frac{\varepsilon_p + 2\varepsilon_w}{\sigma_p + 2\sigma_w}\right)$, $\tau_0 = \left(\frac{\varepsilon_p - \varepsilon_w}{\sigma_p - \sigma_w}\right)$, $j = \sqrt{-1}$, $\varepsilon_p = 2.55\varepsilon_0$ is the particle permittivity and σ_p is the particle effective bulk conductivity used as a fitting parameter along with the pre-factor of **Equation 4.1**). Using the particle effective bulk conductivity, σ_p ($\sim 1\mu S/cm$), and the pre-factor of 1,100 from **Equation 4.1** as fitting parameters, one can obtain an estimate of the EHD reversal frequency (i.e., ~ 1 kHz), which is in qualitative agreement with the experimental results (**Fig. 4.4b**). Although being of the same order of magnitude, the quantitative difference between the fitted reversal frequency and the experimental value (~ 3 kHz) is probably due to the inability to perfectly match the model obtained for a dimer particle and the much more complicated particle tested. In particular, the reversal at ~ 3 kHz resembles the effect described in Ma *et al.*[21] for a cluster of two different sized particles made of the same dielectric material.

Given the ability of the non-patchy microspinners to controllably switch directions based upon the frequency of the applied field, we sought to demonstrate that microspinners can lock (assemble) and unlock (disassemble) on demand. Such controlled locking and unlocking could prove useful for a variety of systems (e.g., for studying phase transitions, as hypothesized by Glotzer and co-workers[18,19]). At low field strengths (i.e., corresponding to E^2 = 1.6x10^4 V^2/cm^2), we found that the attractive EHD flows between the microspinners drove their assembly into doublets (**Fig. 4.5**). However, at high field strengths (e.g., corresponding to E^2 = 6.4×10^5 V^2/cm^2) at the same frequency (i.e., 2 kHz), larger EHD flows in the same direction led to instability between the particles and stronger dipolar repulsion, which made the microspinners disassemble and rotate separately. While this example only shows the interactions between two microspinners for the sake of simplicity, it demonstrates how minor adjustments in an applied electric field can serve as a convenient tool to control particle-particle interactions.

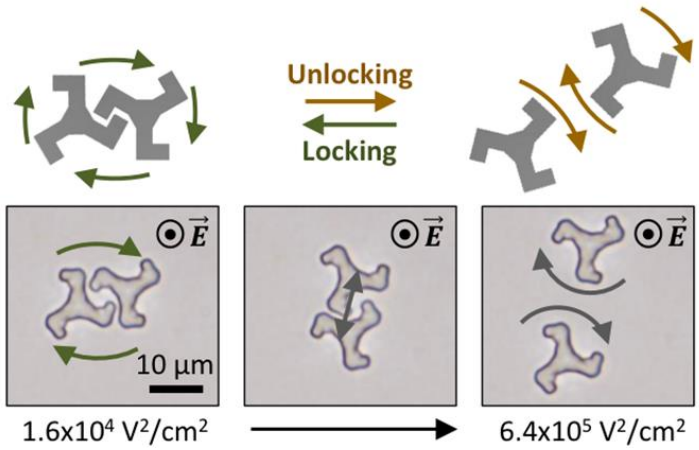

Figure 4.5: Locking and unlocking behaviors of two non-patchy microspinners. The microspinners lock at low field strengths (E^2 = 1.6x10^4 V^2/cm^2) and at 2 kHz. Microspinners disassemble and separately rotate at high electric field strengths (E^2 = 6.4x10^5 V^2/cm^2).

4.3.2 Electrokinetic Rotation of Patchy Microspinners

The addition of gold patches along the tips of each arm of the microspinner enables two additional rotational inversions at high frequencies where the primary mechanisms driving such frequency-

dependent rotation are summarized in **Figure 4.6**. The phenomenological transitions in the spin direction are attributed to sequential transition of these mechanisms (from left to right, in order of increasing electric field frequency). Similar to the non-patchy microspinners, the asymmetric shape of the patchy microspinners facilitates generating imbalanced EHD flows where the first rotational inversion occurs due to a reversal in EHD flows. The asymmetric polarization between the dielectric body and the gold patches of the patchy microspinners induces additional rotational modes by ICEP[31–33] and sDEP,[23] which will be discussed in more detail below. Briefly, as the frequency increases further after the first rotational inversion, the transition of motion mechanism from reserved EHD flows to ICEP leads to the second rotational inversion. As the frequency increases further still (i.e., to ~50 kHz), sDEP becomes dominant over ICEP leading to the final rotational inversion.[23]

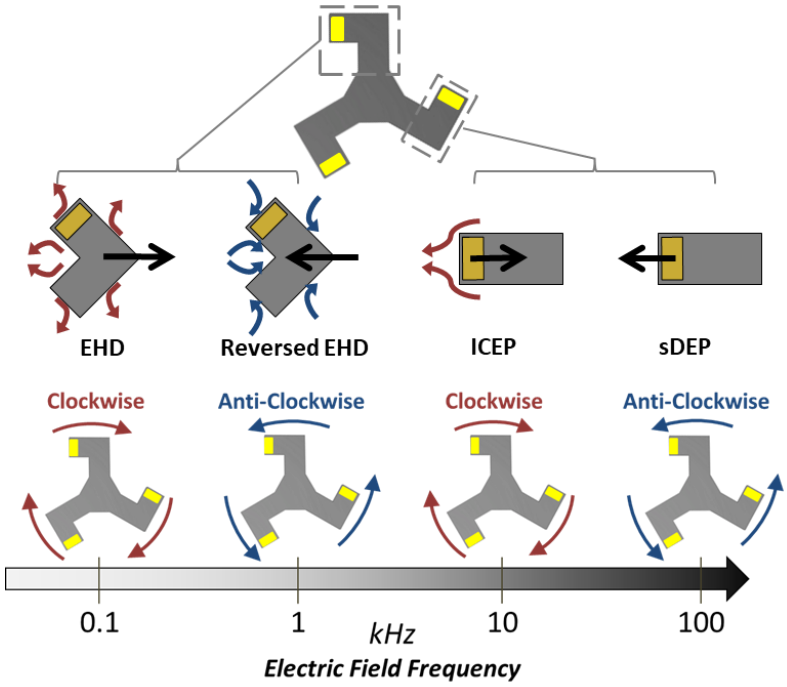

Figure 4.6: Schematic of the effect of the electric field frequency on the direction of particle rotation, where the direction of motion of each particle section is indicated with a black arrow; flow lines (blue and red) are hypothesized. Thus, particle spinners display four modes of rotation, whereby motion occurs due to (in order of increasing frequency): EHD flows, reversed EHD flows, ICEP, and sDEP.

To understand the effects of the asymmetric polarization on particle spin behavior, it is best to first consider the simple case of metallodielectric JP spheres, where one hemisphere is conductive and the other is dielectric. We first investigated the rotational mode by ICEP. It has been shown that the unbalanced induced charge electroosmotic (ICEO) flows generated due to the asymmetric polarization of the JPs lead to their linear translation.[22] Connecting three such JPs approximately resembles the microspinners shown here. This concept was originally suggested by Squires and Bazant, but was never experimentally tested or verified.[34] The first realization of an electrokinetic spinner consisting of two JPs (i.e., a doublet) was achieved by Boymelgreen *et al.*,[35] where the relative orientation of the metallodielectric interface dictated the orbital motion of the doublet.

The conductive surface patches on the microspinners result in the induction of a different electro-convective mechanism at frequencies higher than those corresponding to EHD, which are rapidly suppressed with increasing frequencies (i.e., beyond the resistor-capacitor (RC) time of the induced charge on the powered electrodes). The maximum ICEO response corresponding to the RC time of the induced charges at the metallic patches can be approximated as $f_{ICEP} = \frac{D}{2\pi\lambda_D a} = \frac{f_{EHD}H}{a} \sim 2.7kHz$, where $a \approx 1.6\mu m$,[32,34,36] which is the approximate effective radius of the Au patch (corresponding to the in-plane Au-coated region of 4 μm width and 2 μm length, i.e., $\pi a^2 = 4\mu m \cdot 2\mu m$).

Since the metallic patches are placed at the distal ends of the arms of the microspinners, the ICEO flows should cause the particles to spin in a clockwise direction in the ICEP regime. Indeed, after increasing the frequency (i.e., to ~3 kHz), the microspinners begin to rotate clockwise again (**Fig. 4.7**). In this case, when an electric field is applied across a cell containing the microspinners, they become polarized, whereupon a layer of countercharges accumulates against

the surfaces of the particles in the EDL. Since the surfaces of the microspinners have an asymmetric distribution of polarizability, the EDLs over the metal patches of the microspinners are more strongly polarized than the dielectric bodies of the particles. This results in imbalanced ICEO flows, which cause the spinners to rotate via ICEP.

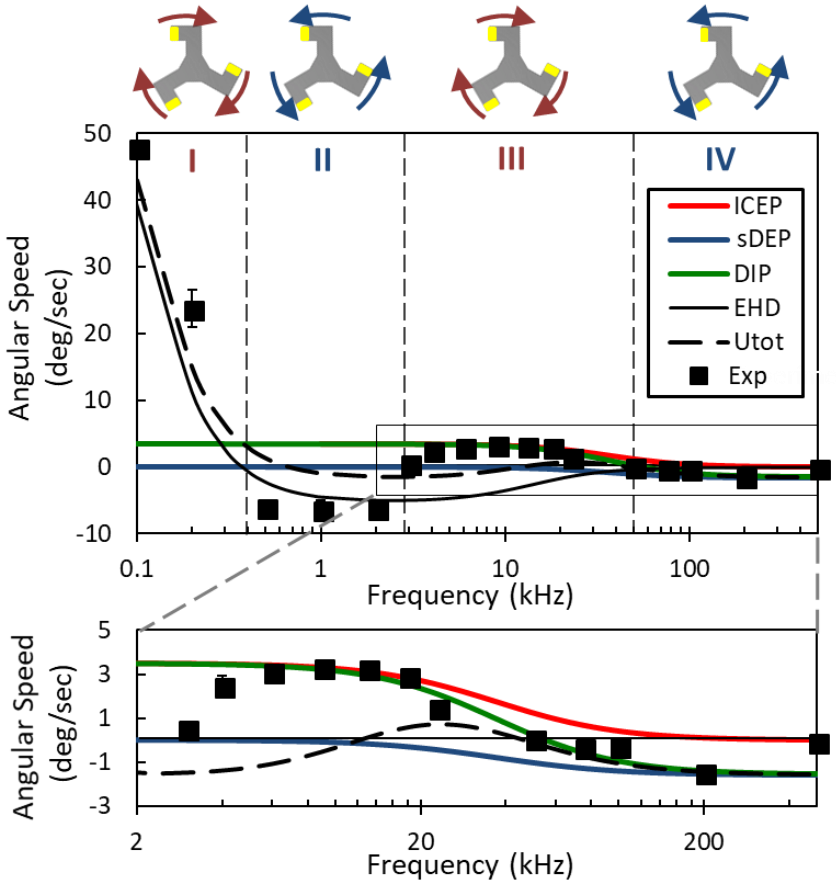

Figure 4.7: Rotation dynamics of patchy metallodielectric microspinners. [**Top**] Schematics display the direction of particle rotation (clockwise and anti-clockwise rotations are indicated by red and blue arrows, respectively). [**Middle**] Angular speed of patchy microspinners as a function of electric field frequency (at a constant E^2 = 6.4x10^5 V^2/cm^2); positive values indicate clockwise rotation. Theoretical trend lines are fitted to the experimental results (symbols) with Eqn. (1) for EHD (solid black line), Eqn. (2) for ICEP (red line), and Eqn. (3) for sDEP (blue line). The dipolophoresis (DIP) angular velocity (green line) is obtained by summing the ICEP and sDEP contributions, while the total angular speed (black dashed line) is obtained by the sum of the DIP and EHD contributions. [**Bottom**] Expanded view of the graph above, displaying values between 2 and 500 kHz.

Despite the quantitative differences between the fitted model and the experimental data, both exhibit the three reversal frequencies (i.e., $f_{EHD\rightarrow rEHD}$, $f_{rEHD\rightarrow ICEP}$, $f_{ICEP\rightarrow sDEP}$). From **Figure 4.7**, we see that in the low frequency range (i.e., 0.1 to ~3 kHz), the patchy microspinners behave similarly to the non-patchy microspinners (i.e., their rotations are dominated by EHD flows, yet with a lower EHD reversal frequency of ~0.3 kHz). Here, we obtained a fitted effective particle bulk conductivity, σ_p, of $\sim 0.5 \mu S/cm$ and pre-factor of 1,500 in **Equation 4.1**. In contrast to the non-patchy microspinners, a second reversal in the direction of rotation occurs at ~3 kHz. It is assumed that this reversal is associated with the transition from EHD flows to ICEP, as the reversal frequency (i.e., $f_{EHD\rightarrow ICEP} \sim 3kHz$) is in agreement with the maximum ICEP response,[31,32,34,36] matching the RC time of the induced charges at the metallic patch (i.e., $f_{ICEP} \sim 2.7kHz$) and the diminishing EHD flows.

At even higher frequencies (i.e., > 50 kHz), a third and final spin reversal occurs, which is associated with the transition from ICEP to sDEP,[23] $f_{ICEP\rightarrow sDEP} \sim 60kHz$. sDEP occurs due to the presence of strong, localized field gradients between the conductive surface patches on the microspinners and the adjacent conductive substrate (i.e., the ITO-coated glass slides).[23] More specifically, sDEP results from the localized, asymmetric non-uniform electric field induced by the dual asymmetry of the particle and the electrode that act on the induced dipole within the particle.[23] Since such asymmetry exists also at frequencies well beyond the RC time of the ICEO of such particles, it is expected the sDEP contribution dominates at high frequencies where electro-convection effects are negligible. In the case of a simple JP, the result is that the particle propels with the gold-coated hemisphere facing forward (i.e., opposite to the motion of ICEP), and in the case of the microspinners, the result is that the particles rotate with the gold tips facing forward (i.e., anti-clockwise).

Following Boymelgreen *et al.* for moderate frequencies,[23] below the Maxwell-Wagner limit, i.e., $\Omega_{MW} = \frac{\omega\lambda_D^2}{D} << 1$, the non-dimensional expressions for the ICEP and sDEP angular velocities can be simplified to:

$$\dot{\theta}_{ICEP}(\Omega) \propto \frac{B}{B^2 + (A\Omega)^2} \quad \textbf{(Equation 4.2)}$$

$$\dot{\theta}_{sDEP}(\Omega) \propto -\frac{\Omega^2}{B^2 + (A\Omega)^2} \quad \textbf{(Equation 4.3)}$$

where $\Omega = \frac{\omega\lambda_D a}{D} = \Omega_{MW}\, a/\lambda_D$ is the non-dimensional frequency scaled, $A \sim 50$ is a constant, and $B \propto \frac{\varepsilon_w}{\varepsilon_{Au}} \frac{a}{\lambda_D}$. Here, we evaluate $B \sim 0.6$. The pre-factors of **Equation 4.2** and **Equation 4.3** are fitting parameters to the experimental data. It is seen that beyond the charge relaxation time of the induced EDL (i.e., $\Omega > 1$), the ICEP contribution decays to zero according to Ω^{-2}, while the sDEP approaches asymptotically towards its maximal value (**Fig. 4.7**). The exact frequency at which the direction of rotation of the microspinners will invert is strongly dependent on the relative magnitudes of the ICEP and sDEP, the latter being heavily dictated by the distance between the particle center to the bottom substrate, h, scaled with $(a/h)^5$.[23] Since we did not measure *h*, we fitted a pre-factor (- 3,500) for the sDEP, which is different from that used as a fitting pre-factor (2.2) for the ICEP contribution.

The total angular velocity, which is a superposition of the three contributions, i.e., $\dot{\theta}_{total}(\Omega) = \dot{\theta}_{EHD}(\Omega) + \dot{\theta}_{ICEP}(\Omega) + \dot{\theta}_{sDEP}(\Omega)$, is also depicted in **Figure 4.7** (as dashed lines). Although there are some quantitative differences between the model and experiments, the model and the data agree well qualitatively, and in particular, the model captures the three reversals of

the rotation direction. The differences stem from the simpler geometries used in the models in contrast to the much more complicated morphology of the microspinner. In addition, for reasons of simplicity, we neglected the possible low frequency dispersion behavior of the ICEP effect due to partial screening of the powered electrodes (commonly, these electrodes do not behave as ideal blocking electrodes due to faradaic reactions that are able to support a current also at DC conditions), which in turn results in the decrease of the electric field that acts on the floating metallic patches and thus the ICEO intensity.

4.4 Conclusions

In summary, we have investigated a new class of supercolloidal microspinner particles that rotate around their central axis with a spin direction that is singularly controlled by the frequency of an externally applied electric field. We show that the reversal of their rotation occurs at three critical frequencies, unlike their non-patchy counterparts, which exhibit only one rotational inversion. We performed a series of scaling analyses to reveal that the non-patchy microspinners invert their direction of rotation due to a reversal in EHD flows, and that the patchy microspinners switch their direction of rotation two additional times due to the transition between EHD flows and ICEP as well as between ICEP and sDEP, respectively.

While this study provides fundamental data describing the electrokinetic mechanisms of motion of such microspinners, the results indicate a greater need to understand and model more complex systems.[37,38] While Janus particles have been studied in great detail over the last decade,[39–41] the complexity of our microspinners introduces a new level of sophistication where more complex modeling strategies will be required. In particular, modeling the interplay of propulsive effects, like those presented here (i.e., EHD flows, ICEP, and sDEP), will be key to

understanding how to design new types of active particles with complex designs that can harvest and dissipate energy through multiple pathways. Such principles could be extended to create new types of active particles that generate more sophisticated propulsive motions, like orbital and precessional motions, and more importantly, that can switch between different modes of propulsion on demand.

Looking forward, this set of results suggests new ways to develop active particles that controllably change their direction of motion on demand. By engineering particles with sophisticated shapes and with complex metallic surface patterns, we believe it should be possible to remotely power particles to undergo navigational steering (i.e., without a reliance on global field gradients).[42,43] These more complex behaviors could open the way to making functional and collectively operating microswimmers that can perform a variety of tasks, including interlocking microgears in colloidal micromachines[18,19] and active particles that can navigate through highly complex fluid geometries (e.g., within vessels of the human body).[44]

4.5 Acknowledgements

We thank Martin Z. Bazant, Nan M. Jokerst, and Ugonna Ohiri for helpful discussions. This work was supported by the U.S. National Science Foundation's (NSF's) Research Triangle Materials Research Science and Engineering Center (MRSEC; DMR-1121107). Microspinners were fabricated in the Shared Materials Instrumentation Facility (SMIF) at Duke University, which is a member of the North Carolina Research Triangle Nanotechnology Network (RTNN) and is supported by the NSF (Grant ECCS-1542015) as part of the National Nanotechnology Coordinated Infrastructure (NNCI). The authors have no conflicts of interest.

4.6 References

[1] C. W. Shields IV, O. D. Velev. The Evolution of Active Particles: Towards Externally Powered Self-Propelling and Self-Reconfiguring Particle Systems. *Chem* **2017**, *3*, 539.

[2] J. Zhang, E. Luijten, B. A. Grzybowski, S. Granick. Active Colloids with Collective Mobility Status and Research Opportunities. *Chem. Soc. Rev.* **2017**, *46*, 5551.

[3] C. Hu, S. Pane, B. J. Nelson. Soft Micro- and Nanorobotics. *Annu. Rev. Control Robot. Auton. Syst* **2018**, *1*, 14.

[4] K. Han, C. W. Shields IV, O. D. Velev. Engineering of Self-Propelling Microbots and Microdevices Powered by Magnetic and Electric Fields. *Adv. Funct. Mater*. **2018**, DOI: 10.1002/adfm.201705953.

[5] J. Li, O. E. Shklyaev, T. Li, W. Liu, H. Shum, I. Rozen, A. C. Balazs, J. Wang. Self-Propelled Nanomotors Autonomously Seek and Repair Cracks. *Nano Lett.* **2015**, *15*, 7077.

[6] M. Kaynak, A. Ozcelik, A. Nourhani, P. E. Lammert, V. H. Crespi, T. J. Huang. Acoustic Actuation of Bioinspired Microswimmers. *Lab Chip* **2017**, *17*, 395.

[7] S. Ni, E. Marini, I. Buttinoni, H. Wolf, L. Isa. Hybrid Colloidal Microswimmers through Sequential Capillary Assembly. *Soft Matter* **2017**, *13*, 4252.

[8] R. Dreyfus, J. Baudry, M. L. Roper, M. Fermigier, H. A. Stone, J. Bibette. Microscopic Artificial Swimmers. *Nature* **2005**, *437*, 862.

[9] P. Tierno, R. Golestanian, I. Pagonabarraga, F. Sagués. Magnetically Actuated Colloidal Microswimmers. *J. Phys. Chem. B* **2008**, *112*, 16525.

[10] W. Gao, S. Sattayasamitsathit, K. M. Manesh, D. Weihs, J. Wang. Magnetically Powered Flexible Metal Nanowire Motors. *J. Am. Chem. Soc.* **2010**, *132*, 14403.

[11] S. Tottori, L. Zhang, F. Qiu, K. K. Krawczyk, A. Franco-Obregón, B. J. Nelson. Magnetic Helical Micromachines: Fabrication, Controlled Swimming, and Cargo Transport. *Adv. Mater.* **2012**, *24*, 811.

[12] M. Liu, T. Zentgraf, Y. Liu, G. Bartal, X. Zhang. Light-Driven Nanoscale Plasmonic Motors. *Nat. Nanotechnol.* **2010**, *5*, 570.

[13] H.-R. Jiang, N. Yoshinaga, M. Sano. Active Motion of a Janus Particle by Self-Thermophoresis in a Defocused Laser Beam. *Phys. Rev. Lett.* **2010**, *105*, 268302.

[14] L. Shao, Z. J. Yang, D. Andrén, P. Johansson, M. Käll. Gold Nanorod Rotary Motors Driven by Resonant Light Scattering. *ACS Nano* **2015**, *9*, 12542.

[15] C. Maggi, F. Saglimbeni, M. Dipalo, F. De Angelis, R. Di Leonardo. Micromotors with Asymmetric Shape That Efficiently Convert Light into Work by Thermocapillary Effects. *Nat. Commun.* **2015**, *6*, 7855.

[16] G. Kokot, S. Das, R. G. Winkler, G. Gompper, I. S. Aranson, A. Snezhko. Active Turbulence in a Gas of Self-Assembled Spinners. *Proc. Natl. Acad. Sci.* **2017**, *114*, 12870.

[17] S. Sabrina, M. Tasinkevych, S. Ahmed, A. M. Brooks, M. Olvera De La Cruz, T. E. Mallouk, K. J. M. Bishop. Shape-Directed Microspinners Powered by Ultrasound. *ACS Nano* **2018**, *12*, 2939.

[18] N. H. P. Nguyen, D. Klotsa, M. Engel, S. C. Glotzer. Emergent Collective Phenomena in a

Mixture of Hard Shapes through Active Rotation. *Phys. Rev. Lett.* **2014**, *112*, 75701.

[19] M. Spellings, M. Engel, D. Klotsa, S. Sabrina, A. M. Drews, N. H. P. Nguyen, K. J. M. Bishop, S. C. Glotzer. Shape Control and Compartmentalization in Active Colloidal Cells. *Proc. Natl. Acad. Sci.* **2015**, *112*, E4642.

[20] O. D. Velev, K. H. Bhatt. On-Chip Micromanipulation and Assembly of Colloidal Particles by Electric Fields. *Soft Matter* **2006**, *2*, 738.

[21] F. Ma, X. Yang, H. Zhao, N. Wu. Inducing Propulsion of Colloidal Dimers by Breaking the Symmetry in Electrohydrodynamic Flow. *Phys. Rev. Lett.* **2015**, *115*, 208302.

[22] S. Gangwal, O. Cayre, M. Z. Bazant, O. D. Velev. Induced-Charge Electrophoresis of Metallodielectric Particles. *Phys. Rev. Lett.* **2008**, *100*, 58302.

[23] A. Boymelgreen, G. Yossifon, T. Miloh. Propulsion of Active Colloids by Self-Induced Field Gradients. *Langmuir* **2016**, *32*, 9540.

[24] S. T. Chang, V. N. Paunov, D. N. Petsev, O. D. Velev. Remotely Powered Self-Propelling Particles and Micropumps Based on Miniature Diodes. *Nat. Mater.* **2007**, *6*, 235.

[25] R. Sharma, O. D. Velev. Remote Steering of Self-Propelling Microcircuits by Modulated Electric Field. *Adv. Funct. Mater.* **2015**, *25*, 5512.

[26] U. Ohiri, C. W. S. Iv, K. Han, O. D. Velev, N. Jokerst, T. Tyler. Reconfigurable Engineered Motile Semiconductor Microparticles. *Nat. Commun.* **2018**, *9*, 1791.

[27] T. K. Khurana, J. G. Santiago. Effects of Carbon Dioxide on Peak Mode Isotachophoresis: Simultaneous Preconcentration and Separation. *Lab Chip* **2009**, *9*, 1377.

[28] S. Wang, F. Ma, H. Zhao, N. Wu. Bulk Synthesis of Metal-Organic Hybrid Dimers and Their Propulsion under Electric Fields. *ACS Appl. Mater. Interfaces* **2014**, *6*, 4560.

[29] F. Ma, S. Wang, D. T. Wu, N. Wu. Electric-Field–induced Assembly and Propulsion of Chiral Colloidal Clusters. *Proc. Natl. Acad. Sci.* **2015**, *112*, 6307.

[30] W. D. Ristenpart, I. A. Aksay, D. A. Saville. Electrohydrodynamic Flow around a Colloidal Particle near an Electrode with an Oscillating Potential. *J. Fluid Mech.* **2007**, *575*, 83.

[31] T. M. Squires, M. Z. Bazant. Induced-Charge Electro-Osmosis. *J. Fluid Mech.* **2004**, *509*, 217.

[32] M. Z. Bazant, T. M. Squires. Current Opinion in Colloid & Interface Science Induced-Charge Electrokinetic Phenomena. *Curr. Opin. Colloid Interface Sci.* **2010**, *15*, 203.

[33] M. S. Kilic, M. Z. Bazant. Induced-Charge Electrophoresis near a Wall. *Electrophoresis* **2011**, *32*, 614.

[34] T. M. Squires, M. Z. Bazant. Breaking Symmetries in Induced-Charge Electro-Osmosis and Electrophoresis. *J. Fluid Mech.* **2006**, *560*, 65.

[35] A. Boymelgreen, G. Yossifon, S. Park, T. Miloh. Spinning Janus Doublets Driven in Uniform Ac Electric Fields. *Phys. Rev. E* **2014**, *89*, 11003.

[36] A. M. Brooks, S. Sabrina, K. J. M. Bishop. Shape-Directed Dynamics of Active Colloids Powered by Induced-Charge Electrophoresis. *Proc. Natl. Acad. Sci.* **2018**, *115*, E1090.

[37] Q. Brosseau, G. Hickey, P. M. Vlahovska. Electrohydrodynamic Quincke Rotation of a Prolate Ellipsoid. *Phys. Rev. Fluids* **2017**, *2*, 14101.

[38] Y. Hu, P. M. Vlahovska, M. J. Miksis. Colloidal Particle Electrorotation in a Non-Uniform Electric Field. *Phys. Rev. E* **2018**, *97*, 13111.

[39] A. Walther, A. H. E. Müller. Janus Particles: Synthesis, Self-Assembly, Physical Properties, and Applications. *Chem. Rev.* **2013**, *113*, 5194.

[40] J. Yan, M. Bloom, S. C. Bae, E. Luijten, S. Granick. Linking Synchronization to Self-Assembly Using Magnetic Janus Colloids. *Nature* **2012**, *491*, 578.

[41] A. M. Boymelgreen, T. Balli, T. Miloh, G. Yossifon. Active Colloids as Mobile Microelectrodes for Unified Label-Free Selective Cargo Transport. *Nat. Commun.* **2018**, *9*, 760.

[42] V. Garcia-gradilla, J. Orozco, S. Sattayasamitsathit, F. Soto, F. Kuralay, A. Pourazary, A. Katzenberg, W. Gao, Y. Shen, J. Wang. Functionalized Ultrasound-Propelled Magnetically Guided Nanomotors: Toward Practical Biomedical Applications. *ACS Nano* **2013**, *7*, 9232.

[43] X.-Z. Chen, N. Shamsudhin, M. Hoop, R. Pieters, E. Siringil, M. S. Sakar, B. J. Nelson, S. Pané. Magnetoelectric Micromachines with Wirelessly Controlled Navigation and Functionality. *Mater. Horiz.* **2016**, *3*, 113.

[44] T. Qiu, T.-C. Lee, A. G. Mark, K. I. Morozov, R. Münster, O. Mierka, S. Turek, A. M. Leshansky, P. Fischer. Swimming by Reciprocal Motion at Low Reynolds Number. *Nat. Commun.* **2014**, *5*, 5119.

Chapter 5

Summary and Outlook*

* Partially based on Han, Shields IV, and Velev, *Adv. Funct. Mater.* **2018**, in press.

5.1 Summary

Interest in colloidal systems of anisotropic particles in external fields has grown dramatically over the past few years due to their unusual interactions, dynamic functions and structure formation abilities, as discussed in Chapter 1. The overarching goal of my graduate research is to gain fundamental insights into these systems and utilize these principles to address ongoing engineering challenges. One example is making miniaturized robotic devices for remote sensing, cell-level diagnoses, drug delivery and microsurgical devices, all of which require microscale operations. In this thesis research, as a means to precisely control dynamic behaviors of colloidal systems, external fields were applied to anisotropic colloidal particles, leading to encoded directional responses depending on system design elements. Building upon a number of fundamental breakthroughs identified during our studies, new types of colloidal microbots, microswimmers and microdevices were developed.

Chapter 2 presents self-reconfiguring microbots assembled from one-side cobalt coated patchy microcubes in external magnetic fields. We showed that assemblies of such patchy microcubes can be engineered to store energy in the cobalt patches through magnetic polarization and release it by microscale reconfiguration. The residual polarization of the cobalt patches allowed on-demand dynamic reconfiguration of the assemblies. It is achieved by switching between directional field-dipole and dipole-dipole interactions via turning the magnetic field on and off. The pattern of cluster reconfiguration can be encoded in the sequence of the cube orientations within the assemblies. We provided examples of cube clusters of specific sequences that can be actuated to perform microscale operations such as capturing and transporting live cells, acting as microbot prototypes.

Chapter 3 reports new methods for active swimming of the self-assembled microbots in non-Newtonian fluids by cyclic time-asymmetric magnetic fields. A scallop-like self-assembled cluster with a cyclic time-asymmetric flapping stroke did not generate net displacement in Newtonian fluids due to its time-reversal symmetry at low Re regimes. Directional active swimming of self-assembled "microscallops" was achieved by locally modulating the viscosity of surrounding non-Newtonian fluids through magnetic field-controlled time-asymmetric flapping strokes. The viscophoretic swimming motility of microscallop assemblies was investigated by analyzing how the time-asymmetry of flapping patterns and the microscallop geometric designs determine the swimming direction. These microscallop assemblies displayed the ability to switch their swimming modes between forward, backward and stationary motion by adjusting the field strength and controlling the relative speed between their opening and closing stroke.

In Chapter 4, we report active rotation of engineered anisotropic particles in external AC electric fields. We show that active propulsion modes of engineered particles can be encoded via the anisotropy of the particle shape and/or polarizabilities. We demonstrated how to electrokinetically tune their dynamic responses using the AC field parameters, including field frequency, strength and direction. The characterization of the role of these parameters enabled the evaluation of the relative role of multiple electrokinetic effects, including induced charge electrophoresis, AC dielectrophoresis and asymmetric EHD flows. This in turn allowed establishing design principles for a new generation of self-propelling devices with electrically switchable rotation and lock/unlock functions.

5.2 Future Outlook

My PhD research has focused on understanding the fundamentals behind the dynamic behaviors of anisotropic colloidal particles in external fields. From an engineering perspective, a variety of field-driven dynamic responses can be encoded in the design of anisotropic particles. By concentrating on particle-particle and particle-medium interactions, we identified rules on how to directionally control the assembly, reconfiguration and self-propulsion of systems of engineered anisotropic particles. My further interest lies in extending the principles of such dynamic functions on the microscale to a macroscale engineered system. Below, two concepts are envisioned for formulating new classes of stimuli-responsive functional materials by integrating responsive particles with a soft matrix.

The first technique involves embedding magnetically responsive engineered particles in a soft matrix for the generation of magnetoactive composites. One example is using patchy polymer microcubes in which two opposite sides were coated with a magnetizable film (**Fig. 5.1**). Such cubes can be readily microfabricated by depositing a metal film on the top side of an array of cubes formed via photolithography,[1] then depositing metal on the opposite side after flipping the whole array using a polymer stamp.[2] The structure-formation capabilities of these two-side coated microcubes are schematically illustrated in **Figure 5.1**. The interactions between the two in-parallel magnetized films will lead to the formation of an extremely rigid lattice with two distinct sequences (**Fig. 5.1a→b**). The *A*-*A* sequence will create a stiff and inflexible link because the two neighboring cubes are spatially locked by the interacting magnetized films on both top and bottom sides. Sturdy chains connected by the *A*-*A* sequences can be further cross-linked by adjacent cubes in the *A*-*B* sequence, firmly locking the lattice.

Assembling these unique structures in a gel matrix may allow the production of engineered composite gels. The critical feature of these gels will be their switchable rheological properties depending on the strength of an applied magnetic field. The stronger the applied field, the stiffer the gels become due to a higher cross-linking density of the assembled cube lattices. The stiff and solid gels can be potentially transformed into a completely liquid state by disassembling the cube lattices. Disassembly can be performed by demagnetizing the metallic facets of the cube particles via application of a time-decaying oscillating magnetic field (**Fig. 5.1b→a**).[3] Consequently, these gels could reversibly switch their phase state between the solid and liquid by remote magnetization and demagnetization. Such a magnetoactive switchable gel may find applications in adaptive materials, switchable devices, and targeted drug delivery.

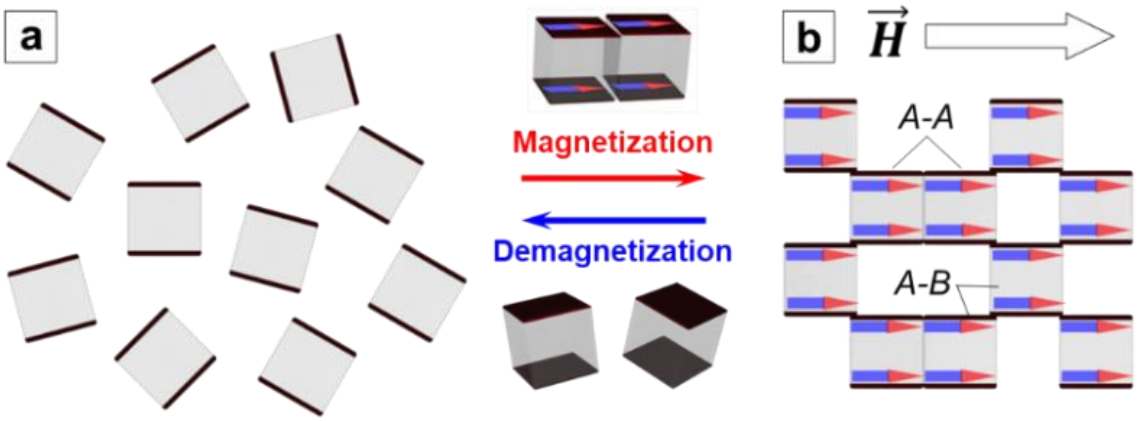

Figure 5.1: Schematics of expected assembly and disassembly behaviors of two-side coated microcubes. (**a**) Dispersed non-magnetized cubes and (**b**) Formation of rigid crosslinked lattices. Remote magnetization and demagnetization enable the transition between the state (**a**) and (**b**).

The second new type of stimuli-responsive material is an electro-active engineered hydrogel system constructed by coupling polyelectrolyte hydrogels with active diodes. When subjected to global direct current (DC) electric fields, polyelectrolyte-doped hydrogels directionally bend because the DC electric fields asymmetrically re-distribute mobile ions and create osmotic pressure differences around the hydrogels.[4–6] For example, under a DC electric

field, an anionic hydrogel bends toward the cathode because the electrophoretic migration of mobile cations toward the cathode causes the osmotic pressure difference between the hydrogel interfaces at the anode and cathode side ($\pi_1 > \pi_2$; **Fig. 5.2**). Such electrophoretic hydrogel bending mechanism has been employed for making electro-active hydrogel actuators.[7] These electroactive hydrogel components have shown promise for building systems of soft robot prototypes including hydrogel walkers[8] and octopus-like aquabots.[9] However, when global DC electric fields are used as a power source, these systems require sophisticatedly designed hydrogels[9] and/or an elaborate electrode setup[10] for their directional movements. Also, they operate at relatively high DC voltages, which may cause undesirable electrolysis and degradation in biological systems.

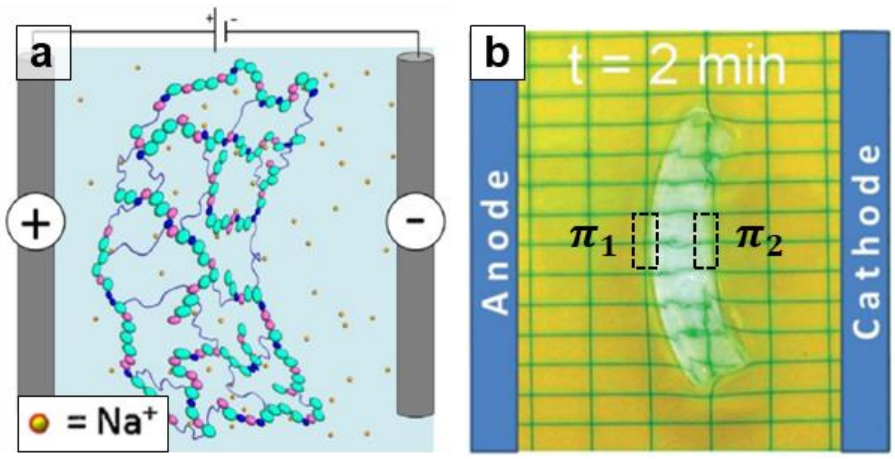

Figure 5.2: (**a**) Schematic and (**b**) snapshot of the bending of an anionic hydrogel in a global DC electric field. The hydrogel bending is attributed to the osmotic pressure difference ($\pi_1 > \pi_2$) by electrophoretic migration of mobile cations toward the cathode in the global DC electric field. The schematic in (**a**) reproduced with permission.[5] Copyright 2016, Elsevier. The snapshot in (**b**) is reproduced with permission.[6] Copyright 2012, Royal Society of Chemistry.

One approach to address these challenges is to utilize locally induced DC fields from diodes powered by global alternating current (AC) electric fields. This approach was inspired by

the pioneering work of the Velev group[11,12] on AC electric field-powered propulsion of diodes. They reported that commercial diodes floating in water can self-propel by generating self-electroosmotic flows in response to global AC electric fields. In preliminary experiments in this research, the self-electroosmotic flows generated by remotely powered diodes were used to locally bend hydrogels in global AC electric fields (**Fig. 5.3a**). The bending patterns of hydrogels can be programmed depending on the number and orientation of diodes surrounding the target hydrogels. For example, a hydrogel strip placed in contact with three diodes with an alternating orientation wes bent into a zigzag pattern (**Fig. 5.3b**).

A multi-responsive hydrogel system can be constructed by replacing regular diodes with photodiodes. Under a global AC electric field, photodiodes can be externally controlled by light to bend the adjacent hydrogel. When no light illumination exists, a photodiode acts as a regular diode and generates a local DC field, which leads to hydrogel bending. Conversely, hydrogel bending by the photodiode can be suppressed during light illumination because a photodiode converts light into an electric bias eliminating the DC potential between its electrodes.[13] On this basis, two opposing photodiodes can generate reversible hydrogel bending as illustrated in **Figure 5.3c**. First, the hydrogel bends upward when the external light illuminates only the bottom photodiode. The hydrogel bends in the opposite direction, i.e., downward, when an external light illuminates the top photodiode, while the illumination is simultaneously removed from the bottom photodiode. The ability to programmably control bending actuation of these diode-directed active hydrogel systems is an example of the broad array of emerging new opportunities in stimuli-responsive materials and soft robotics.[14]

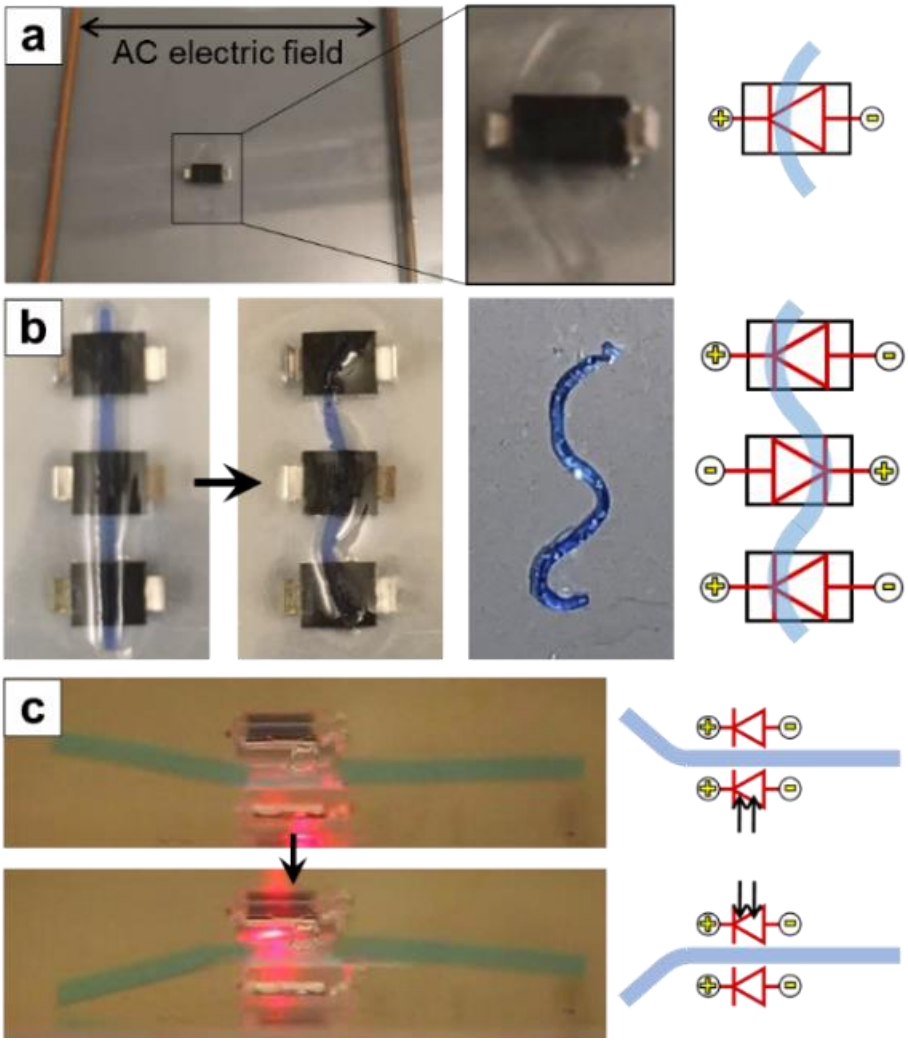

Figure 5.3: Bending of anionic hydrogels by remotely powered and controlled diodes in a global AC electric field. (**a**) Experimental setup depicting a diode-directed hydrogel bending system. The diode rectifies the global AC field into a local DC field, thereby inducing hydrogel bending. (**b**) Hydrogel bending from the linear to zigzag pattern by three externally powered diodes. (**c**) Light-responsive hydrogel bending using opposing photodiodes. Selective light illumination controls the direction of hydrogel bending. Schematics on the right-side illustrate the dependence of hydrogel bending on the diode orientation in (**b**) and the photodiode functionality in (**c**).

Beyond stimuli-responsive functional materials, active particles have emerged as a topic of scientific interest in the field of soft matter due to their ability to harvest, sometimes store, and directionally release energy on demand. They are useful for studying fundamental phenomena like swarming, phase changes and locomotion,[15,16] and are beginning to prove their potential to solve

numerous engineering problems. For example, such particles are currently being developed for potential applications,[17,18] including targeted drug delivery,[19] environmental remediation,[20] detoxification[21] and constituents in self-healing materials.[22] Controlling their movements and interactions is key to increasing the likelihood for their translation to practical use. We believe that this can be achieved in two ways. First, external electric and magnetic fields provide a direct and facile way to control particle dynamics in real time. This is largely because external fields can be tuned, are directional and externally powered, which contrasts other mechanisms such as catalytic propulsion.[23] Second, the engineering the properties of active particles can enable even finer control of their movements by imparting multiple ways in which energy can be harvested and directionally dissipated.

There are many ways in which active particles can be engineered to transduce energy, although many of these mechanisms are still relatively early in their development. We believe that combining features in (or on) the particles with various methods for enhancing their energization is the key to the continued progress in this area. The mechanisms for particles empowerment by electric and magnetic fields include asymmetric EHD flows,[24,25] induced-charge electrophoresis,[26,27] self-rectified electrophoresis,[11,12] self-dielectrophoresis,[28,29] helical propulsion,[30,31] traveling-wave propulsion,[32,33] surface-assisted propulsion[34,35] and time-asymmetric flapping propulsion.[36] While we have shown a few examples of particles empowered by several of these phenomena, we believe that combinations of these effects (by engineering particles with complex shape, composition and surface properties) will "propel" these particles into mainstream use.

Two critical issues may need to be addressed to secure the successful translation of these particles into more routine applications.[37] First, the lack of directional navigation remains a major

problem for many types of active particles. The concept of steering active particles is still somewhat nascent; however, as demonstrated by others,[38–41] directional control can also be introduced by external magnetic and electric fields. Since external fields often impart directionality, they can be used to align particles via magnetic[42,43] or electric torque.[44,45] Second, many methods for driving the movement of active particles are inefficient to the point of impracticality.[23] Active particles are, by definition, out of equilibrium. Therefore, the efficient transduction of energy must be a priority in the scale up and manufacturing of such particles. Electric and magnetic fields may offer workable means to energize such particles, though the efficiency of energy transduction is largely dependent on the design of the corresponding active particles. For example, the efficiency of energy transduction for the early helical magnetic swimmer[46] has been estimated as 0.66% (or ~10^{-3}) based on evaluation where the mechanical power output (i.e., the drag force applied on the swimmer multiplied by its axial swimming speed) is normalized by magnetic power input.[47] This value is relatively high compared to that of some Au/Pt catalytic motors, which have been estimated to have a power conversion efficiency of ~10^{-9}.[48] Therefore, as advancements in particle fabrication emerge, active particles can be made with more sophisticated means of harvesting and dissipating energy. We believe this next step is critical in translating active particles from their current state, i.e., from simple motile entities, to usable tools that solve important problems and enable the development of new technologies. This can be achieved by integrating comprehensive design elements into an engineered particle, building upon the intrinsic connection between particle design and function.[49]

5.3 References

[1] C. W. Shields IV, S. Zhu, Y. Yang, B. Bharti, J. Liu, B. B. Yellen, O. D. Velev, G. P. López. Field-Directed Assembly of Patchy Anisotropic Microparticles with Defined Shape. *Soft Matter* **2013**, *9*, 9219.

[2] Q. Chen, E. Diesel, J. K. Whitmer, S. C. Bae, E. Luijten, S. Granick. Triblock Colloids for Directed Self-Assembly. *J. Am. Chem. Soc.* **2011**, *133*, 7725.

[3] E. Blanco, S. Lam, S. K. Smoukov, K. P. Velikov, S. A. Khan, O. D. Velev. Stability and Viscoelasticity of Magneto-Pickering Foams. *Langmuir* **2013**, *29*, 10019.

[4] Y. Osada, H. Okuzaki, H. Hori. A Polymer Gel with Electrically Driven Motility. *Nature* **1992**, *355*, 242.

[5] L. Migliorini, T. Santaniello, Y. Yan, C. Lenardi, P. Milani. Low-Voltage Electrically Driven Homeostatic Hydrogel-Based Actuators for Underwater Soft Robotics. *Sensors Actuators B Chem.* **2016**, *228*, 758.

[6] P. J. Glazer, M. van Erp, A. Embrechts, S. G. Lemay, E. Mendes. Role of pH Gradients in the Actuation of Electro-Responsive Polyelectrolyte Gels. *Soft Matter* **2012**, *8*, 4421.

[7] L. Hines, K. Petersen, G. Z. Lum, M. Sitti. Soft Actuators for Small-Scale Robotics. *Adv. Mater.* **2017**, *29*, 1603483.

[8] D. Morales, E. Palleau, M. D. Dickey, O. D. Velev. Electro-Actuated Hydrogel Walkers with Dual Responsive Legs. *Soft Matter* **2014**, *10*, 1337.

[9] G. H. Kwon, J. Y. Park, J. Y. Kim, M. L. Frisk, D. J. Beebe, S. H. Lee. Biomimetic Soft Multifunctional Miniature Aquabots. *Small* **2008**, *4*, 2148.

[10] M. Otake. *Electroactive Polymer Gel Robots: Modelling and Control of Artificial Muscles*; Springer: Berlin, 2010.

[11] S. T. Chang, V. N. Paunov, D. N. Petsev, O. D. Velev. Remotely Powered Self-Propelling Particles and Micropumps Based on Miniature Diodes. *Nat. Mater.* **2007**, *6*, 235.

[12] R. Sharma, O. D. Velev. Remote Steering of Self-Propelling Microcircuits by Modulated Electric Field. *Adv. Funct. Mater.* **2015**, *25*, 5512.

[13] J. Singh. *Semiconductor Devices: An Introduction*; McGraw-Hill: New York, 1994.

[14] L. Zhu, Y. Cao, Y. Liu, Z. Yang, X. Chen. Architectures of Soft Robotic Locomotion Enabled by Simple Mechanical Principles. *Soft Matter* **2017**, *13*, 4441.

[15] J. Zhang, E. Luijten, B. A. Grzybowski, S. Granick. Active Colloids with Collective Mobility Status and Research Opportunities. *Chem. Soc. Rev.* **2017**, *46*, 5551.

[16] P. Illien, R. Golestanian, A. Sen. "Fuelled" Motion: Phoretic Motility and Collective Behaviour of Active Colloids. *Chem. Soc. Rev.* **2017**, *46*, 5508.

[17] B. J. Nelson, I. K. Kaliakatsos, J. J. Abbott. Microrobots for Minimally Invasive Medicine. *Annu. Rev. Biomed. Eng.* **2010**, *12*, 55.

[18] J. Wang, W. Gao. Nano/Microscale Motors: Biomedical Opportunities and Challenges. *ACS Nano* **2012**, *6*, 5745.

[19] R. W. Carlsen, M. Sitti. Bio-Hybrid Cell-Based Actuators for Microsystems. *Small* **2014**,

10, 3831.

[20] M. Guix, J. Orozco, M. García, W. Gao, S. Sattayasamitsathit, A. Merkoçi, A. Escarpa, J. Wang. Superhydrophobic Alkanethiol-Coated Microsubmarines for Effective Removal of Oil. *ACS Nano* **2012**, *6*, 4445.

[21] J. Li, B. Esteban-Fernández de Ávila, W. Gao, L. Zhang, J. Wang. Micro/nanorobots for Biomedicine: Delivery, Surgery, Sensing, and Detoxification. *Sci. Robot.* **2017**, *2*, eaam6431.

[22] J. Li, O. E. Shklyaev, T. Li, W. Liu, H. Shum, I. Rozen, A. C. Balazs, J. Wang. Self-Propelled Nanomotors Autonomously Seek and Repair Cracks. *Nano Lett.* **2015**, *15*, 7077.

[23] W. Wang, W. Duan, S. Ahmed, T. E. Mallouk, A. Sen. Small Power: Autonomous Nano- and Micromotors Propelled by Self-Generated Gradients. *Nano Today* **2013**, *8*, 531.

[24] F. Ma, S. Wang, D. T. Wu, N. Wu. Electric-Field–induced Assembly and Propulsion of Chiral Colloidal Clusters. *Proc. Natl. Acad. Sci.* **2015**, *112*, 6307.

[25] F. Ma, X. Yang, H. Zhao, N. Wu. Inducing Propulsion of Colloidal Dimers by Breaking the Symmetry in Electrohydrodynamic Flow. *Phys. Rev. Lett.* **2015**, *115*, 208302.

[26] T. M. Squires, M. Z. Bazant. Breaking Symmetries in Induced-Charge Electro-Osmosis and Electrophoresis. *J. Fluid Mech.* **2006**, *560*, 65.

[27] S. Gangwal, O. Cayre, M. Z. Bazant, O. D. Velev. Induced-Charge Electrophoresis of Metallodielectric Particles. *Phys. Rev. Lett.* **2008**, *100*, 58302.

[28] A. Boymelgreen, G. Yossifon, T. Miloh. Propulsion of Active Colloids by Self-Induced Field Gradients. *Langmuir* **2016**, *32*, 9540.

[29] A. M. Boymelgreen, T. Balli, T. Miloh, G. Yossifon. Active Colloids as Mobile Microelectrodes for Unified Label-Free Selective Cargo Transport. *Nat. Commun.* **2018**, *9*, 760.

[30] A. Ghosh, P. Fischer. Controlled Propulsion of Artificial Magnetic Nanostructured Propellers. *Nano Lett.* **2009**, *9*, 2243.

[31] L. Zhang, J. J. Abbott, L. Dong, B. E. Kratochvil, D. Bell, B. J. Nelson. Artificial Bacterial Flagella: Fabrication and Magnetic Control. *Appl. Phys. Lett.* **2014**, *94*, 64107.

[32] R. Dreyfus, J. Baudry, M. L. Roper, M. Fermigier, H. A. Stone, J. Bibette. Microscopic Artificial Swimmers. *Nature* **2005**, *437*, 862.

[33] W. Gao, S. Sattayasamitsathit, K. M. Manesh, D. Weihs, J. Wang. Magnetically Powered Flexible Metal Nanowire Motors. *J. Am. Chem. Soc.* **2010**, *132*, 14403.

[34] L. Zhang, T. Petit, Y. Lu, B. E. Kratochvil, K. E. Peyer, R. Pei, J. Lou, B. J. Nelson. Controlled Propulsion and Cargo Transport of Rotating Nickel Nanowires near a Patterned Solid Surface. *ACS Nano* **2010**, *4*, 6228.

[35] P. Tierno, R. Golestanian, I. Pagonabarraga, F. Sague. Controlled Swimming in Confined Fluids of Magnetically Actuated Colloidal Rotors. *Phys. Rev. Lett.* **2008**, *101*, 218304.

[36] T. Qiu, T.-C. Lee, A. G. Mark, K. I. Morozov, R. Münster, O. Mierka, S. Turek, A. M. Leshansky, P. Fischer. Swimming by Reciprocal Motion at Low Reynolds Number. *Nat. Commun.* **2014**, *5*, 5119.

[37] C. W. Shields IV, O. D. Velev. The Evolution of Active Particles: Towards Externally Powered Self-Propelling and Self-Reconfiguring Particle Systems. *Chem* **2017**, *3*, 539.

[38] J. Wang, K. M. Manesh. Motion Control at the Nanoscale. *Small* **2010**, *6*, 338.

[39] J. Burdick, R. Laocharoensuk, P. M. Wheat, J. D. Posner, J. Wang. Synthetic Nanomotors in Microchannel Networks : Directional Microchip Motion and Controlled Manipulation of Cargo. *J. Am. Chem. Soc.* **2008**, *130*, 8164.

[40] V. Garcia-gradilla, J. Orozco, S. Sattayasamitsathit, F. Soto, F. Kuralay, A. Pourazary, A. Katzenberg, W. Gao, Y. Shen, J. Wang. Functionalized Ultrasound-Propelled Magnetically Guided Nanomotors: Toward Practical Biomedical Applications. *ACS Nano* **2013**, *7*, 9232.

[41] L. Baraban, D. Makarov, R. Streube, I. Mönch, D. Grimm, S. Sanchez, O. G. Schmidt. Catalytic Janus Motors on Micro Fluidic Chip: Deterministic Motion for Targeted Cargo Delivery. *ACS Nano* **2012**, *6*, 3383.

[42] R. M. Erb, J. J. Martin, R. Soheilian, C. Pan, J. R. Barber. Actuating Soft Matter with Magnetic Torque. *Adv. Funct. Mater.* **2016**, *26*, 3859.

[43] R. S. M. Rikken, R. J. M. Nolte, J. C. Maan, J. C. M. van Hest, D. A. Wilson, P. C. M. Christianen. Manipulation of Micro- and Nanostructure Motion with Magnetic Fields. *Soft Matter* **2014**, *10*, 1295.

[44] T. B. Jones. Basic Theory of Dielectrophoresis and Electrorotation. *IEEE Eng. Med. Biol. Mag.* **2003**, *22*, 33.

[45] K. Kim, X. Xu, J. Guo, D. L. Fan. Ultrahigh-Speed Rotating Nanoelectromechanical System Devices Assembled from Nanoscale Building Blocks. *Nat. Commun.* **2014**, *5*, 3632.

[46] L. Zhang, J. J. Abbott, L. Dong, K. E. Peyer, B. E. Kratochvil, H. Zhang, C. Bergeles, B. J. Nelson. Characterizing the Swimming Properties of Artificial Bacterial Flagella. *Nano Lett.* **2009**, *9*, 3663.

[47] W. Wang, T. Chiang, D. Velegol, T. E. Mallouk. Understanding the Efficiency of Autonomous Nano- and Microscale Motors. *J. Am. Chem. Soc.* **2013**, *135*, 10557.

[48] W. F. Paxton, A. Sen, T. E. Mallouk. Motility of Catalytic Nanoparticles through Self-Generated Forces. *Chem. Eur. J.* **2005**, *11*, 6462.

[49] U. Ohiri, C. W. S. Iv, K. Han, O. D. Velev, N. Jokerst, T. Tyler. Reconfigurable Engineered Motile Semiconductor Microparticles. *Nat. Commun.* **2018**, *9*, 1791.